JÜLICH FORSCHUNGSZENTRUM

Final Report

Technical Assistance for the Deployment of an advanced hyperspectral imaging sensor during SoyFLEX2

ESA Contract No. 4000107143/12/NL/FF/lf CCN4

2 April 2018

FINAL VERSION

CzechGlobe

Fondazione Clima e Sostenibilità

UNIVERSITA' DEGLI STUDI DI MILANO BICOCCA

UNIVERSITÀ DEGLI STUDI DI UDINE

Uniwersytet Przyrodniczy w Poznaniu
Poznań University of Life Sciences

Table of Content

1 Summary of main findings 6
1.1 The FLEX airborne demonstrator *HyPlant*: A high-performance imaging spectrometer to measure reflectance and sun-induced fluorescence 6
1.2 Fluorescence retrieval and automated processing routine of the spectral fitting method and fluorescence maps 6
1.3 SoyFLEX2 experiment: Forward modelling of canopy fluorescence emission 7
2 Introduction and Background 8
3 Campaign objectives 8
4 Instrumentation, material and methods 10
4.1 Airborne sensor *HyPlant* 10
4.1.1 *HyPlant* data processing 13
4.1.2 Georectification of *HyPlant* images 20
4.1.3 TASI: Hyperspectral thermal sensor 24
4.1.4 Airborne platform 24
4.2 Correlative ground equipment 25
4.2.1 Imagine hyperspectral instruments for top-of-canopy measurements 25
4.2.2 Top-of-canopy reflectance and fluorescence measurements 26
4.2.3 Hyperspectral cal/val reference measurements 29
4.2.4 Leaf level reflectance and fluorescence measurements 35
4.2.5 Chlorophyll content 37
4.2.6 Structural characterization of the canopy 37
4.2.7 Gas exchange chambers 39
4.2.8 Atmospheric conditions 43
4.2.9 Meteorological conditions 45
5 Campaign sites and activities 49
5.1 Long term campaign site in Germany 49
5.1.1 Anthropogenic, agricultural area around Jülich 49
5.1.2 Research campus Klein-Altendorf, Germany 52
5.2 Spruce forest experimental site in Bílý Kříž, Czech Republic 55
5.3 SoyFLEX2 campaign site; Experimental farm Udine, Italy 57
5.3.1 Defined core dataset for SoyFLEX2 experiment 58
5.3.2 *HyPlant* quick looks of core dataset 59
6 Results 62
6.1 Mapping of the long term study sites 62
6.1.1 Anthropogenic, agricultural area around Jülich 62
6.1.2 Agricultural research Campus Klein-Altendorf 80
6.1.3 Forest area in Bílý Kříž, Czech Republic 82
6.2 Vegetation indices and fluorescence maps and of the SoyFLEX2 experiment 84

6.2.1 Vegetation indices of the SoyFLEX2 experiment 85
6.2.2 Red and far-red fluorescence maps of the SoyFLEX 2 experiment 86
6.2.3 Validation of fluorescence maps from iFLD and Spectral Fitting Method, with the ground reference measurements 92
6.3 The SoyFLEX2 experiment 96
6.3.1 Motivation of the SoyFLEX2 experiment 96
6.3.2 Gas exchange chamber measurements on the canopy level 98
6.3.3 Chlorophyll content and canopy structure 107
6.3.4 Leaf-level FluoWat measurements 110
6.3.5 TOC reflectance and fluorescence 118
6.3.6 SCOPE: prove of fluorescence re-absorption 120
6.3.7 Concluding remarks 133
7 Recommendations for future campaigns 135
References 135

Acronyms and Abbreviations

aPAR	Absorbed Photosynthetic Active Radiation
C_{ab}	Chlorophyll a+b content
C_{ant}	Anthocyanin content
C_{ca}	Carotenoid content
CCN	Contract Change Notice
C_{dm}	Dry matter content
CIP	Campaign Implementation Plan
CKA	Campus Klein-Altendorf
C_s	Brown material fraction
C_w	Leaf water content
DAR	Data Acquisition Report
DEM	Digital Elevation Model
ESA	European Space Agency
ESTEC	ESA Technical Centre
ETR	Electron Transport Rate
F_{687}	Fluorescence at 687 nm
F_{760}	Fluorescence at 760 nm
FAPAR	Fraction of Absorbed Photosynthetic Active Radiation
Fc	Fractional covers
FLEX	FLuorescence EXplorer
FOV	Field-of-View
fqe	Fluorescence quantum yield
FWHM	Full Width at Half Maximum
G	Ground flux
GLT	Geometric Lookup Table
GPP	Gross Primary Productivity
H	Sensible heat flux
HYFLEX	HYperspectral FLuorescence EXperiment
HyPlant	Hyperspectral Plant imaging spectrometer
iFLD	Improved Fraunhofer Line Discrimination
LAI	Leaf Area Index
LE	Latent heat flux
LIDFa	Leaf angel distribution parameter which control the leaf slope
LIDFb	Leaf angel distribution parameter which control the distribution's bimodality
LUE	Light Use Efficiency
MERIS	Medium Resolution Imaging Spectrometer
MG	MinnGold
MTCI	MERIS Terrestrial Chlorophyll Index
N	Leaf thickness
NDVI	Normalized Difference Vegetation Index
NEE	Net Ecosystem Exchange
NIR	Near Infrared (spectral range)
PAR	Photosynthetic Active Radiation
PRI	Photochemical Reflectance Index
PSF	Point Spread Function

Reco	Ecosystem Respriration
ROI	Region of Interest
SFM	Spectral Fitting Method
SIF	Sun-induced fluorescence
SVD	Singular Vector Decompostion
SWIR	Short Wave Infrared
TOC	Top-Of-Canopy
u*	Friction velocity
V2Z	Maxumin carboxylation rate
VI	Vegetation Indices
VIS	Visible (spectral range)
WP	Workpackage
WT	Wild-Type

Reference Documents (RD)

[RD-1] ESA, 2015: Report for Mission Selection: FLEX, ESA SP-1330/2, European Space Agency, Noordwijk, The Netherlands.
[RD-2] EOP-PI/2008-05-83, An analysis of the synergy between FLEX and Sentinel-3.
[RD-3] FLEX/S3 Tandem Mission Photosynthesis Study, Final Report, ESA ESTEC ITT AO/1-7088/12/NL/AF, July 2014.
[RD-4] Technical Assistance for the Deployment of an advanced hyperspectral imaging sensor during SoyFLEX, Final Report, ESA Contr. No. 4000107143/12/NL/FF/If, CCN3, October 2017.
[RD-5] FLEX/Sentinel-3 Tandem Mission FLEX Bridge Study, Final Report, ESA ESTEC Contract No. 4000112341/14/NL/FF/gp, January 2016.
[RD-6] Technical assistance for the deployment of an advanced hyperspectral imaging senor during HYFLEX, Final Report, ESA Contr. No. 4000107143/12/NL/FF/If, April 2014.

1 Summary of main findings

1.1 The FLEX airborne demonstrator *HyPlant*: A high-performance imaging spectrometer to measure reflectance and sun-induced fluorescence

Acquisition of high resolution data by the *HyPlant* sensor were generally satisfactory and high performance reflectance data were acquired on all proposed study sites in Czech Republic, Germany and Italy. Both *HyPlant* sensor modules were fully operational and radiometric quality of the data is high and stable. In winter 2014/1015 *HyPlant* was technically improved, which resulted in a higher dynamic range and a greatly improved point spread function (PSF). The PSF of *HyPlant* showed a narrow and symmetrical shape with low tailing and a low stray light component, thus is was possible to record high quality at-sensor radiance data for fluorescence retrieval. In addition the geometric accuracy of the images was significantly improved compared to the previous years. It was suspected that a technical failure in the Oxford GPS/IMU unit could be the reason for the low accuracy in past campaigns. Thus, in the 2016 campaign the *HyPlant* sensor was operated with an Applanix unit of Czech Globe and a geometric accuracy of 1-2 pixels was achieved. In a parallel testing the sensor was operated with a new Oxford unit to evaluate a possible technical malfunctioning in this GPS/IMU unit. It was shown that both GPS/IMU units can provide of comparable quality. We are now sure that we have identified the technical failure and the *HyPlant* Oxford unit was send back to the manufacturer and after further intense technical investigation a microscopic hair fracture in one of the accelometers within the core of the IMU unit could be identified. The GPS/IMU unit was repaired in January 2017 and for future campaigns we will achieve higher accuracy using the *HyPlant* Oxford unit.

1.2 Fluorescence retrieval and automated processing routine of the spectral fitting method and fluorescence maps

The red and far-red fluorescence maps were computed by three retrieval methods, which are available for *HyPlant*. (1) The 'singular vector deconvolution' (SVD) uses solar Fraunhofer lines in the red and far-red spectral region to retrieve fluorescence. The SVD approach depends on the specific training-set and the fluorescence values generally are prone to a larger noise level. This method was applied as the default method for forest areas such as the experimental sites in Czech Republic. (2) The iFLD method was greatly improved in the past years and exploits the two O_2 bands in combination with non-fluorescing reference surfaces. In general, the iFLD fluorescence values show a very good agreement with ground measurements for different vegetation types. However, the retrieval requires non-fluorescence pixels, which makes it non applicable for e.g. large forest areas which have no non-vegetated gaps. Additionally, the iFLD method is prone to artifacts that may be caused by the reference pixels within the image. Nevertheless the iFLD remains the main method to retrieve fluorescence in most flight lines. (3) The 'Spectral Fitting Method' (SFM) was for the first time applied operationally on a larger data set of *HyPlant* and delivers first maps of sun-induced fluorescence that are based on the proposed retrieval method of the FLEX satellite mission (i.e. atmospheric RT modelling coupled with fluorescence retrieval). The processing work-flow architecture was developed towards the systematic processing of tens of imagery based on customized batch scripts to transfer data, submitting parallel-computing jobs on super-computer infrastructure, to retrieve products and compute basic quality statistics. Furthermore, the Spectral Fitting was also adapted to compute fluorescence of small areas based on reference tarps, allowing to produce maps even for non-optimal atmospheric conditions (i.e. SoyFLEX2). The maps produced by the SFM are satisfying, but further developments are recommended to consolidate and make the processing-chain operational through: i) consolidating pre-processing (i.e., non-linearity and PSF deconvolution); ii) developing topographic correction module; iii) developing an inverse scheme to retrieve atmospheric parameters directly from imagery itself.

1.3 SoyFLEX2 experiment: Forward modelling of canopy fluorescence emission

The SoyFLEX experiment was a repetition of an experiment that took place during the 2015 Campaign in Germany. In this experiment, two different varieties of soybean were planted: the standard 'wild type' variety named Eiko and the 'MinnGold' variety, which shows a greatly reduced amount of leaf chlorophyll content while having the same leaf area index and a similar growth. Thus, the two varieties mainly differ in leaf level chlorophyll content. In this study those two varieties were investigated to show how leaf chlorophyll content, canopy architecture, and photosynthetic efficiency affect top-of-canopy reflectance based vegetation reflectance and sun-induced fluorescence measurements. The dataset on leaf and canopy level was used as input for SCOPE modelling to better parameterize the reabsorption and escape probability of fluorescence in natural canopies and to identify the main parameters that influence canopy fluorescence emission.

When measuring the sun-induced fluorescence emission spectra on fully developed, sun exposed leaves located in the top layer of the canopy we observed that, Eiko present the same fluorescence emission as MinnGold for the red fluorescence peak at 680 nm. For the far-red fluorescence emission peak at 760 nm Eiko shows higher values than MinnGold. Those results are in line with the observation from the SoyFLEX experiment in 2015 [RD-4] and support results from the literature. Changes in the red fluorescence peak (F680) are associated with the plant photochemistry and the far-red fluorescence peak (F760) is related to the chlorophyll content and structural parameters.

However, top of canopy (TOC) sun-induced fluorescence values measured at ground and from the *HyPlant* airborne sensor show lower red fluorescence values (F687) for Eiko than for MinnGold, but a higher far-red fluorescence peak (F760) in Eiko than in MinnGold. The difference between leaf and TOC measurements may be due to the re-absorption of the fluorescence emitted within a leaf and in the canopy. Fluorescence that is emitted at 680 nm is greatly reabsorb by leaf pigments. Additionally, leaf fluorescence emitted at 680 nm at the bottom of the canopy is re-absorb by a leaf located in the upper-canopy.

Comparing the difference between leaf and canopy measurements we could conclude that the lower red fluorescence (F680) canopy values in Eiko are due to higher canopy re-absorption. By eliminating leaf and canopy re-absorption in SCOPE we could accurately recalculate the fluorescence emission at chloroplast level of both varieties despite their greatly different canopy structure.

Thus by using the experimental set-up of the two soybean varieties we could greatly contribute to our scientific understanding how (1) the fluorescence signal that is emitted at the chloroplast level is re-absorbed within the leaf and by the different canopy layers before reaching the sensor and (2). proved that sun-induced fluorescence can be used as a good indicator of plant photochemistry, once the effects due to reabsorption at leaf and canopy level are taken into account.

2 Introduction and Background

Vegetation monitoring has been one of the key objectives of many different satellite missions in the past. The FLuorescence EXplorer (FLEX) is the first satellite mission to be designed specifically for the measurement of passive sun-induced chlorophyll fluorescence in terrestrial vegetation [RD-1]. FLEX was selected in November 2015 as ESA's 8th Earth Explorer, to be launched in 2022 and to operate for 3 to 5 years in tandem with ESA's Sentinel-3 (S-3) (Drusch *et al.* 2016). The FLEX/S-3 tandem mission will support both the retrieval of sun-induced fluorescence and its interpretation through the acquisition of complementary and synergistic data [RD-2]. Sun-induced fluorescence and associated biophysical data products derived from the FLEX/S-3 mission will be used as additional information to quantify actual photosynthetic performance and stress responses for a range of applications spanning the fields of agriculture, forestry, and environmental science [RD-1]. Previous studies such as the FLEX/S3 Tandem Mission Photosynthesis Study [RD-3], developed a consolidated leaf-canopy SIF-photosynthesis model based on SCOPE (van der Tol *et al.* 2009). In addition, stress indicators were analysed, and a conceptual framework was proposed to guide stress detection using FLEX.

The previous HYFLEX campaign (Technical Assistance for the Deployment of an advanced hyperspectral imaging sensor during HYFLEX"; Contract No. 4000107143, CCN1, CCN2) supported the testing of the novel Hyperspectral Plant Imaging Spectrometer (*HyPlant*). Within the HYFLEX project maps of sun-induced chlorophyll fluorescence over different agricultural field sites, needle and broadleaf forest were presented. Results demonstrated the capability of *HyPlant* airborne data to test and evaluate different approaches to model and retrieve top-of-canopy (TOC) fluorescence and the possibility to study the physiological responds between fluorescence and photosynthesis. The HYFLEX campaign in 2015 ('Technical Assistance for the Deployment of an advanced hyperspectral imaging sensor during SoyFLEX'; CCN3) the analyses are extended to measurements of a dedicated experiment with two different soybean varieties. Due to the disease and poor growth of the soybean plant in 2015, only limited recorded data could be used for further analyses [RD-4]. Within this CCN4 the analyses of the two soybean varieties will be extended to gain reliable results for further scientific analyses. On addition two long-term monitoring sites namely, the agricultural TR32 site in Selhausen (Germany) and the forest Bílý Kříž site (Czech Republic).

3 Campaign objectives

The overall objectives of the CCN4-funded activity as they are specified by the SOW are

- **Objective 1**: Acquire and process high quality hyperspectral datasets of fluorescence in conjunction with extended correlative data and
- **Objective 2**: Perform initial analyses of data quality and generate first estimates of fluorescence
- **Objective 3**: Complement the measurements from the soybean mutants from 2015. The data from 2015 look very promising, however not all components were acquired successfully. These missing elements should be recorded this year.
- **Objective 4**: Provide feedback for existing state of the art fluorescence models. The dataset shall be utilized in the framework of this activity to test and evaluate different modelling approaches that simulate and retrieve top-of-canopy fluorescence
- **Objective 5**: Understand if fluorescence enables the detection of differences in canopy gas exchange of different crop species and at different times of the day
- **Objective 6**: Provide a concise and complete set of experimental data to better understand the mixing of the fluorescence signal within the canopy (from the leaf to the top-of-canopy signal)
- **Objective 7**: Establish a data analysis routine that allows to calculate two peak fluorescence maps as well as totally integrated fluorescence emission from *HyPlant* data from a larger set of flight lines.
- **Objective 8**: Complete the time series of Selhausen und Bílý Kříž measurements by continuing the measurement concept from the years 2012-2015. [no ESA funding was provided for this component][1]

[1] This is already covered by a bilateral campaign between Forschungszentrum Jülich and Czech Globe. The partners agreed that these data will be made available to ESA, however, no detailed reporting of this component will be done in this document.

In abovementioned objectives are used to structure this report:

Objective 1 and **Objectives 2** was completely fulfilled by recording the long term experimental sites in Germany (chapter 5.1) and Czech Republic (chapter 5.2). For both sites a high quality dataset was recorded, from which maps of different vegetation indices and sun induced fluorescence were calculated (chapter 6.1). With the recording and data analyses of the two long term study sites in Jülich/Selhausen and Bílý Kříž also **Objective 8** is fulfilled.

Objective 3 was completely fulfilled. The SoyFLEX2 experiment which was repeated and set-up in Udine, Italy was recorded with the *HyPlant* sensor several times around solar noon on consecutive days (chapter 5.3). Correlative ground data were taken accordingly (chapter 4.2).

Objective 4 and **Objective 6** were fulfilled with the analyses of the SoyFLEX2 experiment in chapter 6.3. The acquired dataset of hyperspectral reflectance and fluorescence data on leaf-level (chapter 6.3.4), top-of-canopy level (chapter 6.3.5) and airborne level (chapter 6.2 and 6.2.3) were used as input for a state-of--the-art fluorescence model (SCOPE).

Objective 5 was fulfilled by recording the canopy gas- exchange measurements (chapter 4.2.7), which additional serve as a validation dataset for the SOYFLEX2 experiments (chapter 6.3.2).

Objective 7 was completely fulfilled. The main improvements of the fluorescence retrieval, especially for the S*pectral Fitting Method* were already reported in 2015. The detailed description of the method is described in the final report of 2015, along with the detailed evaluation of the maps. As a main outcome of this activity, the *Spectral Fitting Method* is now operational and ready to produce/calculate red and far-red fluorescence maps also from numerous flight lines and from larger maps (chapter 6.1.1.1 and 6.2.3)

4 Instrumentation, material and methods

In this chapter and overview of the main instrumentation, material and methods used is given. Table 1 summarizes the equipment and the following subchapters give a detailed description about each material and method.

Table 1: Instrumentation during SOYFLEX2 campaign in Germany and Poland.

	Germany	**Poland**
Airborne	*HyPlant,* TASI	*HyPlant,* TASI
Atmospheric characterization	MICROTOPS sun photometer Radio sounding	MICROTOPS sun photometer
Ground reference (Cal/Val)	ASD Field Spec	ASD Field Spec
TOC reflectance and fluorescence	Ocean Optics spectrometers	Ocean Optics spectrometers
Leaf level reflectance and fluorescence	FLUOWAT+ASD Field Spec	FLUOWAT+ ASD Field Spec
Gas exchange and meteorological measurements	gas exchange chamber Eddy Covariance Meteorological stations	gas exchange chamber Eddy Covariance
Biochemical and structural parameter	Leaf chlorophyll content Leaf Area Index, fAPAR	

4.1 Airborne sensor *HyPlant*

The *HyPlant* sensor is a hyperspectral imaging system for airborne and ground-based use. It consists of two sensor heads. The DUAL module is a line-imaging push-broom hyperspectral sensor, which provides contiguous spectral information from 370 to 2500 nm in one device utilizing a common fore objective lens with 3 nm spectral resolution in the VIS/NIR spectral range and 10 nm spectral resolution in the SWIR spectral range. The vegetation fluorescence signal is measured with a separate push-broom sensor, the FLUO module, which produces data at high spectral resolution (0.25 nm) in the spectral region of the two oxygen absorption bands. The Data Acquisition and Power Unit contain two rack modules. The first module includes the data acquisition computer with system control and data acquisition software and the power supply and control electronics for the DUAL module and GPS/INS sensor. The second module includes the same equipment for the FLUO module. The Position and Altitude Sensor (GPS/INS sensor) provides, synchronously with the image data, aircraft position and attitude data for image rectification and geo-referencing. Both imagers (DUAL and FLUO module) are mounted in a single platform with the mechanical capability to align the field of view (FOV) (Figure 1).

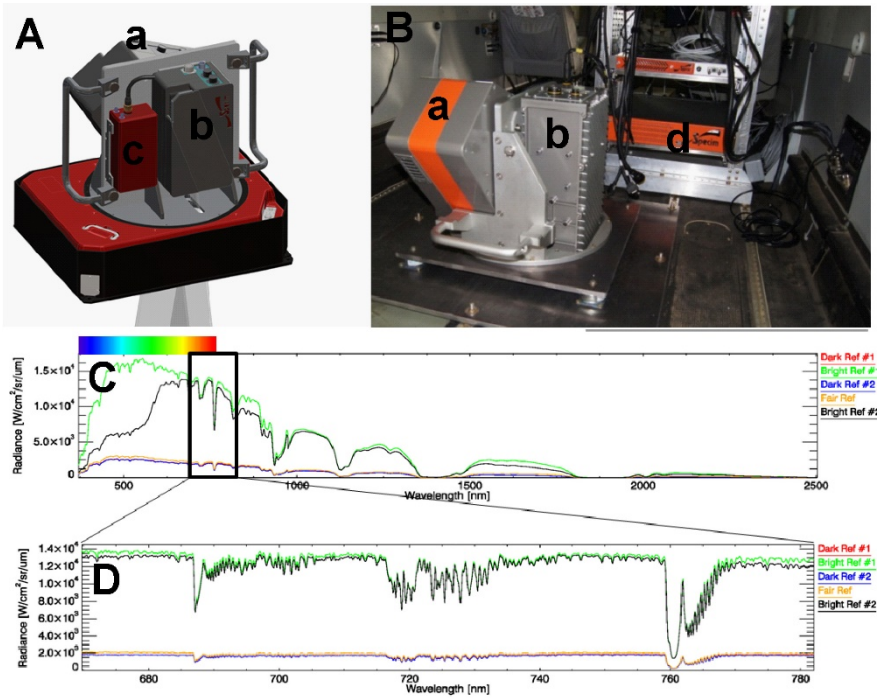

Figure 1: Schematic drawing of the *HyPlant* sensor consisting of the broad band dual module (a) and the high resolution fluorescence module (b). Additionally, the GPS/IMU positioning unit that is attached to the rack is shown (c). B: Installation of *HyPlant* within a Cessna aircraft. In the back the data acquisition unit is visible (d) C, D: Representative radiance measurements from different surfaces from the DUAL and the FLUO module, respectively.

The *HyPlant* sensor deployed during the campaigns in 2013/2014 (*HyPlant_1*) showed a very wide point spread function (PSF). This revealed a relatively bad PSF that was caused by wrong glue between two essential optical elements of the detector (wrong chemical formula of the glue that caused great scattering at an optical element). As a consequence the optical path of the spectrometer was exchanged and upgraded in winter 2014 / 2015 (*HyPlant_2*). After the technical improvements the FLUO module has a greatly improved narrow and rather symmetrical PSF (Figure 2). Nevertheless, a deconvolution has to be implemented in pre-processing to minimize the spatial cross talk of photons between pixel elements ('spill over'). In order to remove the effect of the PSF from the measured data it is necessary to independently process each image line acquired. For this a dedicated deconvolution algorithm was developed by University of Valencia, which is implemented in the processing chain (Figure 3).

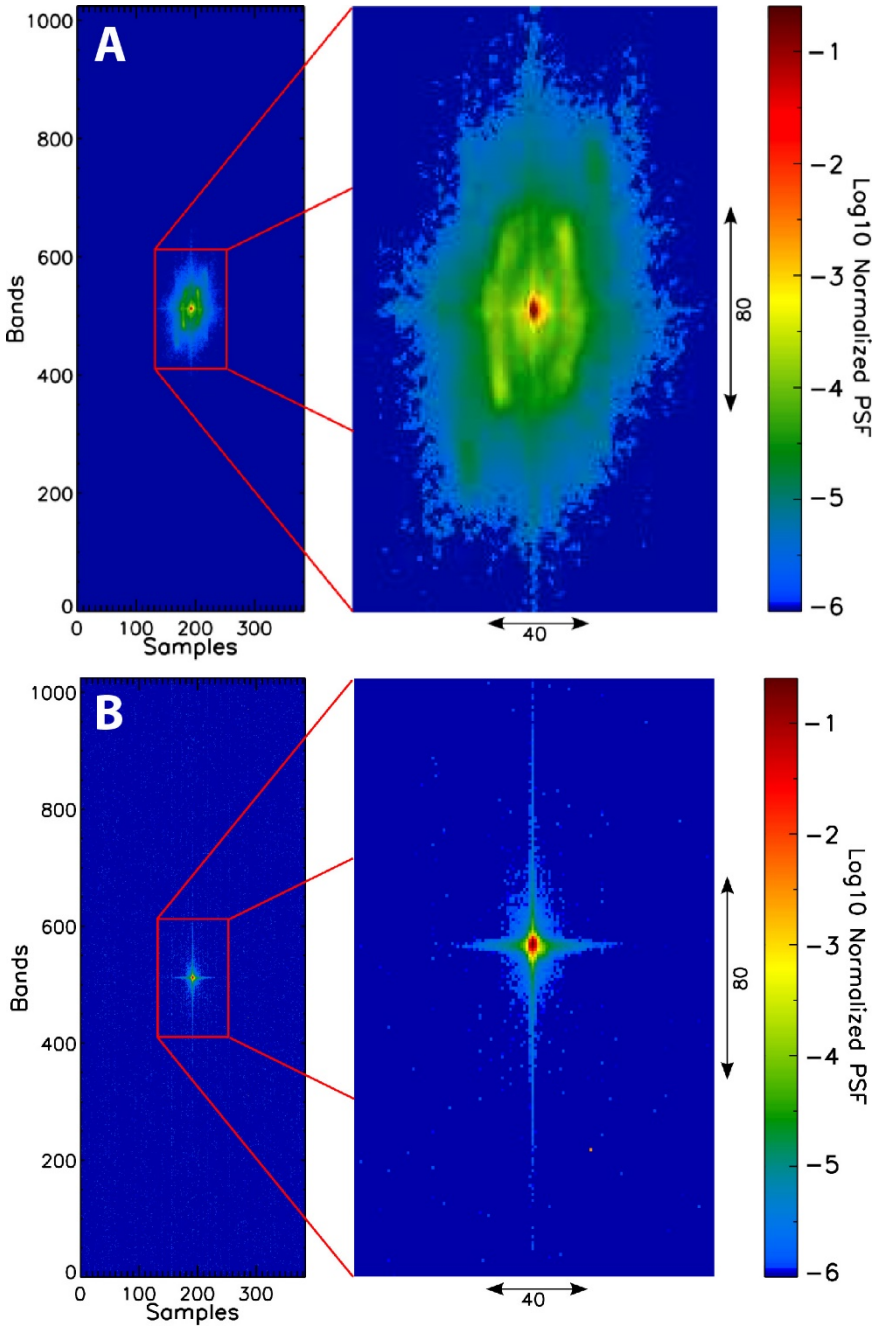

Figure 2: Point spread functions (PSF) of FLUO. A: PSF of the sensor for the calendar years, 2013 and 2014 (*HyPlant_1*), B: PSF of the calendar years 2015 ff (*HyPlant_2*). The PSF was greatly improved in winter 2014 / 2015 by exchanging a wrongly clued optical element in the spectrometer. The PSF is normalized to the total energy and represented in log scale. On the left is the full sensor frame. On the right is the magnified extension of the PSF. Note that typical sensor noise is in the order of 10^{-5} in this scale.

4.1.1 *HyPlant* data processing

HyPlant consists of two modules, each of which delivers its own data stream. Pre-processing of the two data streams has specific requirements, which are derived from the specific output and specific products of the two modules. The *HyPlant* processing chain (Figure 3) gives an overview on the single processing steps of the FLUO and DUAL module, from raw data to final products, such as vegetation indices and fluorescence maps.
First steps of the pre-processing is done for both module with CaliGeoPro, the software that was developed by the manufacturer of *HyPlant* (SPECIM, Finland). CaliGeoPro is used for the wavelength and radiometric calibration of both modules. Therefore, the most recent calibration files from the calibration in winter 2014/2015 at Specim was used. We compared the calibration files from the last years and found that the radiometric and wavelength calibration is rather stable. Therefore, it was decided that the calibration filed from 2015 can also be used for the 2016 dataset. Also the geometric correction is applied with the CaliGeoPro software using the boresight angles evaluated in chapter 4.1.2.
An additional pre-processing step of the FLUO module is the deconvolution of the PSF given in Figure 2. Subsequently red and far-red fluorescence maps are calculated from the deconvoluted FLUO data. A description of the three different fluorescence retrieval methods is given in chapter 4.1.1.2.
The radiometrically corrected DUAL data are atmospherically corrected to Top-of-Canopy (TOC) reflectance data using the ATCOR. Subsequently, different vegetation indices given in chapter 4.1.1.1 are calculated as a default.

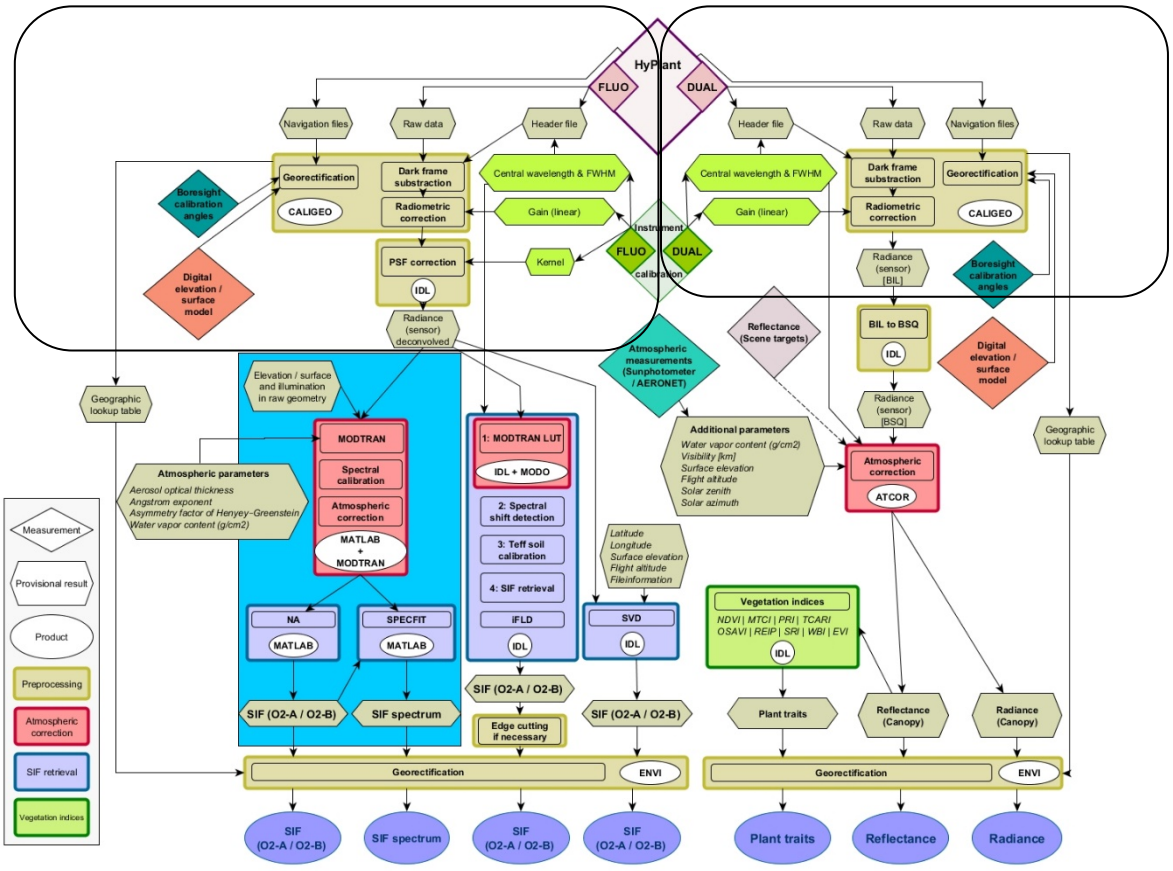

Figure 3: *HyPlant* processing chain, including FLUO and DUAL module.

The main processing steps are labelled in the file name of the flight line (Table 2). Each file name contains the acquisition date, area and time, as well as information about the flight altitude from which

the ground pixel size can be concluded. As basic information the name of the flight line, heading of the aircraft during the acquisition and from which module (DUAL or FLUO) the flight line was recorded is given as well. When the radiometric and wavelength calibration are applied to the flight line, the label *radiance* is added. The atmospheric correction of the DUAL data is done using ATCOR. Top-of-canopy (TOC) radiance files are stored with the *img_surfrad*; TOC reflectance files where in addition spectral polishing and smile correction was applied are labelled with *img_atm_polish_smcorr*. From the TOC reflectance data vegetation indices (see chapter 4.1.1.1) are calculated and labelled with the label *indices_up*. For the FLUO module the label *deconv_i1* indicated that the deconvolution of the spectra to correct the point spread function. The Label *Fs_linear_v2* indicates the fluorescence maps were calculated with the SVD method. The label *FIXDEM_V5* shows that the maps were calculated with the iFLD method. In case the label is *FIXDEM_V3.2* the brightness correction of the IFLD method was applied. The fluorescence maps calculated with the SFM are stored in two different files, marked with the label *SIFO2A* and *SIFO2B* for the two absorption bands. *HyPlant* modules the label *rect* indicate that the calculated product was georectified.

Table 2: The file name for each flight line recorded of the *HyPlant* has the following format. Final products are marked as bold.

Acquisition date	**Acquisition area**	**Recording time (local)**	**Flight altitude**	**Module of the sensor**	**Processing steps DUAL**	**Processing steps FLUO**
YYYYMMDD	-BK (Bily Kriz; Figure 35, Figure 36)	-hh:mm	-0350 (0.5 x 1m)	-FLUO	-radiance (radiometric calibration file of SPECIM was applied)	-radiance (radiometric calibration file of SPECIM was applied)
	-TR32 (large TR32 map; Figure 32)		-0600 (1m x 1m pixel)	-DUAL	**-img_surfrad** **(atmospherically corrected radiance data)**	-deconv_i1 (deconvolution of the spectra to correct the point spread function)
	-SEL (Selhausen; Figure 33)		-1800 (3m x 3m pixel)		**-img_atm_polish_smcorr** **(atmospherically corrected reflectance data, with applied spectral polishing and smile correction)**	**-FIXDEM_V5 (fluorescence maps calculated with the iFLD method)** **FIXDEM_V3.2 (fluorescence maps calculated with brightness correction of the iFLD method)**
	-CKA (research campus Klein-Altendorf; Figure 34)				**-indices_up** **(calculation of selected vegetation indices)**	**-Fs_linear_v2 (fluorescence maps calculated with the SVD method)**
	-SOY (Back-up soya field at campus Klein-Altendorf; Figure 34)				**-rect** **(georectification using the GLT file)**	**-SIFO2A and –SIFO2B (fluorescence maps calculated with the SFM)**
	-UDI (Udine; Figure 37)					**-rect (georectification using the GLT file)**

4.1.1.1 Top-of Canopy Reflectance and Vegetation Indices

Data from the DUAL module was also processed to geo-rectified a-sensor radiance using Caligeo and the Specim provided calibration files (Figure 3). Subsequently, data were atmospherically corrected using ATCOR and top-of-canopy (TOC) radiance and reflectance was stored. From the TOC reflectance data selected vegetation indices were calculated according to formula (1)-(12).

Indices related to chlorophyll content and leaf area index

Simple Ratio (SR)

The simple ratio (SR, formula (1)) shows a ration between near infrared and the red spectral region and enhances the contrast of soil and vegetation (Asrar *et al.* 1984).

$$SR = \frac{R_{<795-810>}}{R_{<665-680>}} \quad (1)$$

The spectral windows correspond to 9 bands in *HyPlant* (center wavelength ± 4 bands).

Normalized Difference Vegetation Index (NDVI)

The Normalized Difference Vegetation Index (NDVI, formula (2)) can theoretically accept values from -1 to 1. Green and dense forest vegetation shows high NDVI values. It should be noted that the NDVI saturates with high Leaf Area Index (LAI< 5) (Rouse *et al.* 1973).

$$NDVI = \frac{R_{<795-810>} - R_{<665-680>}}{R_{<795-810>} + R_{<665-680>}} \quad (2)$$

The spectral windows correspond to 9 bands in *HyPlant* (center wavelength ± 4 bands).

Red-edge Normalized Difference Vegetation Index ($NDVI_{re}$)

The Red-edge Normalized Difference Vegetation Index ($NDVI_{re}$, formula (3)) is a modification of the traditional broadband NDVI. This VI differs from the NDVI by using bands along the red edge, instead of the main absorption and reflectance peaks. It capitalizes on the sensitivity of the vegetation red edge to small changes in canopy foliage content, gap fraction, and senescence. The value of this index ranges from -1 to 1. The common range for green vegetation is 0.2 to 0.9 (Gitelson and Merzlyak 1994; Sim *et al.* 2002).

$$NDVI_{re} = \frac{R_{<735-750>} - R_{<695-710>}}{R_{<735-750>} + R_{<695-710>}} \quad (3)$$

The spectral windows correspond to 9 bands in *HyPlant* (centre wavelength ± 4 bands).

Enhanced Vegetation Index (EVI)

The Enhanced Vegetation Index (EVI, formula (4)) is a VI that is more sensitive to areas with high biomass and should minimize the influence of the background signal and atmospheric influences (Huete *et al.* 2002).

$$EVI = 2.5\left[\frac{R_{<795-810>} - R_{<665-680>}}{R_{<795-810>} + 6 \cdot R_{<665-680>} - 7.5 \cdot R_{<475-490>} + 1}\right] \quad (4)$$

The spectral windows correspond to 9 bands in *HyPlant* (centre wavelength ± 4 bands).

Red-Edge Position (REP)

This Red-Edge Position (REP, formula (5, 6)) index is a narrowband reflectance measurement that is sensitive to changes in chlorophyll concentration. Increased chlorophyll concentration broadens the absorption feature and moves the red edge to longer wavelengths (Dawson and Curran 1998).

$$R_i = \frac{R_{<665-680>} + R_{<795-810>}}{2} \qquad (5)$$

The spectral windows correspond to 9 bands in *HyPlant* (center wavelength ± 4 bands).

$$REP = 700 + 40\,\frac{R_i - R_{700}}{R_{740} - R_{700}} \quad \text{[nm]} \qquad (6) \text{ with } (5)$$

The result is a wavelength that indicates the position of the inflection of the red edge.

MERIS terrestrial chlorophyll index (MTCI)

The MERIS terrestrial chlorophyll index (MTCI, formula (7)) provides information on the chlorophyll content of vegetation. This is a combination of information on leave area index. The MTCI correlates strongly with chlorophyll content when using model, laboratory and field spectrometry data (Dash and Curran 2007).

$$MTCI = \left(\frac{R_{754\pm7.5} - R_{709\pm10}}{R_{709\pm10} - R_{681\pm7.5}}\right) \qquad (7)$$

This index is developed for MERIS and thus we here give the central wavelengths and the widths that correspond to the MERIS bands. We aim to represent the spectral resolution of MERIS and thus we propose to use 9 bands (center wavelength ± 4 bands) for the 681 and 754 nm (app. 15 nm spectral window) and 11 bands (center wavelength ± 5 bands) for the 709 nm (app. 20 nm spectral window) in *HyPlant*.

Transformed Chlorophyll Absorption in Reflectance Index (TCARI)

The Transformed Chlorophyll Absorption in Reflectance Index (TCARI, formula (8)) indicates the relative abundance of chlorophyll. It is affected by the underlying soil reflectance, particularly in vegetation with a low LAI (Haboudane *et al.* 2002).

$$TCARI = 3\left[(R_{700\pm4} - R_{670\pm4}) - 0.2 \cdot (R_{700\pm4} - R_{550\pm4}) \cdot \frac{R_{700\pm4}}{R_{670\pm4}}\right] \qquad (8)$$

TCARI is developed to use a smaller spectral window for the single bands and various definitions are available in the literature. Thus, we propose to use a smaller spectral windows corresponding to 5 bands (app 8 nm spectral window) in *HyPlant* (center wavelength ± 2 bands).

<u>Indices related to photosynthesis and non-photochemical quenching</u>

Photochemical Reflectance Index (PRI)

The photochemical reflectance index (PRI, Formula (9)) is related to the non-photochemical quenching (NPQ) of the vegetation and should therefore be positive related to the light use efficiency of the vegetation canopy. The interpretation of the PRI sometimes remains difficult, as the VI is sensitive to structural and illumination effects.

$$PRI = \frac{R_{<570\pm2.5>} - R_{<531\pm2.5>}}{R_{<570\pm2.5>} + R_{<531\pm2.5>}} \qquad (9)$$

This is the original formula as proposed by Gamon *et al*. (1992). In this expression, the PRI correlates positively with NPQ. For the reference wavelength at 570nm we propose to use a spectral window of app. 5 nm (3 bands in *HyPlant*, centre wavelength ± 1 bands). For R_{531} we propose to use a similar spectral window of app. 5 nm (3 bands, centre wavelength ± 1 band).
The motivation comes from the study in FLEX-Bridge [RD-5]. There it became clear that the spectra are noisy and spectral binning seems to be an appropriate option to compensate for noise since the reflectance change caused by NPQ around 531 nm are relatively "broad". However, the reference wavelength (570 nm) seems to be affected by certain features as well, means is spectrally less stable than expected. So we recommend to use only 3 bands (centre +/- 1 band) to avoid further sensitivities of the PRI for e.g, pigment pool sizes.

Canopy Photochemical Reflectance Index (cPRI)
According to the FLEX-Bridge study [RD-5], Wu *et al.* (2015) is the most promising canopy PRI index, less sensitive for pigment pool sizes, structural and atmospheric effects. Thus, we calculate the cPRI (modified after Wu *et al.* 2015).

$$cPRI = PRI - 0.15(1 - e^{-0.5 \cdot LAI}) \qquad (10) \text{ with } (9)$$

In the original formulation (eq. 10) the LAI needs to be known. We propose to use the Simple Ratio (eq. 1) as approximation for LAI. Thus the formula that should be finally included in the processing module is eq. 11. The additive term of 0.2 originally proposed by Wu *et al.* (2015) is sensor specific and thus is omitted in the formula to be implemented for *HyPlant*.

$$cPRI = \frac{R_{<570\pm2.5>} - R_{<531\pm2.5>}}{R_{<570\pm2.5>} + R_{<531\pm2.5>}} - 0.15\left(1 - e^{-0.5 \cdot \frac{R_{<795-810>}}{R_{<665-680>}}}\right) \qquad (11) \text{ with } (9)$$

Again, for both PRI wavelengths at 530nm and 570nm we propose to use a spectral window of app. 5 nm (3 bands in *HyPlant*, center wavelength ± 1 bands). For the SR, both spectral windows (i.e., 795-810 and 665-680) correspond to 9 bands in *HyPlant* (center wavelength ± 4 bands).

Indices related to canopy water content

Water Band Index (WBI)
The Water Band Index (WBI, formula (12)) is a simple ratio index that is sensitive to differences in canopy water status. An increase in the canopy water content is reflected as a higher absorption at 970 nm relative to the 900 nm reference band (Peñuelas *et al.* 1993).

$$WBI = \frac{R_{<955-970>}}{R_{<890-905>}} \qquad (12)$$

The spectral windows correspond to 9 bands in *HyPlant* (center wavelength ± 4 bands). These spectral windows are at the very edge of the VIS/NIR module; the last waveband of the VIS/NIR module of *HyPlant* is at 969.1nm. We thus propose to use the last 9 bands of the VIS/NIR camera for calculating the spectral window <955-970>.

4.1.1.2 Fluorescence retrieval

All FLUO module flight lines acquired within the FLEX-EU campaign were processed to geo-rectified at-sensor radiance data using the most recent wavelength and radiometric calibration file provided by the Specim in winter 2014/2015. The Point Spread Function (PSF) correction as described in chapter 4.1 and Figure 2 was applied to each of the fluorescence flight lines and is also based on calibration measurements of 2015.

Improved Fraunhofer Line Descrimination (iFLD)

Fluorescence maps of red and far-red fluorescence of the agricultural areas of Germany (chapter 5.1.1 and 5.1.2) were calculated using the improved Fraunhofer Line Discrimination (iFLD). The method is based on the 3-FLD approach by Maier *et al.* (2003) and the iFLD method of Alonso *et al.* 2008. The method was adapted to the high spectrometers, complemented with the simulations of atmospheric components using MODTRAN (Berk et al 2005). In addition an empirical constrain based on reference non-vegetation surfaces is used after Damm et al. (2014). Therefore the method can only be used for flight lines with sufficient non-vegetation reference pixels available across track of the flight line. The detailed description and formulation is given in the Final report 2015 [RD-4]. To improve especially the estimation of the atmospheric parameters are rather theoretical and in non-stable atmospheric conditions, do not always yield to a proper path scattered radiance, which is determined by the aerosol optical thickness. An underestimation of the path scattered radiance results in an underestimation of the fluorescence in bright targets and a false fluorescence in dark target and shadows. Therefore a brightness correction was included in the algorithm.

Singular Vector Decomposition (SVD)

Fluorescence values at 680 nm and 740 nm can be obtained using the Singular Vector Decomposition (SVD). The method is based on a semi-empirical radiative transfer formulation and was first developed by Guanter *et al.* (2012, 2013). The method was previously used for fluorescence retrieval from *HyPlant* recordings in Rossini *et al.* (2015). The data-driven fluorescence retrieval approach represents the measured at-sensor radiance spectrum as a linear combination of reflected solar radiance and fluorescence emission spectra. The reflected solar radiance is formulated as a linear combination of singular vectors (SVs), which are derived after performing a Singular Vector Decomposition of a set of reference (fluorescence-free) spectra. The combination of the derived SVs is able to reproduce any fluorescence-free spectra. This data-driven formulation of the forward model avoids the explicit modelling of atmospheric radiative transfer and the instrument's spectral and radiometric responses, which are typically prone to errors larger than the fluorescence signal itself. The SVs are derived using non-fluorescence training pixels, which are determined by a threshold on the Normalized Difference Vegetation Index (NDVI). We typically used 4–5 SVs to model the "at-sensor" radiance signal. A few adjustments were applied to improve the inversion results, such as the removal of the strongest absorption features or the spectral normalization (continuum removal) of canopy and reference radiances. This method was used to derive the fluorescence maps of the Bílý Kříž forest area recorded in Czech Republic.

Spectral Fitting Method (SFM)

The fluorescence retrieval code based on Spectral Fitting (SF) has been slightly modified from the earlier version [RD-4] used to process *HyPlant* flight lines collected during the 2015 campaign. The improvements do not concern the underling physical approach, but they involve only some technical implementation of the code to facilitate the displaying, understanding and interpreting of results. The novel implementation is intended to give more information to evaluate atmospheric RT forward modelling, point-spread-function (PSF) deconvolution and fluorescence retrieval modules performances. In particular, the theoretical upper/lower bounds were removed within the least square optimization routine included in the Spectral Fitting. The image columns not processed because incomplete deconvolution of PSF (left/right edges) were set to value -999 (instead of 0), avoiding to confuse them with retrievals of non-fluorescence surfaces. This

modification permits to better analyse the distribution of fluorescence values around zero, and sometimes negative, for better evaluating uncertainties in the PSF deconvolution, atmospheric correction and fluorescence retrieval modules. The novel code version v15 (HYPLANT_FLUO_v15A.m and HYPLANT_FLUO_v15B.m) uses 16-bit signed integer (int16) number format to store final maps product, instead of unsigned integer (uint16) used in past versions.

The second objective involved the development of a systematic, robust and semi-automated processing of a large number of airborne flight lines. This was aimed to produce the first large-scale spatial composite map (TR32 mosaic, see chapter 6.1.1.2). The work-flow architecture was designed toward a future massive processing of *HyPlant* data sets. The Spectral Fitting code enables parallel-computing approach and it was initially scaled on high-performance computer (HPC) infrastructure (Galileo HPC, Cineca consortium). The shared memory parallel library Open Multiprocessing (OpenMP) is implemented and operational, allowing to process a single *HyPlant* image line (i.e. 384 column pixels) within 1 second by using 16 processing cores. A medium-length *HyPlant* imagery (e.g. 5000 lines) can be processed about within 80 minutes. The further developments envisaged shall cover the implementation and testing of message passing interface (MPI) library to theoretically scale-up the retrieval algorithm on 384 processing cores. It should give process single *HyPlant* line (384 pixels) in < 0.1 seconds and the entire image within 10 minutes. It must be noted that the fluorescence retrieval processing at O_2-A and O_2-B, as well different imageries, can be submitted as separated/parallel jobs, strongly reducing the time required to produce large spatial composites.

Finally, the Spectral Fitting approach has been further adapted to use reference targets within the imagery to provide fluorescence maps of small area that, for the moment, can be used to process *HyPlant* imagery collected with not-optimal illumination (atmospheric) conditions.

4.1.2 Georectification of *HyPlant* images

From 2012 to 2015 the *HyPlant* sensor was operated with its Oxford GPS/IMU unit. However, the georectification of the flight lines did not show a high accuracy and even an increasing error during the 2015 campaign [RD-4]). The direct comparison of the positioning angel between the Applanix unit from CzechGlobe and the Oxford *HyPlant* unit in 2015 revealed a significant differences between Oxford and the Applanix systems for heading and especially the roll angle.

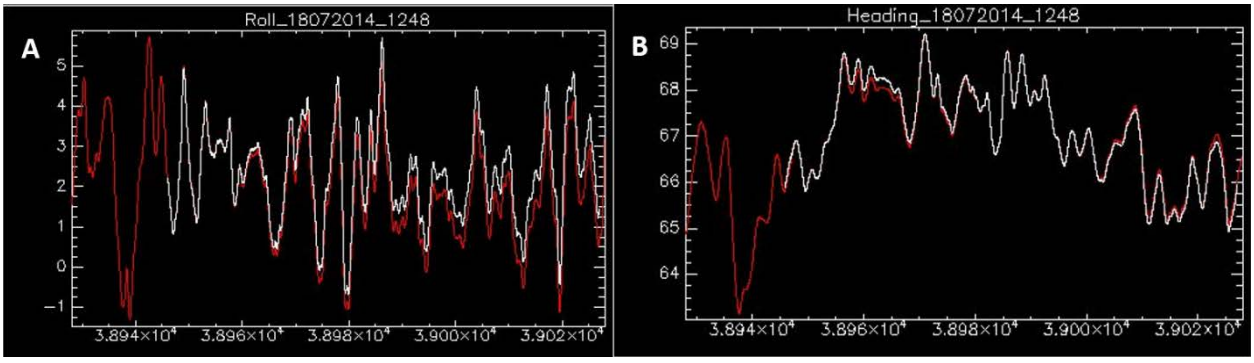

Figure 4: Direct comparison of the three position angles roll (A) and heading (B) as well as the altitude (D). Red line indicates the measurements of the Oxford unit and the white line the Applanix unit.

During the 2016 SyoFLEX2 campaign the *HyPlant* sensor was operated as a default with the Applanix unit from CzechGlobe. In addition, a new Oxford unit (provided by the manufacturer for test purposes) was mounted on the *HyPlant* mount to evaluate the if the inaccurate georectification of the *HyPlant* flight lines

is a general problem when using any Oxford 300 unit, or if there is a specific malfunctioning of the specific Oxford *HyPlant* unit.

Evaluation of the accuracy of the *HyPlant* georectification with the Oxford/Applanix units:

The accuracy of the georectification of *HyPlant* images with the Oxford and Applanix IMUs was evaluated on the boresight pattern acquired on July 18th, 2016 in Germany.
The boresight pattern consists of four flight lines (Figure 5), that were recorded once with the Oxford lend unit attached to *HyPlant* and once with the Applanix unit.
The three flight lines forming the external triangle were used for the calculation of the boresight angles, while the central east-west flight line was used to evaluate the accuracy of the georectification.
For these purposes, ground control points (GCPs) were acquired in correspondence of each overlap and along the validation line.

Figure 5: Boresight pattern acquired in Germany in 2016. GCPs are marked in yellow.

The accuracy assessment was performed on the four validation flight lines (i.e., DUAL and FLUO recorded with the Oxford IMU; DUAL and FLUO recorded with the Applanix IMU) that were georectified using the boresight angles previously calculated.
The mean absolute positioning error for each validation flight line was calculated as the mean Root Mean Square Error

$$RMSE = \sqrt{\Delta x^2 + \Delta y^2} \qquad (12)$$

between the geographic coordinates of 20 GCPs and of the corresponding points identified on the images. The same 20 GCPs were used for both the DUAL and FLUO modules and for both the IMUs(Figure 6).

Figure 6. Position of the 20 GCPs used for the accuracy assessment.

The results of the evaluation are reported in Table 3.

Table 3. Results of the evaluation of the absolute error of the DUAL and FLUO images acquired with the Oxford and Applanix IMUs. Δx and Δy are the mean differences between the geographic coordinates (Long, Lat) of the GCPs and the corresponding points identified on the images. RMSE is a mean value of the Root Mean Square Errors calculated for each point.

	OXFORD			APPLANIX		
	Δx	**Δy**	**RMSE**	**Δx**	**Δy**	**RMSE**
DUAL	1.4295	0.6837	1.6758	1.6841	0.7271	1.9580
FLUO	1.4797	0.7641	1.7298	1.2649	0.8265	1.7211

The mean relative error between DUAL and FLUO acquired with the Oxford and with the Applanix was calculated as the mean RMSE between the geographic coordinates of the same points identified on the DUAL and FLUO images respectively. The relative error was calculated using the same 20 points in which the absolute error was evaluated. The results are reported in Table 4.

Table 4. Results of the evaluation of the relative error between DUAL and FLUO with the Oxford and with the Applanix IMUs. Δx and Δy are the mean differences between the geographic coordinates (Long, Lat) of the same point identified on the DUAL and on the FLUO image. RMSE is a mean value of the Root Mean Square Errors calculated for each point.

	OXFORD			APPLANIX		
	Δx	**Δy**	**RMSE**	**Δx**	**Δy**	**RMSE**
DUAL vs FLUO	0.4108	0.1451	0.4626	0.9870	0.3959	1.0937

In terms of absolute errors, the performances of the Oxford and the Applanix unit are comparable. The positioning error ranges from 1.68 to 1.96 m. The slight differences observed between Oxford and Applanix unit are of the same order, or even lower, than the ones observed between DUAL and FLUO, indicating that most likely they are not related to a real difference in the performances of the instruments but to other

factors (e.g., retrieving of the boresight angles, accuracy of the GCPs, errors in the positioning of the GCPs on the images).
In terms of relative errors, the Oxford unit seems to perform better than the Applanix unit. In fact, the Oxford unit allows to obtain overall a sub-pixel accuracy in the overlap between DUAL and FLUO, while with the Applanix a shift of ~1 pixel is observed. Again, the influence of other factors affecting both the georectification itself and the accuracy assessment must be taken into account for a proper evaluation of the results. Nevertheless, the analysis performed until now did not highlight a significant superiority of one of the two systems.

On the basis of this evaluation it seemed very likely, that there is some kind of specific malfunctioning with the specific Oxford *HyPlant* unit. The Oxford *HyPlant* unit was send back to the manufacturer in winter 2016/2017. After intensive testing a microscopic hair fracture in one of the accelometers within the core of the IMU unit could be identified for a false recording of the role angle. The Oxford *HyPlant* GPS/IMU unit was repaired in January 2017, intensively tested and is now again implemented within the HyPlant measurement package for future campaigns and we are sure that higher accuracy will be achieved in the future.

All data from this report were acquired while *HyPlant* was operated with the Applanix unit from CzechGlobe. The boresight angles were derived from a boresight pattern (Figure 5) that was recorded at the beginning of the campaign in Germany. The boresight angles are given in Figure 4. The accuracy is within 1-2 pixels as evaluated within the chapter.

Table 5: Boresight angles of the Applanix unit for the DUAL and FLUO module evaluated from the boresight flights in Jülich, Germany using tie points.

	DUAL	**FLUO**
Roll	0.33614448	0.27356222
Pitch	-2.0228040	-0.42738688
Yawn	-0.10279960	0.19702741

4.1.3 TASI: Hyperspectral thermal sensor

The TASI-600 sensor is a 32 bands hyperspectral pushbroom sensor in the 8.0-11.5 µm spectral range, with a swath of 600 pixels for a FOV of 40° and an IFOV of 1.2 mrad. TASI was installed during the whole campaign window and operated in parallel with *HyPlant* sensor (Figure 7).
However, the processing of the data will not be highest priority, and only single flight lines will be processed content related.

Figure 7: *HyPlant* installed in the front and TASI sensor senor in the second hatch.

4.1.4 Airborne platform

The aircraft identified for these operations is a Cessna Grand Caravan C208B with dual camera hatches Figure 8 owned and operated by Czech Globe. The aircraft gives us the flexibility to use one aircraft company for multi sensor survey, as such optimizing flight times.

Figure 8: Cessna Grand Caravan C208B (Czech Globe).

4.2 Correlative ground equipment

4.2.1 Imagine hyperspectral instruments for top-of-canopy measurements

As part of the German Plant Phenotyping Network (DPPN) the Forschungszentrum Jülich is building a new automated positioning system for high throughput plant phenotyping. To support the mobile platforms initiative as well as the European Space Agency's Flex-satellite mission, HyScreen (Figure 9), a new hyperspectral imaging system for ground-based measurements of sun Induced fluorescence and hyperspectral reflectance was developed. By using HyScreen, which mimick *HyPlant* characteristics, we aim to improve our understanding of fluorescence signal (i.e spatial variability, contribution of shaded/sunlit components). Data processing will be on best effort.

Figure 9: HyScreen set-up at the border between the MinnGold and wild-type (Eiko) field.

The technical characteristics of the HyScreen instrument are currently still under evaluation but can be summarized as follows:

- Spectral radiometric performance:

	Module 1 **400-1600 nm**	**Module 2** **670-780 nm**
FWHM	2-4	0.2-0.4
SNR	500-1000	200-300
Out-of-band rejection	< 0.5-1%	< 0.10.5 %

- Spatial performance:

Measuring distance	2 m
Target measurement area	0.5 m x 0.5 m
Field-of-view	35°
Spatial pixel resolution	Module 1 [400-1600nm]: 0.5 mm Module 2 [670-780nm]: 1 mm

Table 6: HyScreen data collected. All data were collected between 10:00 am and 12:00am in a small plot which contain both MinnGold and Eiko varieties.

Date	Number good scans	Data type
July 23nd	3	TOC - Minngold and Eiko
July 26rd	3	TOC - Minngold and Eiko
July 29rd	5	PRI experiment
July 29rd	8	SRN characterization
July 29rd	4	Reference panels

Figure 10: (Left) MinnGold and Eiko varieties and (right) and non-fluorescence targets (grey reference and soil).

The instrument was used in the field in a test experiment, data were not part of the objectives and will not be delivered to ESA. HyScreen processing chain, from raw data to Sun Induced fluorescence using the Spectral Fitting Methods (SFM), is almost completed. Only the implementation of the Point Spectral Function (PSF) is missing. The first results from fluorescence (grass) and non-fluorescence targets (soil) measured in Udine point in the right direction showing the technical functionality of the system. However fluorescence retrieval still needs to be refined.

4.2.2 Top-of-canopy reflectance and fluorescence measurements

4.2.2.1 Manual Spectroscopy System (MSS) for top-of-canopy measurements

Top-of-canopy high resolution radiance spectra were collected from July 21 to July 26 with the Manual Spectroscopy System (MSS; Figure 11), equipped with two spectrometers covering different spectral ranges:

i) a HR4000 spectrometer (OceanOptics, USA) operating in the visible and near infrared (400-1000 nm) spectral range with a full width at half maximum (FWHM) of 1 nm to allow the computation of incident irradiance, visible to near-infrared reflectance and different vegetation indices;

ii) a QEPro spectrometer (OceanOptics, USA) covering the 650-800 nm spectral range with a finer resolution (FWHM = 0.3 nm). This spectrometer is specifically intended for sun-induced fluorescence retrieval.

Bare fiber optics with a field of view (FOV) of 25° were used to alternatively measure a Spectralon white reference calibrated panel (Labsphere Inc., U.S.A.) mounted on a levelled tripod, and the vegetated targets. The soybean targets were measured from nadir at a height above the ground of 120 cm, corresponding to a sampling area of about 50 cm diameter.
Ocean Optics spectrometers were housed in a Peltier thermally regulated box (model NT-16, Magapor, Zaragoza, Spain) keeping the internal temperature at 25°C in order to reduce dark current drift.
The two spectrometers were spectrally calibrated with known standards (CAL-2000 mercury argon lamp, OceanOptics, USA) while the radiometric calibration was inferred from cross-calibration measurements performed with a reference calibrated FieldSpec spectrometer (Analytical Spectral Device, USA).
Fluorescence in the oxygen absorption bands O_2-B and O_2-A positioned at 687 (F_{687}) and 760 nm (F_{760}), respectively, as well as the full fluorescence spectrum, was retrieved using advanced spectral fitting methods (Cogliati *et al.*, 2015).

Figure 11: The Manual Spectroscopy System (MSS) measuring over the white panel within the soybean field.

In order to characterize the internal variability of each soybean field, three plots (M1, M2 and M3) were selected for each variety and measured with the MSS. Figure 13 shows the position of the measured plots, while corresponding GPS coordinates are reported in Table 7. Depending on weather conditions one or more of these plots were measured each day. A summary of the acquired data for each day is reported in Table 8.

4.2.2.2 FLOX System: Continuous hyperspectral instruments for top-of-canopy measurements

The FLuorescence bOX (FLOX; Figure 12) is an automated field spectroscopy device capable of collecting unattended, continuous, long-term hyperspectral measurements. It represents the evolution of prototypes such as Multiplexer Radiometer Irradiometer (MRI), SFLUOR box and SIF-System developed from a collaboration between Jülich Research Center and the Remote Sensing of Environmental Dynamics

Laboratory of the University of Milano Bicocca. The basic routines of FLOX are based on SPECY (Forschungszentrum Jülich, IBG-2: Plant Sciences).
FLOX is specifically designed to passively measure sun-induced Chlorophyll fluorescence under natural light conditions. Therefore the design is optimized in order to achieve maximum efficiency in terms of: Signal to Noise Ratio, Spectral Resolution and quick acquisition time. The core of the system is a QEPro spectrometer from Ocean Optics covering the Red/Near Infrared region (650 – 800 nm), analogous to the one used in the MSS (see paragraph 4.2.2.1). Upward and downward channels of FLOX allow to sequentially measure the solar irradiance and the reflected radiance from the canopy. In order to keep a stable level of dark current the spectrometers are embedded in a temperature controlled, waterproof housing. The signal-to-noise ratio is maximized thanks to accurate automatic optimization of the signal of both channels (http://jb-hyperspectral.com/wordpress/index.php/product/).
A single plot of each soybean variety was measured from July 23 to July 29. The position of the FLOX in the field, the correspondent GPS coordinates and a summary of the acquisition timeline are reported in Figure 13, Table 7 and Table 8, respectively.

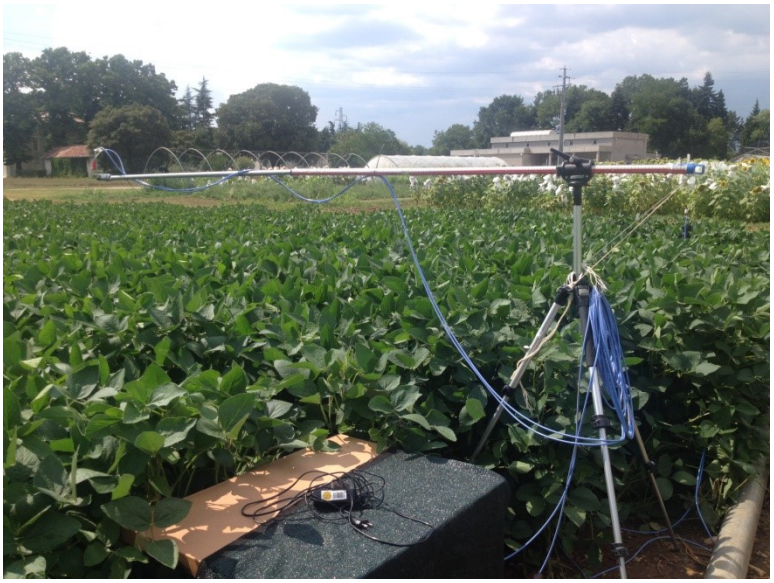

Figure 12: The FLuorescence bOX (FLOX) measuring the "Wild" soybean plot.

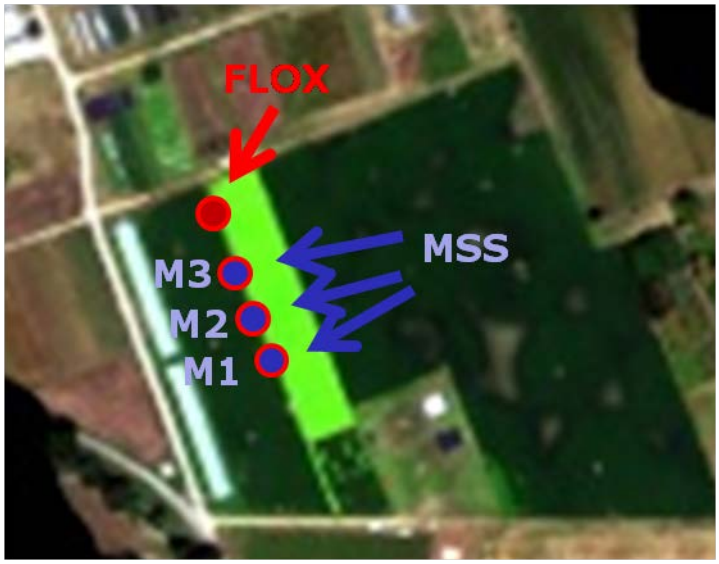

Figure 13: FLOX and MSS plots over a *HyPlant* RGB image.

Table 7: GPS coordinates of the plots measured with the MSS and the FLOX.

PLOT	Latitude (°)	Longitude (°)
M1	46.03574 N	13.22574 E
M2	46.03585 N	13.22568 E
M3	46.03595 N	13.22563 E
FLOX	46.03619 N	13.22546 E

Table 8: Schematic summary of the measurements taken over the soybean with the MSS and the FLOX.

PLOT	July 21	July 22	July 23	July 24	July 25	July 26	July 27	July 28	July 29
M1	X		X		X	X			
M2		X	X			X			
M3		X	X			X			
FLOX			X		X	X	X		X

4.2.3 Hyperspectral cal/val reference measurements

During the campaigns a mobile team equipped with a calibrated FieldSpec FR Pro field spectrometer (Analytical Spectral Device, USA) covering the visible, near infrared and shortwave infrared region (350 – 2500 nm) will measure various surface calibration/validation targets. Natural “pseudo-invariant” features at the site and artificial targets specifically placed into the flight lines will be used as calibration/validation targets. Pseudo–invariant surfaces will be for example asphalt, concrete, gravel or soil.
Artificial targets (black, white and grey) will be also placed into the flight lines.
Target reflectance will be measured by recording (i) incoming radiation using a white reference calibrated panel (Labsphere Inc., U.S.A.) and (ii) upwelling radiation from the surface.

4.2.3.1 German campaign

Spectral measurements for Cal/Val activities were acquired in correspondence of natural pseudo-invariant surfaces and vegetation with a ASD FieldSpec Pro spectrometer (Analytical Spectral Device Inc., USA), covering the visible, near-infrared and shortwave infrared spectral regions (350-2500 nm).
The measurements were collected on 19 July 2016 simultaneously to *HyPlant* overpass (14:06-15:09 local time). The location of the selected targets is described in Figure 14. A description of each target is given in Table 9.

Figure 14: Location of the ground targets at Camps Klein-Altendorf.

Table 9: Description of the ground targets at Campus Kleinaltendorf.

Target	Picture	Coordinates	Acquisition Day	Acquisition Time (local time)	Notes
Asphalt 1		50.61440 N, 6.99256 E	19 July 2016	14:06-14:11	Bright, dusty
Asphalt 2		50.61490 N, 6.99223 E	19 July 2016	14:38-14:43	Dark, dusty
Asphalt 3		50.61419 N, 6.99303 E	19 July 2016	14:54-14:58	Bright, clean

Soil	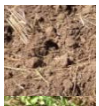	50.61501 N, 6.99165 E	19 July 2016	14:31-14:35	Bare soil with presence of straws
Grass	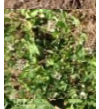	50.61489 N, 6.99184 E	19 July 2016	14:45-14:50	Heterogeneous, presence of flowers/soil
Sugarbeet 1		50.61432 N, 6.99225 E	19 July 2016	14:13-14:18	Low, sparse canopy
Sugarbeet 2	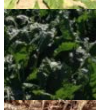	50.61420 N, 6.99206 E	19 July 2016	14:20-14:26	High, dense canopy
Wheat	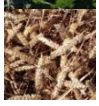	50.61398 N, 6.99291 E	19 July 2016	15:04-15:09	Completely dry

For each target, the measurements were acquired in correspondence of 4 points (10 spectra per point) in order to characterise the heterogeneity of the surface. The spectra were acquired in radiance. Reflectance was calculated in post-processing by dividing the upwelling radiance for the incoming radiation (average of 10 white reference spectra acquired before and of 10 white reference spectra acquired after the 40 measurements over the target) measured using a Spectralon white reference calibrated panel (Labsphere Inc., U.S.A.) mounted on a levelled tripod.
Examples of the spectral measurements acquired are showed in Figure 15.

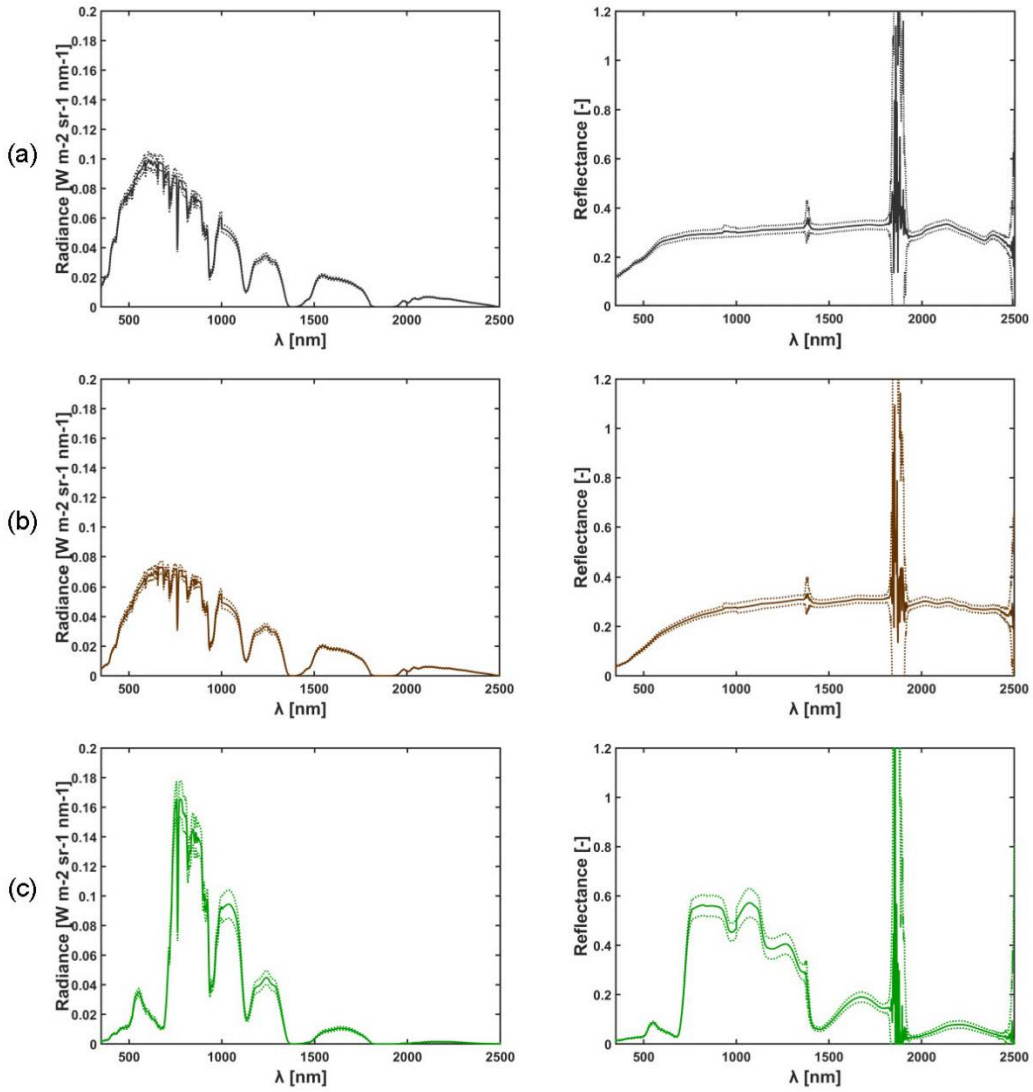

Figure 15: Examples of radiance (on the left) and reflectance (on the right) spectra of asphalt (a), soil (b) and sugar beet (c) measured in the field.

4.2.3.2 Italy SoyFLEX2 campaign

Spectral measurements for Cal/Val activities were acquired pseudo-invariant tarps in black white, grey and vegetation with a ASD FieldSpec Pro spectrometer (Analytical Spectral Device Inc., USA), covering the visible, near-infrared and shortwave infrared spectral regions (350-2500 nm).
The pseudo-invariant tarps were located close to the Soybean measurement field so they were visible in every recorded *HyPlant* flight line (Figure 16). The white tarp was placed on bare soil field to avoid adjacency effect from surrounding vegetation. Grey and Black trap were placed on the grassland field. To keep the influence of the surrounding vegetation as minimum as possible a layer of black foil was put underneath the tarps and a layer of plastic foil was used to frame the tarps. The position of the tarps was similar for each measurement days. The exact coordinates of the tarp position, acquisition date and time is given in Table 10 and Table 11. The example spectra of the reference targets are given in Figure 17.

Figure 16: Grey reference tarp framed by black foil to minimize adjacency effect from surrounding vegetation (left). RGB composite of a *HyPlant* flight line from 22 July 2016. Pseudo-invariant traps and vegetation plot for Cal/Val ASD measurements were placed close to the MinnGold measurement field (right).

Table 10: Geographic coordinates and acquisition and time of the Cal/Val reference targets on 22 July and 25 July 2016.

Target	Coordinates	Acquisition Day	Acquisition Time (local time)
grey tarp	46.03532 N, 13.22681 E; 46.03537 N, 13.22690 E 46.03529 N, 13.22695 E; 46.03525 N, 13.22684 E	22.July 25 July	12:38-12:43 12:34-12:38
black tarp	46.03516 N, 13.22690 E; 46.03519 N, 13.22700 E 46.03512 N, 13.22705 E; 46.03510 N, 13.22694 E	22.July 25 July	12:45-12:50 12:29-12:31
vegetation plot (grassland)	46.03494 N, 13.22709 E	22.July 25 July	13:17-13:23 12:24-12:27
white tarp	46.03464 N, 13.22700 E; 46.03463 N, 13.22708 E 46.03458 N, 13.22707 E; 46.03459 N, 13.22699 E	22.July 25 July	12:57-13:03 12:19-12:23
soil plot	46.03450 N, 13.22702 E	22.July 25 July	13:06-13:18 12:15-12:18

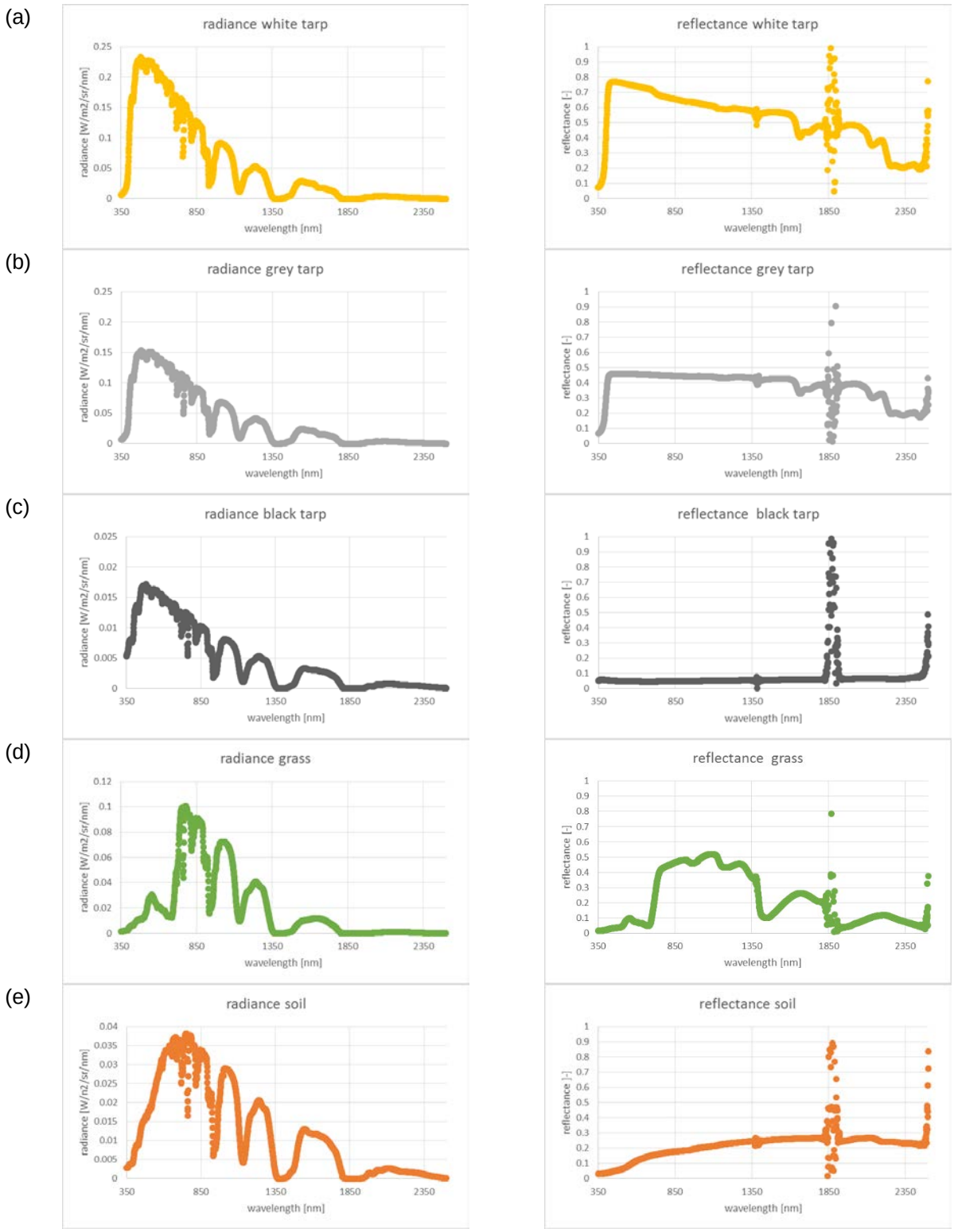

Figure 17: Examples of radiance (on the left) and reflectance (on the right) spectra of the white tarp (a), the grey tarp (b), black tarp (c), grassland (d) and soil (e) measured in the field.

Table 11: Geographic coordinates and acquisition and time of the Cal/Val reference targets on 26 July 2016.

Target	Coordinates	Acquisition Day	Acquisition Time (local time)
grey tarp	46.03503 N, 13.22659 E; 46.03506 N, 13.22668 E 46.03499 N, 13.22673 E; 46.03495 N, 13.22663 E	26.July	12:15-12:18
black tarp	46.03513 N, 13.22644 E; 46.03519 N, 13.22657 E 46.03513 N, 13.22663 E; 46.03510 N, 13.22655 E	26.July	12:18-12:26
vegetation plot (grassland)	46.03494 N, 13.22708 E	26.July	12:10-12:13
white tarp	46.03440 N, 13.22699 E; 46.03465 N, 13.22706 E 46.03460 N, 13.22705 E; 46.03461 N, 13.22698 E	26.July	12:06-12:09
soil plot	46.03455 N, 13.22701 E	26.July	12:04-12:06

4.2.4 Leaf level reflectance and fluorescence measurements

The optical properties and fluorescence of MinnGold and Eiko leaves were measured by means of a spectrometer (ASD FieldSpec 3 Hi-Res, Analytical Spectral Devices, Colorado, USA), coupled with a FluoWat leaf clip. This portable leaf clip allowed to measure real leaf reflectance, transmittance (without fluorescence contribution) and fluorescence emission under both artificial (active measurements) and natural light conditions (passive measurements). The fluorescence signal measuring principle is based on cutting off the incoming light spectrum above 650 nm with a short-pass filter, which allows recording only the fluorescence emission (650-850 nm), since in this way the measured signal does not originate from reflection (Van Wittenberghe *et al.*, 2013). Upward and downward steady-state fluorescence ($F\uparrow$, $F\downarrow$; when the adaxial leaf side was illuminated) were measured by placing the fibre optic into the upper or lower leaf clip opening, respectively. As fluorescence emission is highly dependent on the intensity of incoming photosynthetically active radiation – PAR_{leaf} (400-700 nm, Wm^{-2}) (Meroni *et al.*, 2009), the F signal was normalized for the absorbed PAR_{leaf} ($APAR_{leaf}=PAR_{leaf}*FAPAR_{leaf}$; $F_{yield}=F/APAR_{leaf}$) during the data processing phase. Incoming PAR_{leaf} was measured as the reflected radiance of a white reference panel (ODM-98, Gigahertz-Optik GmbH, Türkenfeld, Germany), with and without filter, while leaf reflectance and transmittance integrated over the PAR region were used to derive light absorbance and hence fraction of absorbed radiation ($FAPAR_{leaf}$). During the SoyFLEX2 campaign, active measurements were carried out by means of two types of artificial LED light sources characterized by different emission spectra (LED1 – producing white light (Figure 18) and LED2 – producing solely blue peak. In order to characterize the vertical profile of fluorescence in MinnGold and Eiko canopies, active measurements were performed on leaves located at three different canopy heights corresponding to the bottom, middle and top-of-canopy canopy layer, respectively, while passive fluorescence measurements were conducted on fully developed, sun exposed top-of-canopy leaves (Figure 18). The $FAPAR_{leaf}$ was measured on leaves sampled at the three heights (bottom, middle and top canopy) under both LED and sunlight illumination conditions (the latter measurements were carried out on detached leaves). The list of the leaf-level measurements performed within the SoyFLEX2 campaign is presented in Table 12

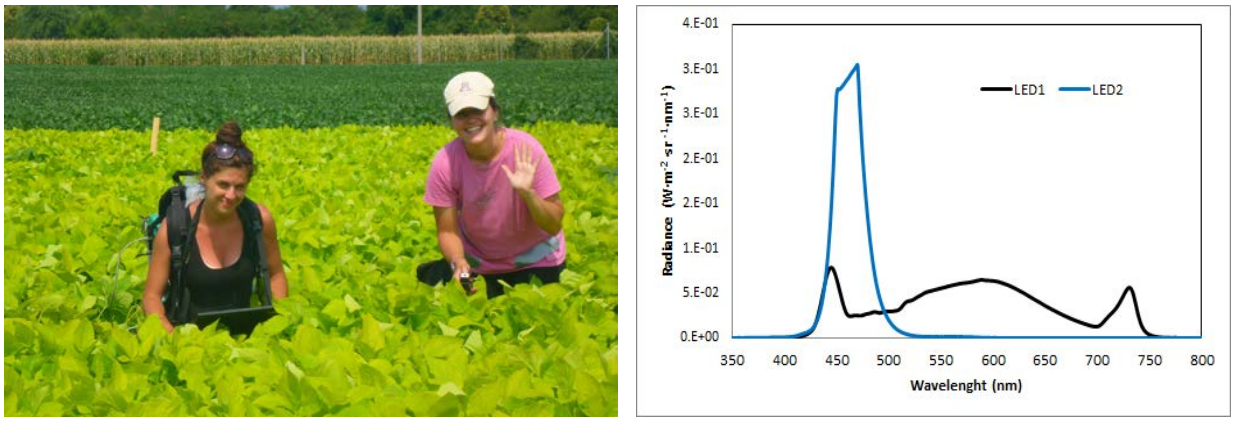

Figure 18: FluoWat measurements of top MinnGold leaves (left). Light spectra for the LED light sources used for determination of the vertical profile of leaf reflectance/transmittance/absorbance and fluorescence in the MinnGold and Eiko canopies (right).

Table 12: List of instruments and measurements carried out at the leaf level during the SoyFLEX2 field campaign.

Instrument	**Measurement scale and type**	**Date of measurements**	**Total nr of sampled leaves**	**Measured or derived parameter**
Sunlight	Leaf (top of the canopy)	2016-07-22 2016-07-26	4 9	Ftot, Fmax680, Fmax760 PAR $_{leaf}$, FAPAR $_{leaf}$, APAR $_{leaf}$ Ftot_yield (Ftot/APAR $_{leaf}$) Fmax680_yield (Fmax680/APAR $_{leaf}$) Fmax760_yield (Fmax760/APAR $_{leaf}$)
White LED	Leaf (bottom-middle-top of the canopy)	2016-07-25	9 for each canopy layer	
Blue LED	Leaf (bottom-middle-top of the canopy)	2016-07-27 2016-07-28	10 for each canopy layer	
Sunlight	Leaf (bottom-middle-top of the canopy)	2016-07-29	6 for each canopy layer	Leaf reflectance, transmittance, absorbance ($FAPAR_{leaf}$)

SYMBOLS and ABBREVIATIONS:

Ftot - the total fluorescence (integrated fluorescence signal between 650 and 800 nm) ($mWm^{-2}sr^{-1}nm^{-1}$)
Fmax680 - maximum fluorescence at O_2-A band ($mWm^{-2}sr^{-1}nm^{-1}$)
Fmax760 - maximum fluorescence at O_2-B band ($mWm^{-2}sr^{-1}nm^{-1}$)

4.2.5 Chlorophyll content

Circular discs of a diameter of 1 cm were punched from leaves located at three different heights (bottom, middle and top) of Eiko and Minngold canopies (12 leaves per layer and accession), frozen in liquid nitrogen and later transferred into a -80 °C freezer for long-term storage. This gives the possibility to analze Carotenoid (neoxanthin, violaxanthin, antheraxanthin, zeaxanthin, lutein, and beta-carotene concentrations) and chlorophyll pigment quantities within weeks and month after the campaign, if analyses becomes necessary according to a standardized protocol which is described in the following in short.
The extraction of chlorophyll a, chlorophyll b and the carotenoids is carried out using 100% acetone buffered with magnesium hydroxide carbonate (~4MgCO3 · Mg (OH) 2 · 5H2O), hereinafter referred to as acetone. 1000 ml of acetone are mixed with 20 g of magnesium hydroxide carbonate and the mixture is cooled to 4 ° C. until use. For extraction, the punched and frozen leaf discs are transferred into a new 2 ml Eppi (Safe Lock) and 200 µl of acetone are added. The sample is filled to 1-5 ml. The Eppi is stored on ice until they can be centrifuged at 13000 rpm for 5 minutes at 4 ° C. The excess solution is measured in the photometer. The spectrophotometric measurements are carried out in a glass cuvette at wavelengths of 470 nm, 645 nm, 662 nm and 710 nm.

4.2.6 Structural characterization of the canopy

Fraction of photosynthetically active radiation absorbed by the vegetation canopy ($FAPAR_{canopy}$) was measured by means of the SunScan probe (Delta-T Devices Ltd., Cambridge, UK), which is a 1-m long linear quantum sensor containing 64 photosynthetically active radiation (PAR; 400-700 nm) sensors equally spaced along its length. $FAPAR_{canopy}$ (-) was calculated using the following equation:

$$FAPAR_{canopy} = \frac{PAR_C - T_C - R_{CS} + R_S}{PAR_C} = \frac{APAR}{PAR_C} \qquad (14)$$

PAR_C - the downward PAR flux density incident at the top of the vegetation canopy (µmol m^{-2} s^{-1});
T_C - the downward PAR flux density transmitted through the vegetation canopy (µmol m^{-2} s^{-1});
R_C - the upward PAR flux density reflected from soil and canopy (µmol m^{-2} s^{-1});
R_S - the upward PAR flux density reflected from soil (µmol m^{-2} s^{-1});
APAR - the absorbed PAR (µmol m^{-2} s^{-1}).

Three different measurement protocols were performed to investigate (i) the spatial variability of the two soybean fields, (ii) detect the diurnal course of FAPAR of soybean, and (iii) record profiles of transmitted PAR throughout the canopy.
The $FAPAR_{canopy}$ measurements were performed around the time of the *HyPlant* overpasses (± 30 min) under clear sky conditions (on the 22nd and 23d of July 2016) in six randomly chosen plots located within the Minngold and Eiko fields (measurements in each of the 6 plots consisted of 4 replicates: 2 with sensor centered on the rows, and 2 with sensor placed in between the rows, thus the total number of measurements for each accession was equal to 24) with the Sunscan probe oriented parallel to the plant row direction (plants were planted in north-south oriented rows). Before and after each measurement, the values of PAR_C were recorded (in order to evaluate the stability of the incident radiation), and then averaged. R_S measurements were performed outside the canopy as shown in Figure 19.
The APAR for both soybean accessions at the time of the *HyPlant* overpass was calculated by multiplying average $FAPAR_{canopy}$ measured in the both fields by PAR measured at the onsite meteorological station.
Additionally, to assess the diurnal variability of $FAPAR_{canopy}$ (and APAR), on the 23d of July, the along-row $FAPAR_{canopy}$ measurements were performed at various times of the day in the footprint of the ground-truth FLOX system (see also chapter 4.2.2.2).

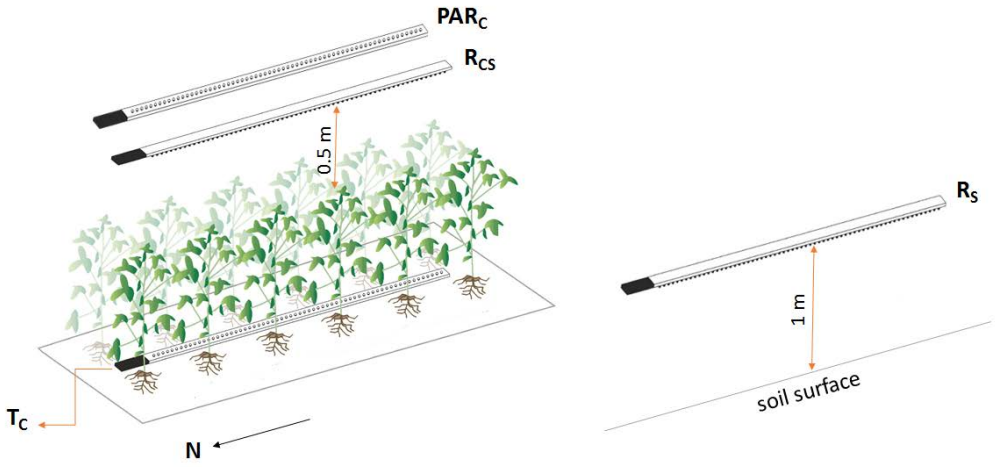

Figure 19: Sensor configuration for FAPARcanopy measurements in one of the Eiko plots. In this example, the sensor is placed in between the soybean rows. The sensor was facing upward when measuring PARC and TC; and downward when measuring RS and RCS.

Besides the $FAPAR_{canopy}$ measurements, the Sunscan probe was used to determine the vertical PAR transmittance profiles in the Minngold and Eiko canopies by measuring PAR transmitted at different canopy heights (at 15-cm canopy height intervals starting from the ground level; T_C, T_1, T_2, T_3, T_4 correspond to transmitted PAR measured at the ground level, and at the height of 15 cm, 30 cm, 45 cm and 60 cm, respectively; Figure 20) and normalizing it by the incident PAR measured at the top of the canopy - PAR_C. The transmittance profile measurements were made with the Sunscan probe oriented parallel to the plant row direction and centered on the row (n=4 for each canopy layer) in the selected Minngold and Eiko plots characterized by a similar canopy height of approximately 70 cm.

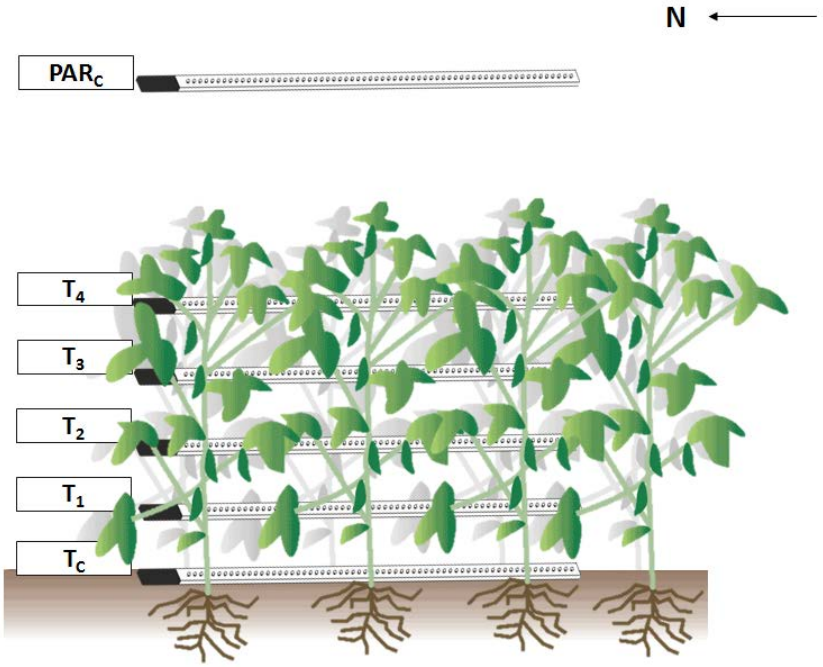

Figure 20: Vertical profile of photosynthetically active radiation (PAR) transmittance measurement scheme. During these along-row measurements of PAR transmittance at different canopy heights (TC, T1, T2, T3 and T4 corresponding to the ground level, and to the canopy height of 15 cm, 30 cm, 45 cm and 60 cm, respectively) the sensor was centred at the rows.

4.2.7 Gas exchange chambers

Chamber measurements of CO_2 fluxes were conducted in the period started from 21st of July and were continued till 27th of July 2016, on both Eiko and MinnGold varieties. The closed dynamic (non-steady-state flow-through) chamber system consisted of two chambers – transparent and non-transparent was used in order to estimate CO_2 fluxes: net ecosystem exchange (*NEE*) and ecosystem respiration (*Reco*), respectively (Figure 21). Additionally, heterotrophic respiration (*Rh*) was estimated on plots with a bare soil (plants were removed from plots end of June 2017) in order to calculate autotrophic respiration (*Ra*) of plants on plots were *Reco* was measured (*Ra*=*Reco* –*Rh*). Gross Primary Productivity (GPP), indicating the amount of CO_2 assimilated by plants in photosynthesis, was calculated as the difference between *Reco* and *NEE* taken consecutively with both chambers.

NEE fluxes measurements with transparent chamber

Reco fluxes measurements with non-transparent chamber

Heterotrophic respiration fluxes measurements with non-transparent chamber

Figure 21: Chambers used for net ecosystem exchange (*NEE*) and ecosystem respiration (*Reco*), and heterotrophic respiration (*Rh*) fluxes measurements.

4.2.7.1 Description of the chamber system

The closed dynamic (non-steady-state flow-through) chamber system was used in order to estimate CO_2 and H_2O fluxes from the experimental plots. The net ecosystem exchange (NEE) and the ecosystem respiration (Reco) were derived directly from measurements using a transparent and an opaque chamber, respectively (Figure 21). The same opaque chamber was used to measure heterotrophic respiration from plots with a bare soil. The transparent chamber was made from 3 mm thick Plexiglas® (Evonik Industries, Darmstadt, Germany), as this material has a high solar radiation transmittance (ca 90%; Chojnicki *et al.* 2010, Hoffman *et al.* 2015). The opaque chamber was made from 3 mm thick white PVC to ensure dark conditions. Both chambers had dimensions of 0.78x0.78x0.50 m and a total volume of 0.296 m^3. Due to the height of the Soybean canopy, which exceeded 0.7 meter at the beginning of the campaign, the chamber height was increased by adding one chamber extension (0.78x0.78x0.25m) made from transparent and non-transparent material, for NEE and Reco fluxes measurements, respectively. The chamber height was 0.75 meter and volume has increased to 0.47 m^3. This chamber setup was used on both varieties in the period between 21st and 23rd of July 2016. Starting from 24th of July, the chamber height and volume was increased farther (to 1.0 meter and 0.62m^3, respectively) by adding second extension. This chamber setup was used only on Eiko canopy (because the canopy height exceeded the height of the chamber), while 0.75 m height chamber was still used on MinnGold (the top of the canopy was below the top of the chamber). During installation of the chamber, the measuring team took special care about each single plant and chamber extensions and chambers were installed with a big care in order to not damage plants and destroy plant canopy next to the collars.

The chambers were fixed on square PVC collars (0.75 x 0.75m) installed in experimental fields with an insertion depth of 5 cm. Twelve soil frames were installed on 24th of June 2016 at the main experimental area, 6 frames per each variety at the locations indicated in Figure 22 with the exact coordinates of the frames given in Table 13. All frames were levelled at the day of installation. Four soil frames (2 locations x 2 soil frames) were installed on each of the varieties inside the soybean canopy (E1, E2, E4, E5 and M1, M2, M4, M5), while 2 frames (2 locations x 1 soil frame) were installed next to the previous one, but on plots without plants (E3, E6 and M3, M6). If plants occurred inside the installed collar, they were removed within one week after frames installation, just after a first rain, when soil starts to be wet and plants could be removed with roots.

Figure 22: Location of the chamber plots and weather station.

Table 13: Coordinates of the plots (E1-E6-gold plots).

Plot	lat	long	Plot	lat	long
E1	46.035590004175901	13.225809959694743	**M1**	46.035659993067384	13.225959995761514
E2	46.035590004175901	13.225780036300421	**M2**	46.035669967532158	13.225869974121451
E3	46.035620011389256	13.225790010765195	**M3**	46.035680025815964	13.225859999656677
E4	46.035269983112812	13.225999977439642	**M4**	46.035369979217649	13.226129980757833
E5	46.035269983112812	13.225959995761514	**M5**	46.03532999753952	13.226069966331124
E6	46.035299990326166	13.225980028510094	**M6**	46.0353500302881	13.22603995911777

During the measurement, the air inside the chamber was mixed using three computer fans (1.4 W each) installed in the chamber. Additionally, 2 fans were installed in each of the chamber extension and they were switched on just after chamber was installed on a collar. Air temperature was measured with radiation-shielded thermistor (T-107, Campbell Scientific, USA). In order to minimize changes of air temperature inside the chamber headspace, the passive cooling system was used as described in Chojnicki *et al.* 2010. The air was circulated at approximately 2.5 L min^{-1} between the chamber and a portable control box containing an infrared gas analyser (LI-840, LICOR, USA), which measured CO_2 and H_2O concentration in the air connected to a bypass flowing through the analyser at 0.7 L min^{-1}. Readings of gases concentration and air temperature were recorded every 5 seconds on a data logger (CR-1000, Campbell Sci., USA).

4.2.7.2 Protocol of measurements

The opaque chamber was closed for 150 seconds during measurements, while the closure time of transparent chamber varied from 120 seconds in the morning to 60 seconds at noon and afternoon in order

to avoid chamber overheating. In case of transparent chamber, the closure time was shortened if the within-chamber air temperature raised more than 1.5°C and the variability of the measured PAR was higher than 10% of the value recorded at the beginning of the measurement. In order to avoid overheating of the chamber and temperature probe in the period between measurements, the transparent chamber was covered with a white reflective material.
Each time, *NEE* measurements were taken at first. *Reco* measurements followed the *NEE* estimations and measurements were taken no more than one minute after *NEE* chamber was removed. After completing the *NEE* and *Reco* measurements on each of the subplots (e.g. E1, E2), the measurements were taken on plots with a bare soil in order to measure *Rh* (on E3, E6 and M3, M6 plots). These measurements were taken 12-15 minutes after first NEE measurements were taken.
Monitoring of meteorological variables
In order to monitor environmental conditions during chamber measurements and correlate the measured fluxes with PAR and temperature, meteorological measurements of soil temperature at 2 cm depth, canopy air temperature and relative humidity at 30 cm height (with HMP155, Vaisala, FI)and PAR (SKP215, Skye Instruments, UK) were carried out automatically at the climate station installed (on 20th of July) in the middle of the site (in a half of the way between E1-E3 & M1-M3 and E4-E6 & M4-M6). Additionally, soil temperature probes (T-107, Campbell Scientific, USA) were installed next to the frames at the depth of 2 cm in order to refer the respiration fluxes to soil temperature.

4.2.7.3 Data processing and fluxes calculation

In order to avoid errors related to changes in water vapour concentration in the chamber headspace over the closure time, the measured CO_2 concentrations were corrected for water dilution effect using equation:

$$C(t) = \frac{C(t)'}{1 - w/1000} \qquad (15)$$

where *C(t)* is the mole fraction of CO_2 (µmol·mol^{-1}) in dry air, *C(t)'* is the measured CO_2 mole fraction (µmol·mol^{-1}) in wet air and *w* is the measured mole fraction of water vapor (mmol·mol^{-1}) measured by LI-840 gas analyser (LI-COR Application Note 129, Perez-Priego *et al.* 2015). Afterwards, all data were visually inspected and data noise originating from disturbances caused by chamber deployment and possible saturation and canopy microclimate effects were discarded (according to Davidson *et al.* 2002, Hoffman *et al.* 2015).
CO_2 fluxes were calculated based on a gas concertation changes over the closure time using the linear regression type as described in Juszczak *et al*. 2013. Fluxes were calculated from the first 30 – 40 seconds of measurements for data with the highest regression slopes in order to avoid underestimation of the fluxes due to e.g. gas saturation, in accordance with Hoffmann *et al.* 2015. The gas flux (*F*) from the chambers in µmols m^{-2} per certain time unit (*t*) was calculated from the gas concentration change in the chamber headspace $\frac{\Delta C}{\Delta t}$, the chamber volume (*V*) and enclosed soil area (*A*) using the equation:

$$F = \frac{\Delta C}{\Delta t} \cdot \frac{V}{A \cdot M_v} \qquad (16)$$

where M_v(m^3·mol^{-1}) is the molar volume of air at the chamber air temperature and pressure. The determination coefficient was calculated for each time series and if $r^2 < 0.9$ the fluxes were discarded and not considered in the analyses.

4.2.8 Atmospheric conditions

4.2.8.1 German Campaign

The JOYCE AERONET station, which is located at the Research Centre Jülich (lat: 50.90833° N; long: 6.41250° E; Elevation: 108). Level 1.5 and level 2.0 data are available for both measurement days 19 and 20 July 2016 and are presented in Figure 23.

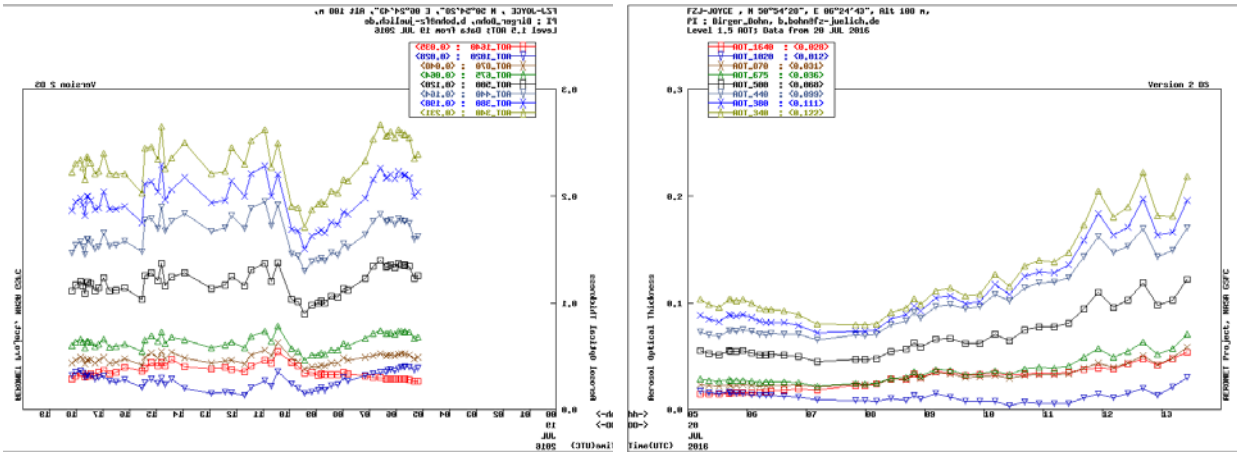

Figure 23: Sun Photometer measurements from the JOYCE AERONET station on 19 and 20 July 2016. The data presented are level1.5 data.

In parallel to the *HyPlant* overpasses at research campus Klein-Altendorf on 19 and 20 July 2016 Microtops measurements were recorded at lat: 50.617, long: 6.983. Non- averaged data points of Aerosol Optical Thickness at 500nm (AOT500), Water Vapour and the Angström coefficient calculated as the ration of the AOT at 400 nm and 1020 nm is presented in Figure 25.

Figure 24: Sun photometer MICROTOPS II.

During the airborne measurements atmospheric conditions were characterized using the sun photometer MICROTOPS II (Figure 24).
The Microtops was place close to the reference tarps on the ground at
lat: 46.035343°N, long: 13.227412°E.
Microtops recording were taken continuously during the *HyPlant* overpasses and if time availability of people permitted also in a 15 minutes interval throughout the day.

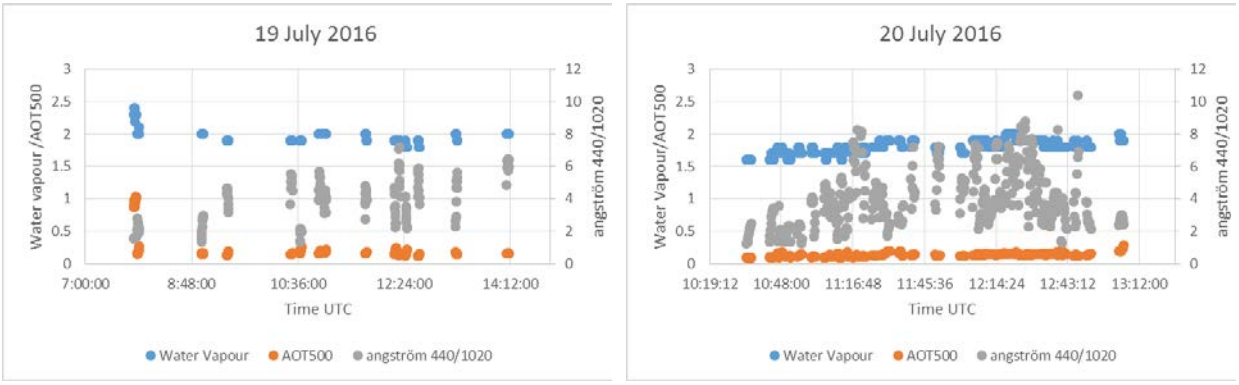

Figure 25: Sun photometer measurements from Microtops II at campus Klein-Altendorf on 19 and 20 July 2016 recorded during the *HyPlant* overpasses. A minimum of 10 scans are taken for each measurement. Data presented here are non-averaged.

4.2.8.2 SoyFLEX2 experiment Italy

Microtops II measurements were recorded in conjunction to the *HyPlant* overpasses over the Udine soybean field on 22 and 23 July 2016 and 25 - 27 July 2016. Ten Microtops reading were taken for each measurement and non-averaged data are shown in Figure 26

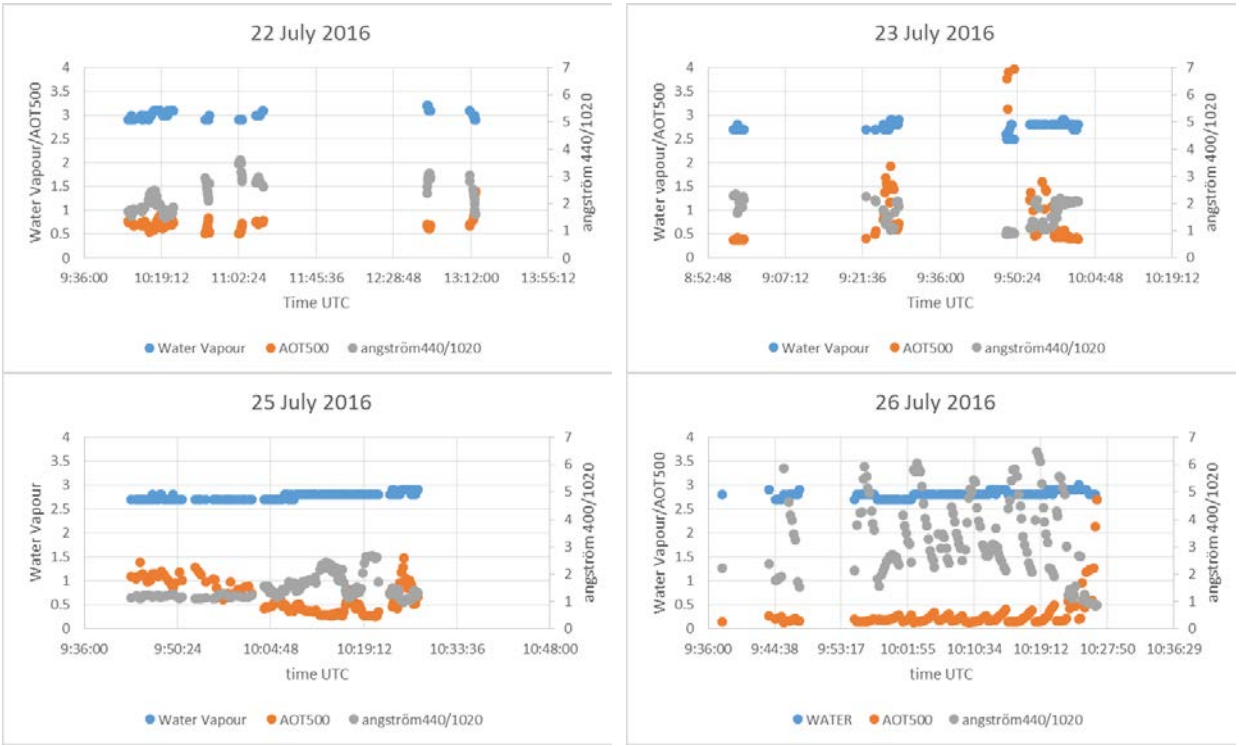

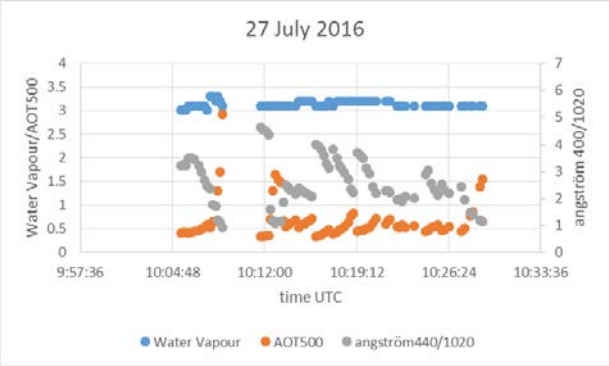

Figure 26: Sun photometer measurements from Microtops II at Udine on 22 and 23 July 2016 and 25 - 27 July 2016 recorded during the *HyPlant* overpasses. A minimum of 10 scans are taken for each measurement. Data presented here are non-averaged.

4.2.9 Meteorological conditions

For all measurement sites, standard meteorological parameters like air temperature, air pressure and relative humidity are available for the time period of the *HyPlant* overpasses (Figure 27). In addition global radiation and/or photosynthetic active radiation (PAR were measured as well). For all measurement sites at least 30 mean values are available, in most case 10 minutes means.

Figure 27: Example of a meteorological station at the research Campus Kleinaltendorf, placed in experimental field.

4.2.9.1 Czech Republic campaign

Meteorological data are continuously acquired at research station Bílý Kříž in Moravian-Silesian Beskids mountains. Several selected meteorological measurements describing atmospheric conditions during day of *HyPlant* overflight (7 June 2016) are plotted in Figure 28.

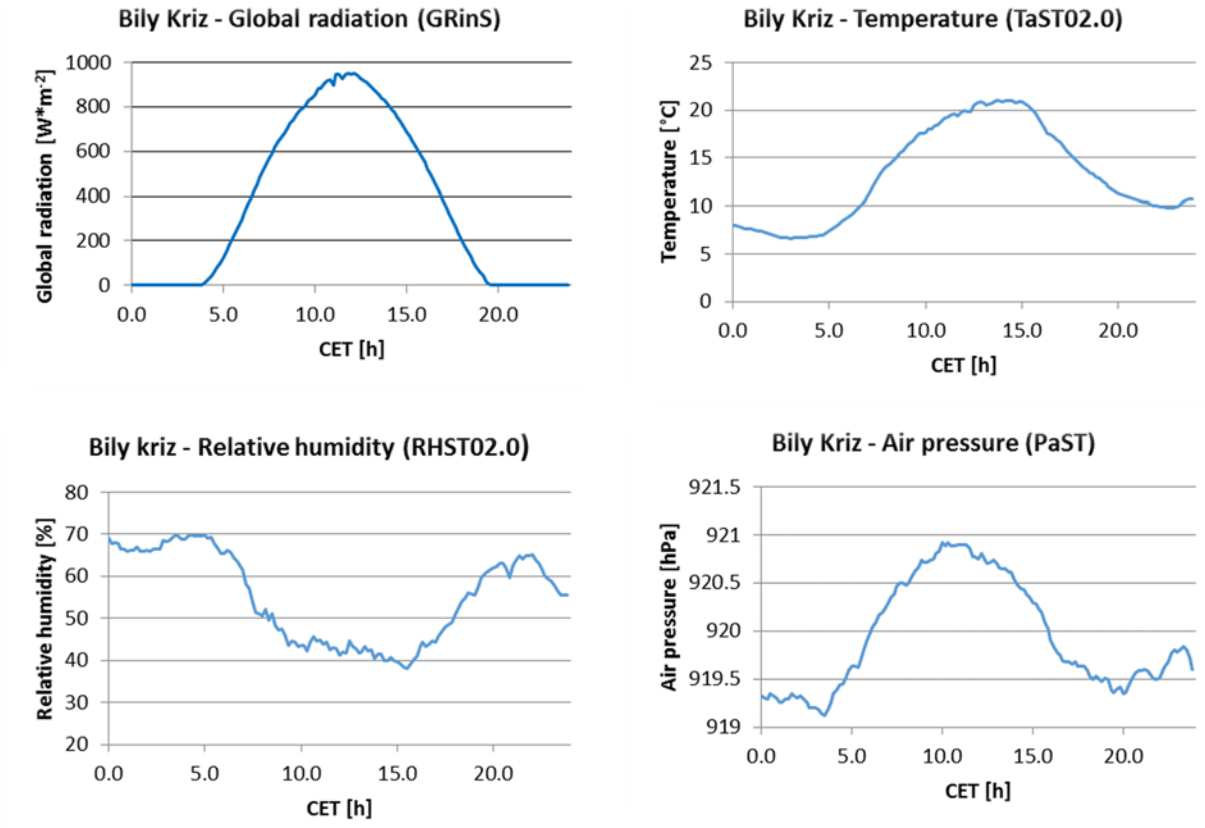

Figure 28: Global radiation, air temperature, relative humidity and air pressure of the meteorological station of Bílý Kříž recorded on 7 June 2016.

4.2.9.2 German campaign

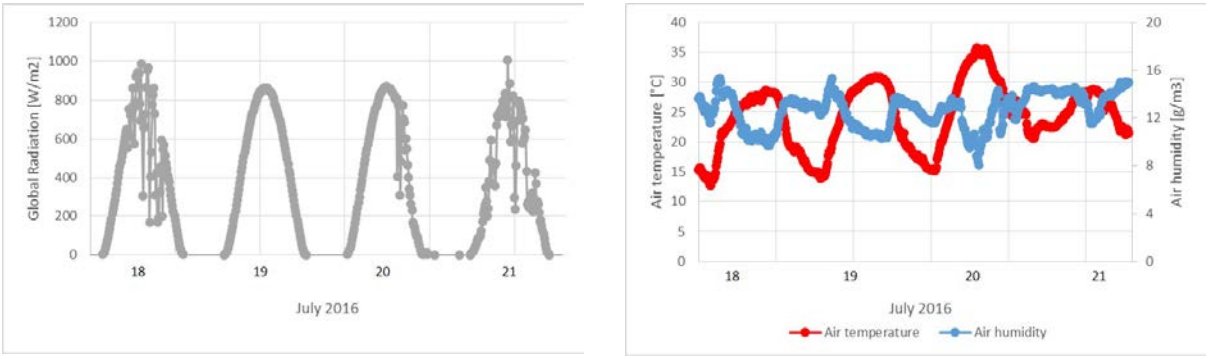

Figure 29: Global Radiation, air temperature and absolute humidity of the meteorological station in the experimental field of Selhausen in the TR32 study area. Data show the time period from 18 - 21 July 2016.

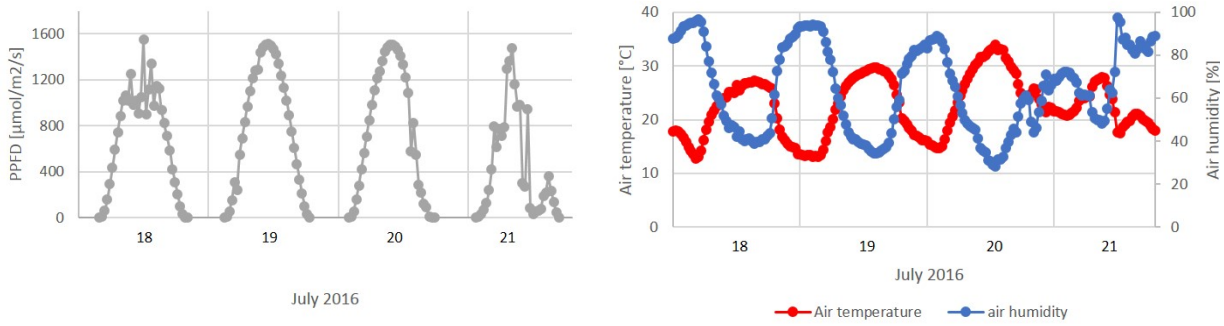

Figure 30: Photon Flux Density (PPFD), air temperature and relative humidity of the meteorological station in the experimental field of the research campus Klein-Altendorf. Data show the time period from 18 - 21 July 2016.

4.2.9.3 Italy Soyflex2 campaign

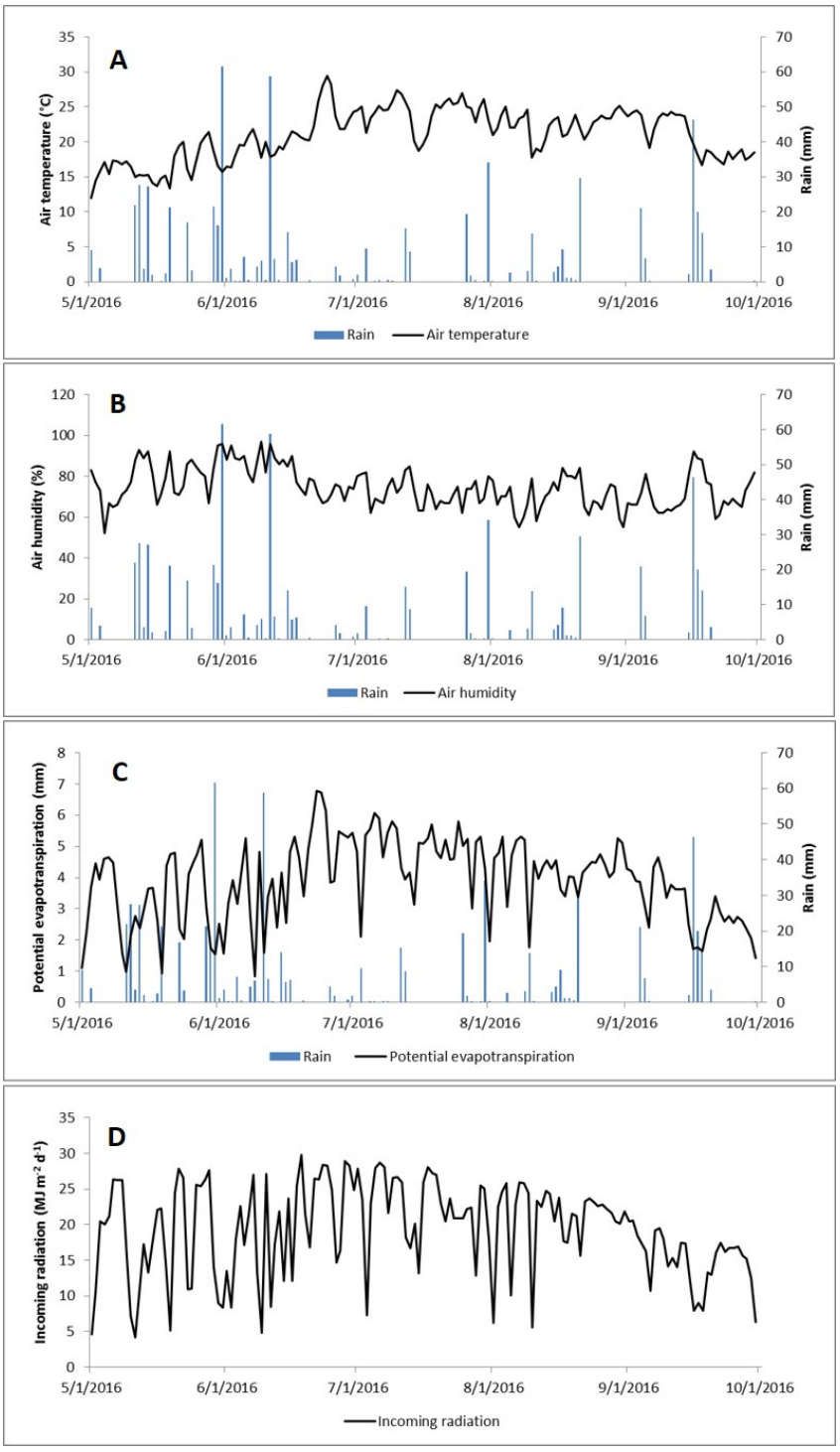

Figure 31: Air temperature in °C (A), air humidity in % (B), potential Evapotranspiration in mm (C), rain in mm (A-C) and incoming radiation in MJ m^{-2} d^{-1} (D) for the vegetation period of the soya field in Udine.

5 Campaign sites and activities

HyPlant data acquisition in 2016 was split in the campaign windows in the different countries, Czech Republic, Germany and Italy. Campaign windows were defined be aircraft availability, weather conditions and development stage of the vegetation.

Table 14: Overview of campaign windows and time of *HyPlant* data acquisition in 2016.

Country	Experimental sites	Date
Czech Republic	Bílý Kříž	18 May – 10 June 2016
Germany	TR32; Selhausen, CKA	18.07.16 – 20.07.16
Italy	Udine	22.07.16 – 27.07.16 for *HyPlant* 18.07.16 – 29.07.16 for ground measurements

5.1 Long term campaign site in Germany

The long term campaign sites in Germany consist of the anthropogenic, agricultural area around Jülich (chapter 5.1.1) and the agricultural research campus Klein-Altendorf (chapter 5.1.2).
An overview of all recorded flight lines and additional available ground data are given in Table 19.

5.1.1 Anthropogenic, agricultural area around Jülich

The agricultural area around Jülich (Figure 32) was chosen as a long term campaign sites and is associated the 'Transregional Collaborative Research Centre 32: Patterns in Soil-Vegetation-Atmosphere Systems: Monitoring, Modelling and Data Assimilation' (TR32; www.tr32.de). It can be described as an anthropogenically influenced area consisting of a variety of different vegetation types, including agricultural fields, grasslands, meadows, and small forest patches. The anthropogenic, agricultural area around Jülich, was recorded in two different flight patterns;

- a large map (TR32 map) which covers a 12 x 13 km area around Jülich with a 2.5 x 2.5 m pixel resolution (Figure 32; Table 15)
- the area close to Selhausen with a 1 x1 m pixel resolution (Figure 33, Table 16).

Both flight patterns were repeated annually since 2012 [RD-6] and are part of a continuous time series.

Figure 32: Large map of the anthropogenic, agricultural area around Jülich (TR32 map) consisting of 18 flight lines with a 25% overlap.

Table 15: Flight lines of the large map of the anthropogenic, agricultural area around Jülich (TR32 map) with a spatial resolution of 2.5 x 2.5 m per pixel.

Flight line	Start		End		Altitude
	Lat	Long	Lat	Long	[m]
fluomap_1 (TR32)	50.901088	6.290447	50.90109	6.290447	1635
fluomap_2 (TR32)	50.901088	6.301827	50.90109	6.301827	1635
fluomap_3 (TR32)	50.901088	6.313207	50.90109	6.313207	1635
fluomap_4 (TR32)	50.901088	6.324587	50.90109	6.324587	1635
fluomap_5 (TR32)	50.901088	6.335967	50.8884	6.335967	1635
fluomap_6 (TR32)	50.901088	6.347347	50.8884	6.347347	1635
fluomap_7 (TR32)	50.901088	6.358727	50.8884	6.358727	1635
fluomap_8 (TR32)	50.901088	6.370107	50.83375	6.370107	1635
fluomap_9 (TR32)	50.901088	6.381487	50.83375	6.381487	1635
fluomap_10 (TR32)	50.901088	6.392867	50.83375	6.392867	1635
fluomap_11 (TR32)	50.901088	6.404247	50.83375	6.404247	1635
fluomap_12 (TR32)	50.901088	6.415627	50.83375	6.415627	1635
fluomap_13 (TR32)	50.901088	6.427007	50.83375	6.427007	1635
fluomap_14 (TR32)	50.901088	6.438387	50.83375	6.438387	1635
fluomap_15 (TR32)	50.901088	6.449767	50.83375	6.449767	1635
fluomap_16 (TR32)	50.901088	6.461147	50.83375	6.461147	1635
fluomap_17 (TR32)	50.889027	6.472527	50.83375	6.472527	1635
fluomap_18 (TR32)	50.883353	6.483907	50.83375	6.483907	1635

Figure 33: Six flight lines to cover the Selhausen area, with a spatial resolution of 1 x1 m.

Table 16: Flight lines of the Selhausen agricultural area with a spatial resolution of 1 x 1 m per pixel

Flight	start		End		altitude
line	lat	long	Lat	long	[m]
SEL_1	50.856448	6.455248	50.896013	6.416788	680
SEL_2	50.857263	6.458175	50.897632	6.419320	680
SEL_3	50.899306	6.421787	50.857929	6.461255	680
SEL_4	50.900869	6.424378	50.858944	6.464518	680
SEL_5	50.902591	6.426794	50.860729	6.466753	680
SEL_6	50.893999	6.414679	50.855164	6.452372	680

5.1.2 Research campus Klein-Altendorf, Germany

The agricultural research Campus Klein-Altendorf near Bonn comprises 181 ha for field trials and approximately 4,800 m^2 for Greenhouse trials. On Campus Klein-Altendorf, research can be conducted with all kinds of plants and crops, ranging from small plants like *Arabidopsis* or herbs to large crops like maize, from annual crops like vegetables to perennial plants like *Miscanthus* or fruit trees. Plants can be grown in the experiments under practical conditions.
The whole agricultural research campus was covered with a 1 x 1 m resolution using the flight patter shown in Figure 34 and Figure 17. This flight pattern is repeated annually since 2012 [RD-4]. In addition, the SoyFLEX2 back up experiment was cover in 0.5 x 1 m resolution (Figure 34 and Table 18).

Figure 34: Four flight lines to cover the experimental Campus Klein-Altendorf with a pixel size of 1 x 1 m resolution and an overlap of 20% of the flight lines (red). The SoyFLEX experiment is located at Campus 'North' and two flight lines with a spatial resolution of 0.5 x 1 m (white).

Table 17: Flight lines of Campus Klein-Altendorf with a spatial resolution of 1 x 1 m per pixel.

Flight line	Start		End		Altitude [m]
	Lat	Long	Lat	Long	
CKA_L1	50.629950	6.981593	50.612125	7.007524	868m
CKA_L2	50.629449	6.977154	50.610518	7.004940	868m
CKA_L3	50.627800	6.974343	50.608936	7.002542	868m
CKA_L4	50.625198	6.973288	50.607192	7.000324	868m

Table 18: Flight lines of Campus Klein-Altendorf with a spatial resolution of 0.5 x 1 m per pixel, to cover the SoyFLEX2 backup experiment.

Flight line	Start		End		Altitude [m]
	Lat	Long	Lat	Long	
SOY_L5	50.629154	6.994687	50.618834	6.996542	512
SOY_L9	50.623147	7.002181	50.621917	6.986254	512

Table 19: Data acquired during the Germany campaign 2016.

Date	Start	End	No. flight lines	Area	*HyPlant* performance	TASI performance	Cloud coverage	Sun photometer	ASD Reference (Cal/Val)
July 18th	17:10	17:55	8	Boresight flight (BOR)	OK	NO	2/8	FZJ-JOYCE AERONET	NO
July 19th	10:56	11:23	6	Selhausen (SEL)	OK	OK	0/8	FZJ-JOYCE AERONET	NO
July 19th	11:49	13:43	18	TR32 large map (TR32)	OK	OK	0/8	FZJ-JOYCE AERONET	NO
July 19th	14:08	14:22	4	Kleinaltendorf (CKA)	OK	OK	0/8	Microtops (lat: 50.617 long: 6.983)	YES (lat: 50.614 long: 6.993)
July 19th	14:26	14:30	2	Kleinaltendorf (SOY)	OK	OK	0/8	Microtops (lat: 50.617 long: 6.983)	YES (lat: 50.614 long: 6.993)
July 20th	13:07	13:11	2	Kleinaltendorf (SOY)	OK	OK	0/8	Microtops (lat: 50.617 long: 6.983)	NO
July 20th	13:27	13:49	6	Selhausen (SEL)	OK	OK	0/8	FZJ-JOYCE AERONET	NO
July 20th	14:05	14:08	2	Kleinaltendorf (SOY)	OK	OK	0/8	Microtops (lat: 50.617 long: 6.983)	NO
July 20th	14:16	14:28	4	Kleinaltendorf (CKA)	OK	OK	0/8	Microtops (lat: 50.617 long: 6.983)	NO
July 20th	14:31	14:45	2	Kleinaltendorf (SOY)	OK	OK	0/8	Microtops (lat: 50.617 long: 6.983)	NO

5.2 Spruce forest experimental site in Bílý Kříž, Czech Republic

The spruce forest experimental research site of Bílý Kříž site is located in the Moravian-Silesian Beskydy Mountains in the eastern part of the Czech Republic and part of the CzechGlobe infrastructure (http://www.czechglobe.cz/en/) and serves as an experimental site for ecosystem monitoring, and many types of continuous/discrete measurements have been carried out there for more than 15 years. The forest site was covered with *HyPlant* in two spatial resolution of 1.0 m (Figure 35, Table 20) and 3.0 m (Figure 36, Table 21). Simultaneously with *HyPlant* data were acquired hyperspectral thermal data by means of sensor TASI600 with spatial resolution 0.8 m and 2.4 m. An overview of all recorded flight lines is given in Table 22.

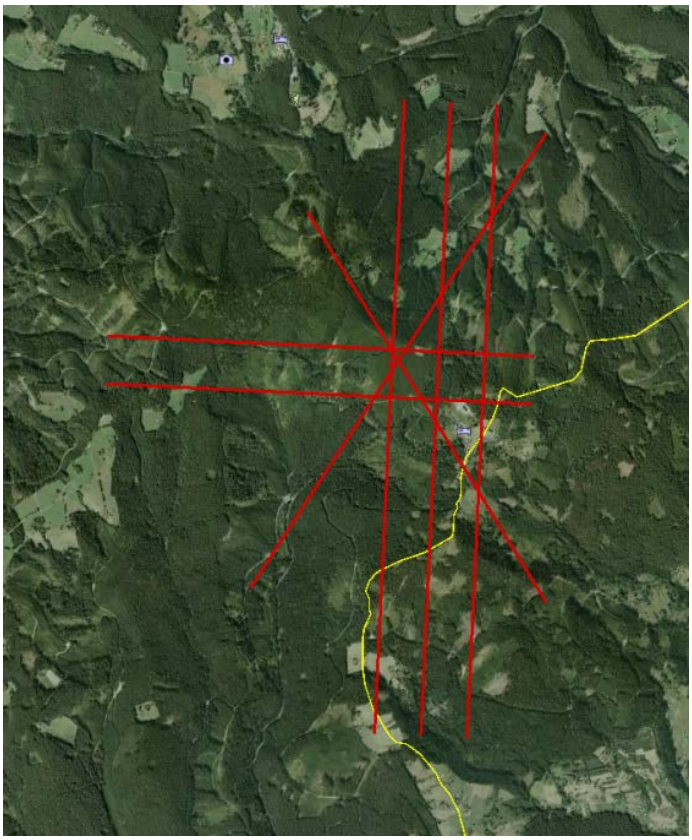

Figure 35: Set of flight lines for the Bílý Kříž site acquired with resolution 1.0 m.

Table 20: Flight lines of the Bílý Kříž area with a spatial resolution of 1 x1 m.

Flight	start		End		altitude
line	lat	long	Lat	long	[m]
BK_1	49.48335	18.54230	49.51389	18.54453	1620
BK_2	49.48346	18.53887	49.51399	18.54110	1620
BK_3	49.48356	18.53544	49.51410	18.53766	1620
BK_4	49.50273	18.51569	49.50175	18.54729	1620
BK_5	49.50042	18.51553	49.49945	18.54713	1620
BK_8	49.50870	18.53047	49.48992	18.54816	1620

BK_9	49.49061	18.52625	49.51249	18.54819	1620

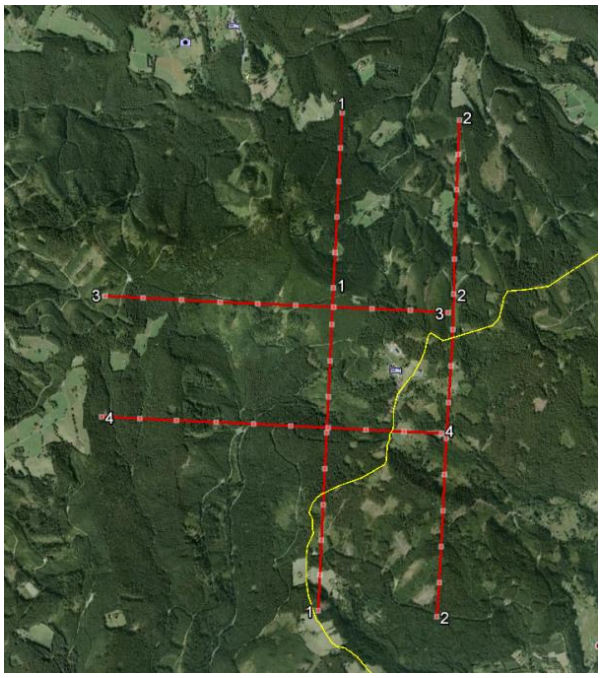

Figure 36: Set of flight lines for the Bílý Kříž site acquired with resolution 3.0 m.

Table 21: Flight lines of the Bílý Kříž area with a spatial resolution of 3 x 3 m.

Flight line	Start		End		Altitude
	Lat	Long	Lat	Long	[m]
BK_21	49.48367	18.53538	49.51419	18.53766	2800
BK_22	49.48332	18.54650	49.51384	18.54879	2800
BK_23	49.50280	18.51569	49.50180	18.54745	2800
BK_24	49.49554	18.51517	49.49454	18.54693	2800

Table 22: Data acquired during the Czech Republic campaign 2016.

Date	Start	End	No. flight lines	Area	*HyPlant* perfor-mance	TASI perfor-mance	Cloud cover-age	Sun Photo-meter	ASD Reference (Cal/Val)
May 23th	10:22	10:39	3	Bílý Kříž (BK)	NO	OK	0/8	NO	YES (lat: 49.499 long: 18.542)
June 7th	11:51	12:48	11	Bílý Kříž (BK)	OK	OK	0/8	NO	NO

Due to the instability of the FLUO sensor during this acquisition of Bílý Kříž could not be recorded on May 23rd, but needed to be repeated on July 7th, 2016. While atmospheric conditions were stable on both days,

no additional ground reference measurements such as Microtops or ASD Cal/Val measurements are available on June 7th.

5.3 SoyFLEX2 campaign site; Experimental farm Udine, Italy

Soybean plots were planted in Germany and Italy in the field. Four different varieties of the plants are planted on small plots (1.5 x 8 m) on different locations in Italy, for example Udine, Italy and at Campus Klein-Altendorf in Bonn, Germany (chapter 5.1.2, Figure 34). The main part of the ground and airborne measurements of the SoyFLEX2 experiment took place in Udine, Italy, were the chlorophyll deficiency mutant MinnGold and wild-type Eiko was also planted in large areas (Figure 37) The Soybean plants at the research campus Klein-Altendorf only served as a back-up possibility. The analyses of the SoyFLEX2 experiment will however focus on the data recorded in Udine, Italy.

Figure 37: Field design of the Soya at the experimental farm of the University in Udine, Italy. Red: small field plots (1.3 x 8 m each plot), Yellow: MinnGold field; Green; Eiko field and white: two flight lines to cover the experimental field in a 1 x 1 m resolution.

Table 23: Flight lines of the experimental farm of the University of Udine to cover the SoyFLEX2 experiment with a spatial resolution of 1 x 1 m per pixel.

Flight line	Start		End		Altitude
	Lat	Long	Lat	Long	[m]
UDI_1	46.023512	13.233422	46.040887	13.223875	765
UDI_2	46.031698	13.211510	46.037884	13.235276	765

Table 24: Data acquired during the Italy campaign 2016.

Date	Start	End	No. flight lines	Area	*HyPlant* performance	TASI performance	Sun photometer	ASD Reference (Cal/Val)
July 22nd	12:03	12:17	4	Udine (UDI)	OK	OK	Microtops lat:46.05 long:13.217	Lat: 46.03494 Long:13.22708
July 23rd	11:38	12:07	7	Udine (UDI)	OK	OK	Microtops lat:46.05 long:13.217	Lat: 46.03494 Long:13.22708
July 25th	12:03	12:21	5	Udine (UDI)	OK	OK	Microtops lat:46.05 long:13.217	Lat: 46.03494 Long:13.22708
July 26th	11:58	12:23	6	Udine (UDI)	OK	OK	Microtops lat:46.05 long:13.217	Lat: 46.03494 Long:13.22708
July 27th	12:04	12:28	7	Udine (UDI)	OK	OK	Microtops lat:46.05 long:13.217	Lat: 46.03494 Long:13.22708

5.3.1 Defined core dataset for SoyFLEX2 experiment

For the further analyses of the SoyFLEX2 experiment a core dataset of five flight lines was proposed and agreed on between the partners and the agency during the progress meeting. Those flight lines were recorded around 12 local time and no clouds showed over the experimental field (Table 25).

Table 25: Defined core dataset of the Udine flight lines. All flight lines are recorded around 12 local time and showed no could coverage during the overpass.

Date	Time (local)	Area	No. flight lines	Flight Direction	Contemporary sentinel overpass
July 22nd	12:03	Udine (UDI)	L2	W	
July 23rd	12:07	Udine (UDI)	L2	W	Sentinel-3 (09:59 UTC OLCI)
July 25th	12:08	Udine (UDI)	L2	W	Sentinel-2 (10:08 UTC) Sentinel-3 (09:07 UTC OLCI)
July 26th	12:03	Udine (UDI)	L2	W	
July 27th	12:17	Udine (UDI)	L2	W	

5.3.2 *HyPlant* quick looks of core dataset

The following figure (Figure 38 - Figure 42) show false colour already georectified quicklooks of each flight line of the defined core dataset. Data were recorded with the FLUO module of the *HyPlant* sensor.

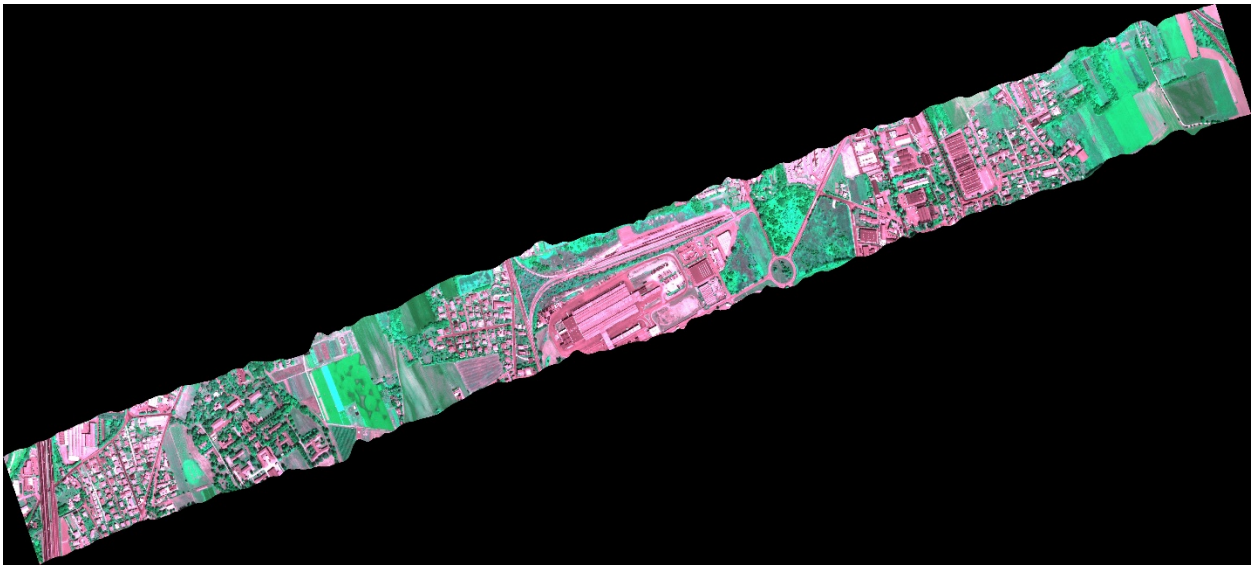

Figure 38: Quicklook of flight line 20160722-UDI-1203-0600-L2-W-FLUO

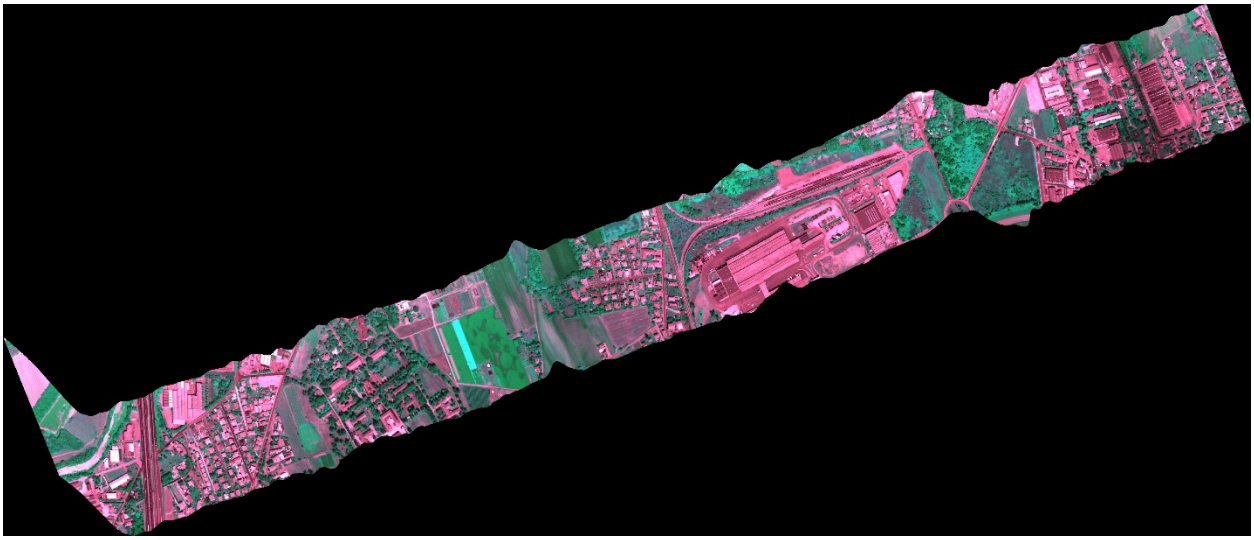

Figure 39: Quicklook of flight line 20160723-UDI-1207-0600-L2-W-FLUO

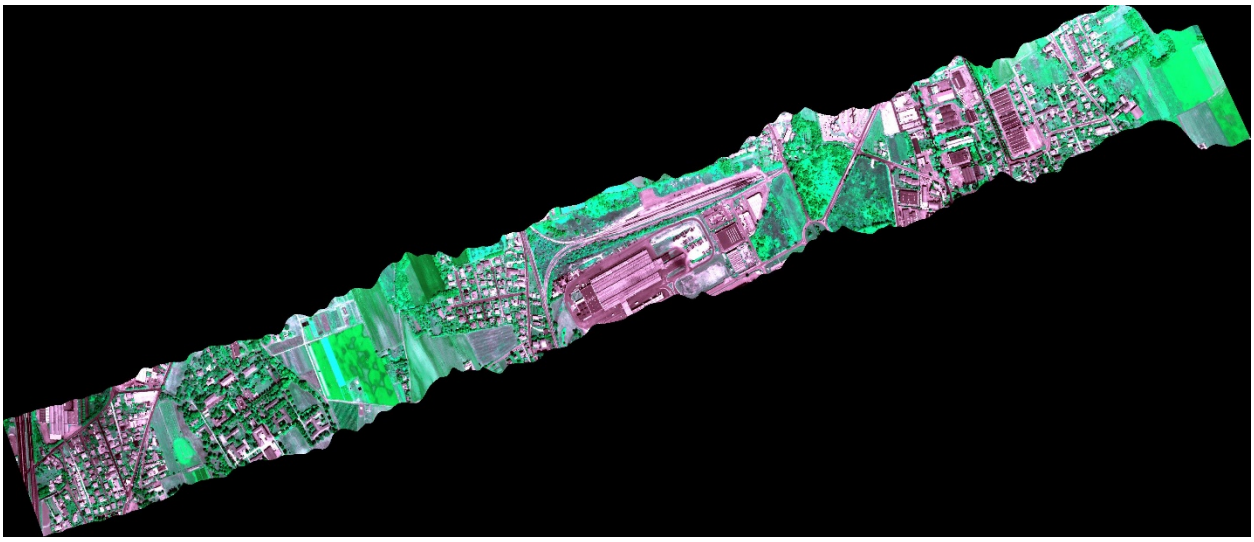

Figure 40: Quicklook of flight line 20160725-UDI-1208-0600-L2-W-FLUO

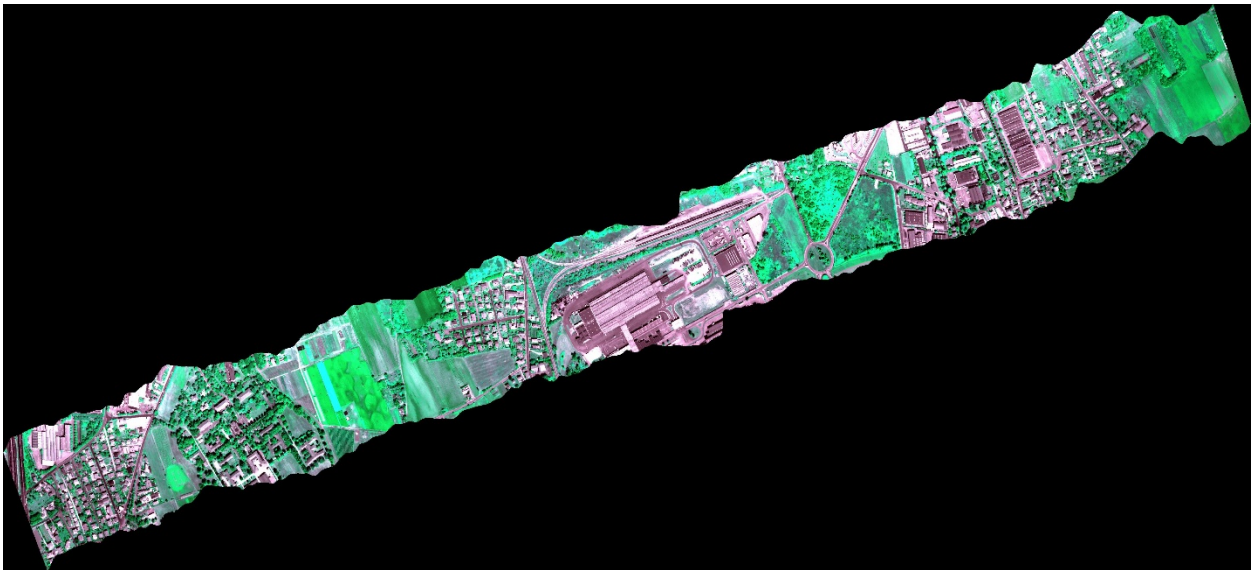

Figure 41: Quicklook of flight line 20160726-UDI-1203-0600-L2-W-FLUO

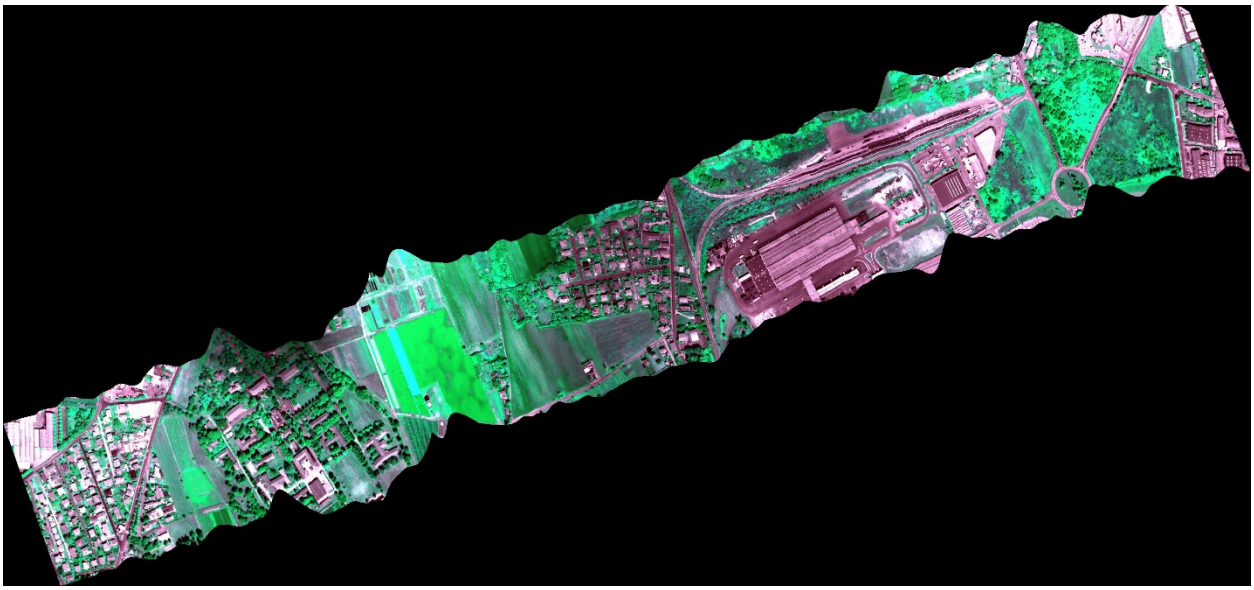

Figure 42: Quicklook of flight line 20160727-UDI-1217-0600-L2-W-FLUO

6 Results

6.1 Mapping of the long term study sites

In the following chapter we present true colour images (Figure 43), vegetation indices (Figure 44) and fluorescence maps of the anthropogenic, agricultural area around Jülich retrieved from the Spectral Fitting Method (Figure 49, Figure 51) and the iFLD method (Figure 52, Figure 53). For the first time both fluorescence retrieval method were applied to the large TR32 map, which consists of 18 single flight lines. Section 6.1.1.2 compares the results derived from both methods. True colour images, vegetation indices and fluorescence maps of the anthropogenic, agricultural area around Selhausen (Figure 56, Figure 57), the agricultural experimental campus in Klein-Altendorf (Figure 58, Figure 59) in Germany and the forest area of Bílý Kříž, Czech Republic (Figure 60, Figure 61). The fluorescence maps of the agricultural sites around Jülich were calculated using the iFLD method as a default, while fluorescence maps of the forest areas were retrieved with the SVD, due to missing non-vegetation reference surfaces.

6.1.1 Anthropogenic, agricultural area around Jülich

6.1.1.1 Vegetation indices of the TR32 map

Figure 43: True colour map (R: 157, G: 105, B: 52 of the anthropogenic, agricultural area around Jülich (TR32 map). Data were recorded on 19 July 2016.

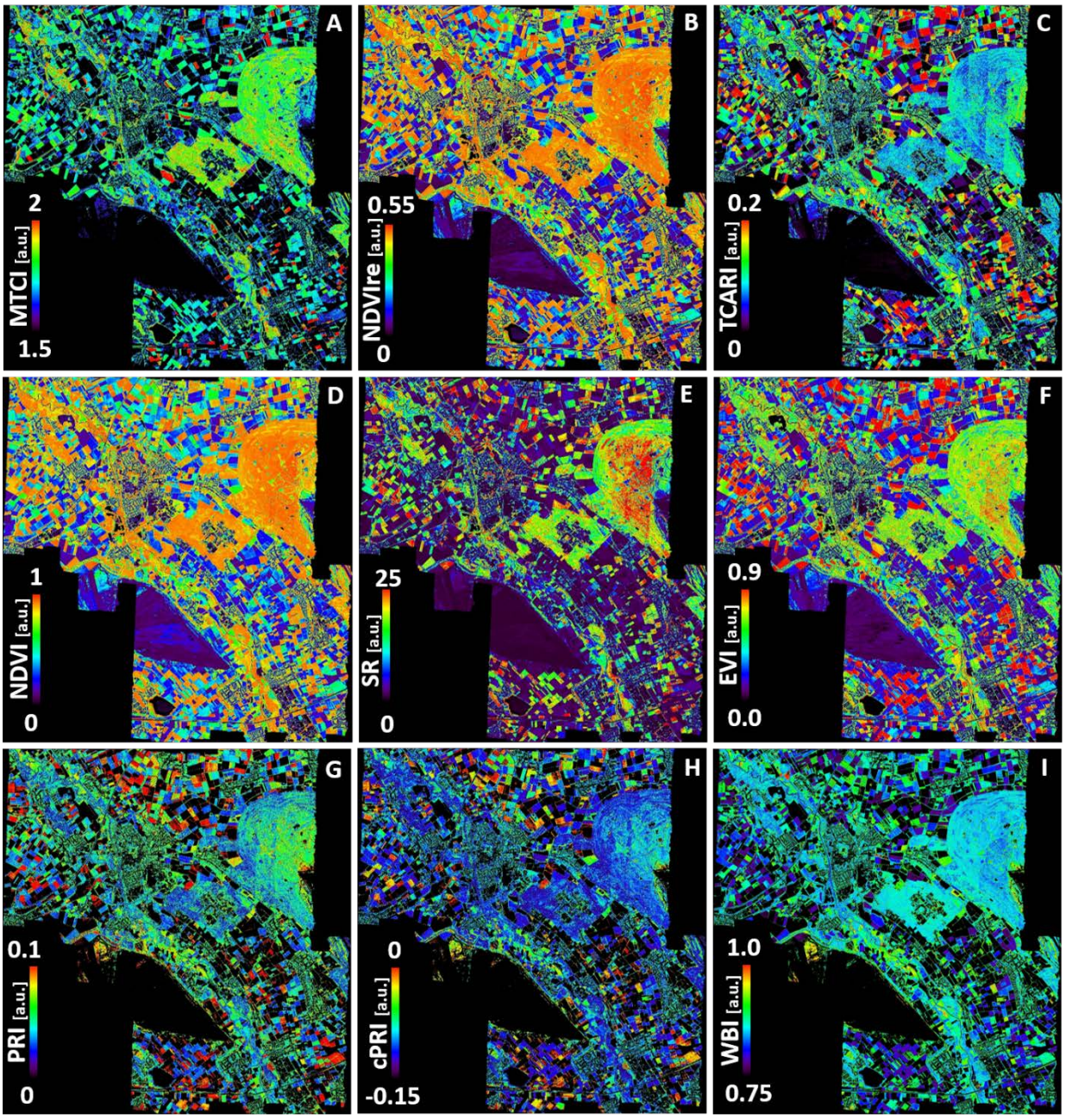

Figure 44: Maps of the anthropogenic, agricultural area around Jülich (TR32 map) showing different vegetation indices: MERIS terrestrial chlorophyll index (MTCI) (A); red-edge Normalized Difference Vegetation Index (NDVIre) (B); Transformed Chlorophyll Absorption Reflectance Index (TCARI) (C); Normalized Difference Vegetation Index (NDVI) (D); Simple Ratio (SR) (E); Enhanced Vegetation Index (EVI) (F); Photochemical Reflectance Index (PRI) (G); canopy Photochemical Reflectance Index (cPRI) (H); and Water Band Index (WBI) (I). Data were recorded on 19 July 2016.

6.1.1.2 Fluorescence maps of the TR32 map

Fluorescence maps calculated with the SFM

The 18 flight lines covering the TR32 area in Germany were used to retrieve sun-induced fluorescence (Table 26). The flight lines were collected on 19 July 2016 between 11:49 and the 13:43 local time for a total time span of 114 minutes, almost around noon. The flight lines were collected either with South (S) and North (N) direction heading. The flight lines were collected from an eight of 1632 m above the surface, resulting in a 2.5 m pixel resolution on the ground.

Table 26: List of *HyPlant* flight lines collected on July 19th, 2016 covering the TR-32 long-term monitoring area in Germany. The local time, heading and acquisition pattern (sequence) of each flight line are indicated.

ID	*File name*	*Local time (hh:mm)*	*Heading*	*Acquisition pattern*
1	20160719-TR32-1149-1800-L1-S	11:49	S	1
2	20160719-TR32-1158-1800-L2-S	11:58	S	3
3	20160719-TR32-1208-1800-L3-S	12:08	S	5
4	20160719-TR32-1153-1800-L4-N	11:53	N	2
5	20160719-TR32-1203-1800-L5-N	12:03	N	4
6	20160719-TR32-1213-1800-L6-N	12:13	N	6
7	20160719-TR32-1219-1800-L7-S	12:19	S	7
8	20160719-TR32-1225-1800-L8-N	12:25	N	8
9	20160719-TR32-1239-1800-L9-N	12:39	N	10
10	20160719-TR32-1306-1800-L10-N	13:06	N	13
11	20160719-TR32-1321-1800-L11-N	13:21	N	15
12	20160719-TR32-1313-1800-L12-S	13:13	S	14
13	20160719-TR32-1232-1800-L13-S	12:32	S	9
14	20160719-TR32-1246-1800-L14-S	12:46	S	11
15	20160719-TR32-1300-1800-L15-S	13:00	S	12
16	20160719-TR32-1327-1800-L16-S	13:27	S	16
17	20160719-TR32-1334-1800-L17-N	13:34	N	17
18	20160719-TR32-1343-1800-L18-S	13:43	S	18

The atmospheric parameters are derived from AERONET station FZJ-JOYCE located at the Research Centre Jülich (long=6.412; lat=50.908; elevation=108 m) in the centre of the recorded TR32 map (FZJ-JOYCE - AERONET Site Information Database). The available AERONET data were already available as version 2, with the highest quality check. The semi-automated script to process sun-photometer files was adapted to process the AERONET standard files Level 2.0. Several improvements were carried out to the previous script developed for Microtops, example of the latest version of the sun-photometer processing GUI. Figure 45 shows the output graphical interface displayed by the semi-automated script, in which the atmospheric model input parameters are displayed and synthetized in the format/unit required by MODTRAN. The semi-automatic processing approach , which is now also adapted to the AERONET standard files, greatly improved, simplified and made faster the overall set-up of input parameters for *HyPlant* processing for different sunphotometers (Microtops and Cimel) employed during different campaigns.
A summary of the atmospheric input parameters derived from the AERONET station JOYCE is given in Table 27. Flight lines marked with the same colour share the same input parameters as they were recorded close in time.

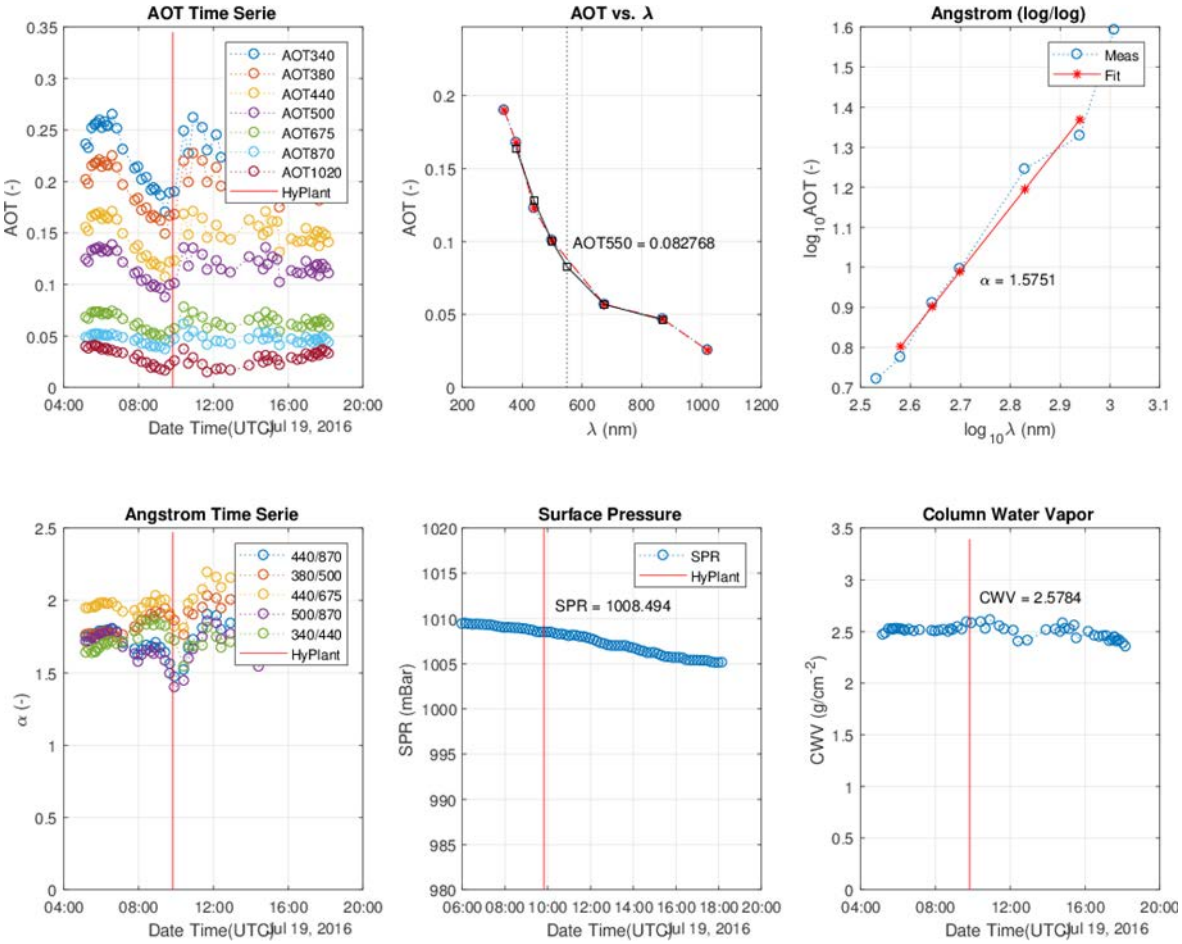

Figure 45: Atmospheric parameters derived from sun-photometer by the semi-automated script: Aerosol Optical Thickness (AOT) time series at different wavelengths collected during the campaign (top-left); AOT at different λ at the time of *HyPlant*, value at 550 nm is computed by interpolation (top-middle), logarithmic plot of AOT at different λ and retrieval of Angström α (top-right); Angström value computed by sun-photometer (bottom-left); surface pressure (SPR) (bottom-middle); column water vapour (CWV) (bottom-right). The vertical red line indicates the time of *HyPlant* imagery.

Table 27: Atmospheric parameters derived from AERONET station JOYCE in Jülich. The atmospheric parameters serve as input for the fluorescence retrieval with the spectral fitting methods. The colours indicate the flight lines, with the where same atmospheric conditions were assumed as they were recorded close in time.

	Flight-line																	
	L1	***L2***	***L3***	***L4***	***L5***	***L6***	***L7***	***L8***	***L9***	***L10***	***L11***	***L12***	***L13***	***L14***	***L15***	***L16***	***L17***	***L18***
AOD	0.082	0.082	0.082	0.082	0.082	0.113	0.113	0.113	0.096	0.110	0.105	0.105	0.113	0.096	0.110	0.105	0.09	0.091
GNDALT	0.108	0.108	0.108	0.108	0.108													
H1	1.800	1.800	1.800	1.800	1.800													
SPR*	1008	1008	1008	1008	1008	1008	1008	1008	1008	1008	1008	1008	1008	1008	1008	1008	1008	1008
MODEL																		
IHAZE																		
ASTMX	1.575	1.575	1.575	1.575	1.575	1.582	1.582	1.582	1.738	1.778	1.850	1.850	1.582	1.738	1.778	1.850	1.950	1.950
IPH																		
G																		
H2OSTR	2.58	2.58	2.58	2.58	2.58	2.59	2.59	2.59	2.52	2.61	2.55	2.55	2.59	2.52	2.61	2.55	2.52	2.52
TPTEMP																		
SZA	37.11	36.11	35.08	36.58	35.51	34.52	33.53	33.53	32.36	31.42	30.32	30.32	33.53	32.36	31.42	30.32	30.19	30.19

*Surface Pressure (SPR) data from meteorological station – measurement time frequency = 10 minutes

To evaluate the quality of the derived fluorescence maps an overall assessment of the entire airborne processing chain is the preferable approach; from in-flight characterization (using the SpecCal program), through atmospheric correction and the direct comparison of ground-truth values with final airborne fluorescence map. Nevertheless, an analyses of intermediate products from the processing chain can help to gain knowledge about the data quality and induvial processing steps.
The comparison of irradiance spectrum at surface measured by field spectrometer and modelled by atmospheric RT code, is one way to assess the quality of the atmospheric model input parameters and the consequent atmospheric correction of *HyPlant*. In 2016 unlucky, the ground-based measurements were not collected simultaneously to the airborne observations in the TR32 area. Therefore, it is not possible to have a quantitative but only a qualitative evaluation of the modelled irradiance spectra. Figure 46 shows the incoming irradiance spectra at surface level modelled by MODTRAN5 for each flight line. Most of the changes are related to the changes in solar zenith angle due to time span of almost two hours between first and last recorded flight line.

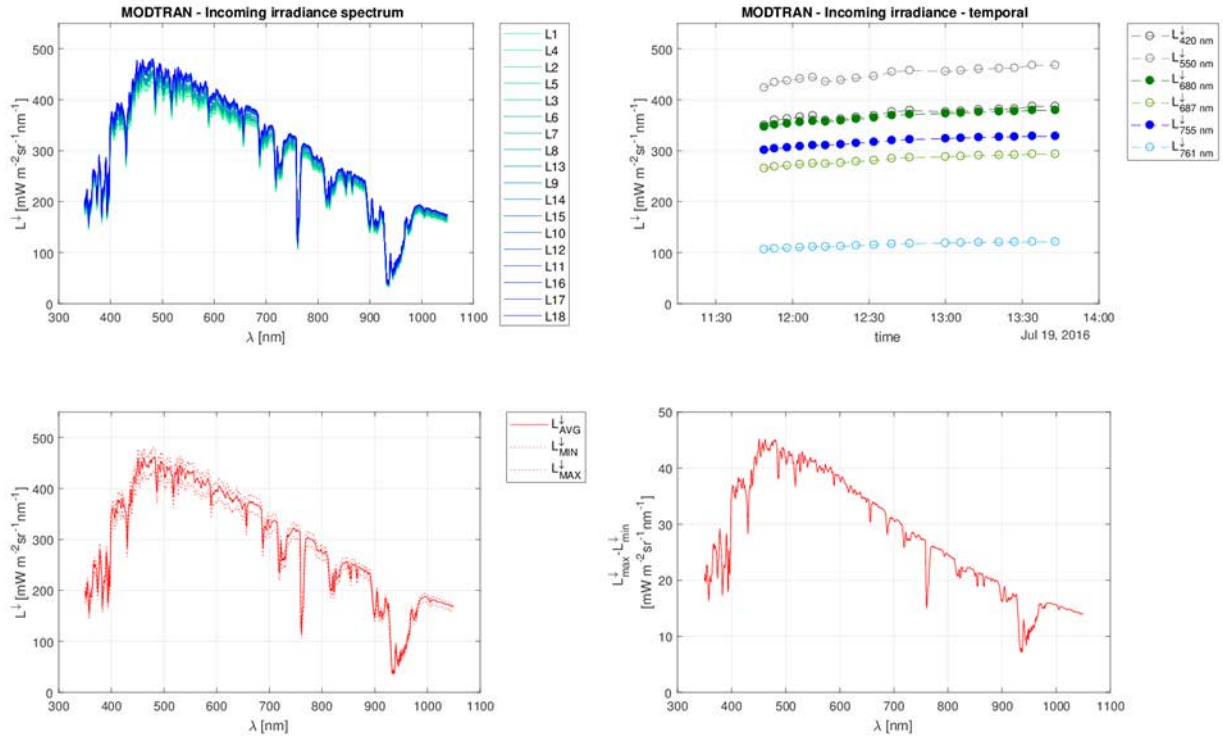

Figure 46: Incoming irradiance spectra at surface level for each flight line modelled by MODTRAN5, the original high-resolution spectra were resampled at spectral sampling of 1 nm, trapezoid SRF with FWHM = 3 nm (top-left). Average, minimum and maximum values (bottom-left). Monochromatic irradiance at selected wavelengths for the different flight lines, they grey lines represents 420 and 550 nm values, green/light green lines represent shoulder/well of O_2-B band, blue/light-blue the O_2-A band (top-right). Absolute difference between maximum and minimum incoming irradiance values (bottom-right).

An additional quality assessment is performed using the SPECCAL algorithm, to investigate the spectral stability of *HyPlant*. As one of the most important steps in the fluorescence retrieval from airborne and satellite instruments concerns is the convolution of high spectral resolution radiance simulations to actual instrument spectral bands, the spectral stability of the high resolution instrument is a crucial point. Although spectral characteristics such as the Full-Width-Half-Maximum (FWHM) and Spectral Shift (SS) are regularly characterized in the laboratory in the winter month, a further in-flight characterization is required for retrieving fluorescence because even slight changes may introduce relevant errors. Therefore, the variation

of these parameters in the spatial direction of the sensor (image columns) must be also characterized to obtain accurate fluorescence values. Figure 47 shows the FWHM and SS, for the O_2-A and O_2-B bands, retrieved from the different flight lines of the TR32 map. Values estimated from the different imageries show similar behaviour in the across-track direction of the image (spatial direction of the CCD), lower values were found in the middle of the sensor and slightly larger values at the edges. This behaviour could be addressed at two different effect: i) usually, the optical path alignment is optimized for the centre of the instrument; ii) the current retrieval algorithm does not include yet the correction for the different viewing angles, therefore larger values can occur for the off-nadir pixels. However, the overall results gained for the 18 different flight lines show a very good agreement for both FWHM and SS. This result raises from three main reasons: i) *HyPlant* spectral stability; ii) SpecCal algorithm consistency on different flight-lines; iii) good characterization of atmospheric parameters (i.e., O_2-band depth).

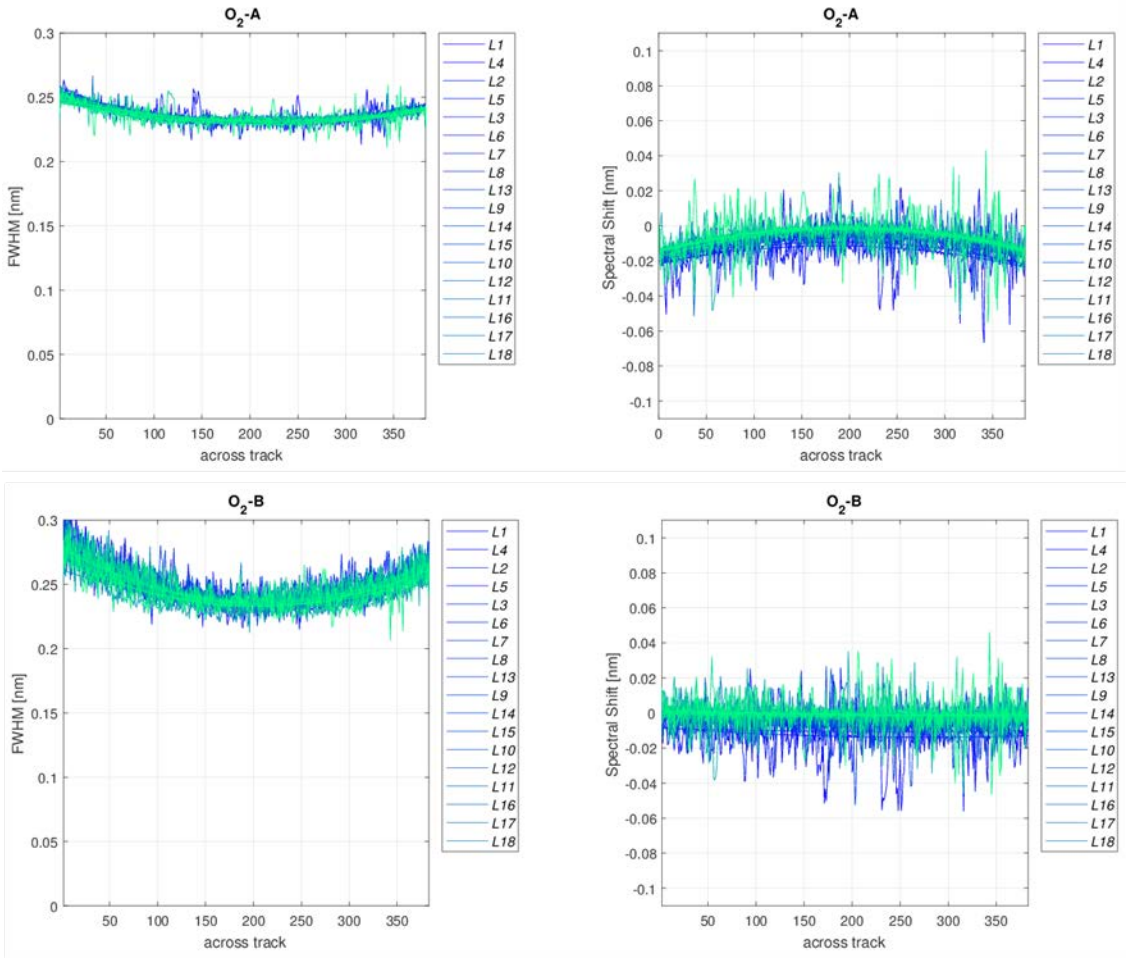

Figure 47: Full Width at Half Maximum (FWHM) and spectral shift (SS), for O_2-A and O_2-B bands, along the imagery across-track direction (image columns) estimated during in-flight conditions (SpecCal). The lines colours refer to the different flight-lines in the core-dataset.

Fluorescence maps calculated with the SFM (not deconvolved)

The fluorescence maps presented in Figure 49 were calculated on at-sensor radiance images, with no deconvolution applied to correct for the PSF. The frequency distribution of the O_2-A and O_2-B band fluorescence values of each complete flight line is given in Figure 48. As already evaluated in the final report in 2015 [RD-4] absolute fluorescence values on the O_2-A and O_2-B band are overestimated when no deconvolution is applied to the spectrum.
The magnitude of the far-red fluorescence values (SIF_{76}) calculated with the SFM (Figure 48 left and Figure 49 B) ranges from 0 up to 5 mW/m²/sr/nm for some surface types. Highest F_{760}_SFM values appear in dense green vegetation such as forest and sugar beet fields while non-vegetation pixels show lower values. However those non-vegetation pixel do often not reach fluorescence values of zero, but show some signal in the O_2-A band (Figure 48 left). Nevertheless, the frequency distribution of the Far-red maps seems to be rather constant between the different flight lines (Figure 48 left). But it should be noted that the far-red fluorescence map does appear blurry and sharp edges such as field corners and buildings are not clearly visible compared to the false colour image (Figure 49 A, B).
The red-fluorescence map (Figure 49 C) shows mainly values ranging from 0 to 3 mW/m²/sr/nm (Figure 48 right) with maximum values in dense green vegetation such as sugar beet. Non vegetation pixels, such as streets and water show SIF_{687} values close to zero (Figure 49 C). However, some non-vegetation pixel such as the pet mining area show unrealistic high SIF_{687} values, as an artefact of the SFM algorithm. In general, the red fluorescence map is sharp and structures such as single field, streets etc., are clearly visible.

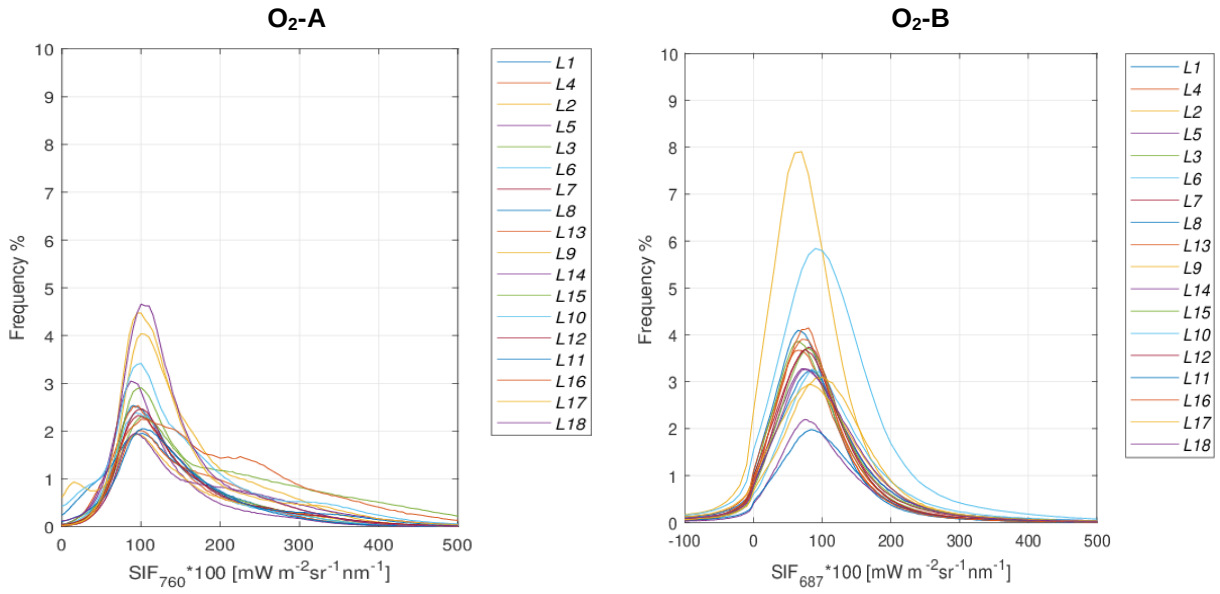

Figure 48: Distribution of fluorescence values for the entire imageries at O_2-A (left) and O_2-B (right) bands retrieved on the full image of all 18 flight lines of the TR32 map. Red and far-red fluorescence maps were derived from the not deconvolved images.

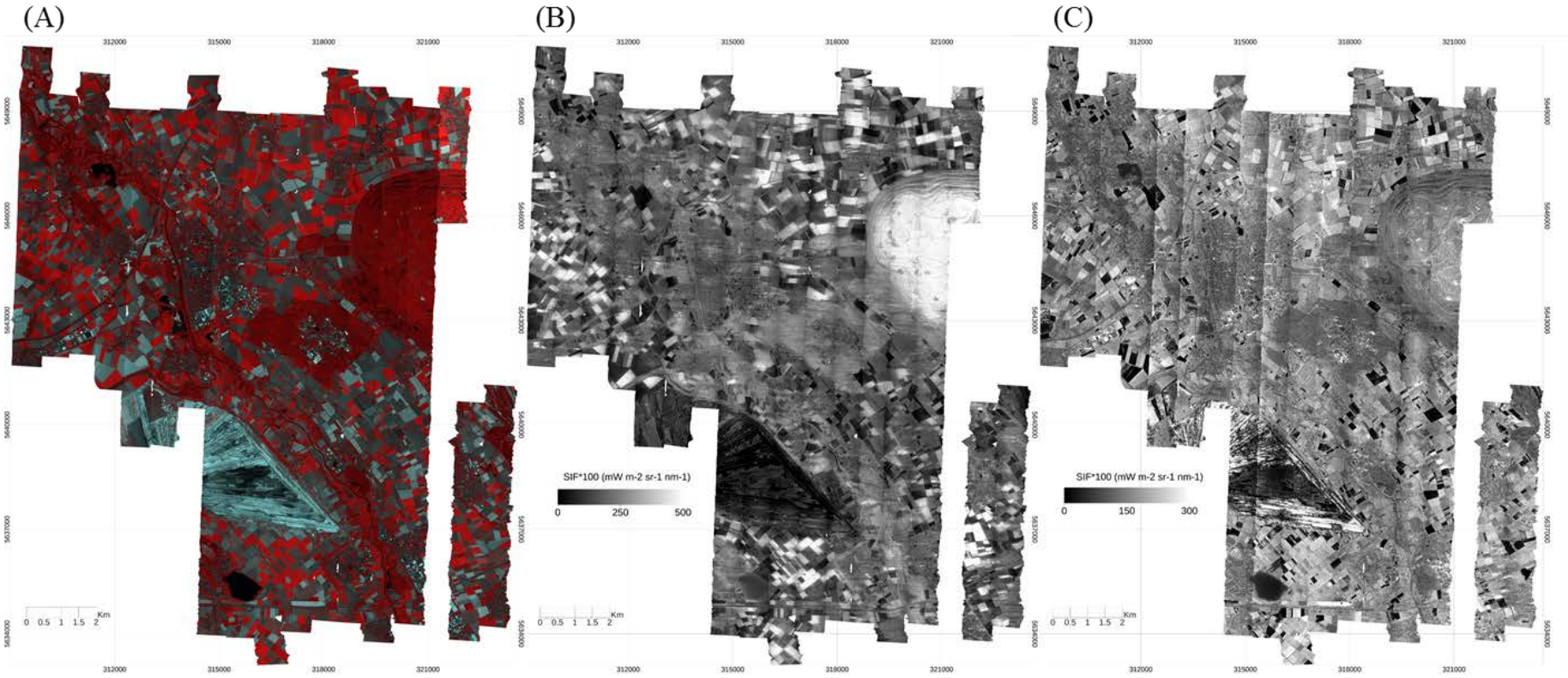

Figure 49: Maps of the anthropogenic, agricultural area around Jülich (TR32 map), Germany. (A) Reference false colour composite; (B) far-red fluorescence map retrieved at O_2-A band; (C) red fluorescence retrieved at O_2-B band. The fluorescence maps were derived with the Spectral Fitting method from the not deconvolved imagery which were recorded on 19 July, 2016.

Fluorescence maps calculated with the SFM (deconvolved)

The red and far-red fluorescence maps calculated from deconvolved at-sensor radiance are presented in Figure 51. For both red and far-red fluorescence maps the values are in general lower than from the not-deconvolved data (Figure 50), most likely due to an overcorrection of the currently applied PSF deconvolution algorithm [RD-4]. In a previous version of the SFM algorithms pixels with a low signal combined with the large amount of noise introduced by the deconvolution algorithm were automatically set to zero. Those boundaries for the fluorescence retrieval for the SFM are not set in the current versions of the algorithm anymore (details see chapter 4.1.1.2). That results in negative red fluorescence values, especially for the red fluorescence derived in the O_2-B band. The majority of the SIF_{687} values range mainly between -3.5 to 2 mW/m^2/sr/nm (Figure 50 right). Although negative values appear in the red fluorescence maps, the overall pattern seems meaningful showing highest values for green dense vegetation such as sugar beet and lowest values for soil and other non-vegetation pixels such as streets. In addition the image appears sharp.
As the radiance signal is in general stronger in the O_2-A band at 760 nm, the far-red fluorescence maps are not affected by negative fluorescence values and SIF_{760} ranges from 0 to 3 mW/m^2/sr/nm (Figure 50 left, Figure 51 B). Highest fluorescence values appear in dense vegetation and especially in the recultivated forest area of the 'Sofienhöhe', in the north-eastern part of the image. The Sofienhöhe is an artificial hill built from the pet mining soil, which was reforested decades ago and presents the only hill in an otherwise flat terrain. Previous top-of-canopy fluorescence measurements in needle and deciduous leaf forest showed that the far-red fluorescence values range up to 1 mW/m^2/sr/nm for needle forest and up to 1.5 to 2 mW/m^2/sr/nm for decisions leaf forest species. Therefore, overestimation of the fluorescence values of the forest of the 'Sofienhöhe` might be related to the fact that so far changes in the elevation and terrain are not considered in the fluorescence retrieval algorithm. However, this needs to be investigated in the future.

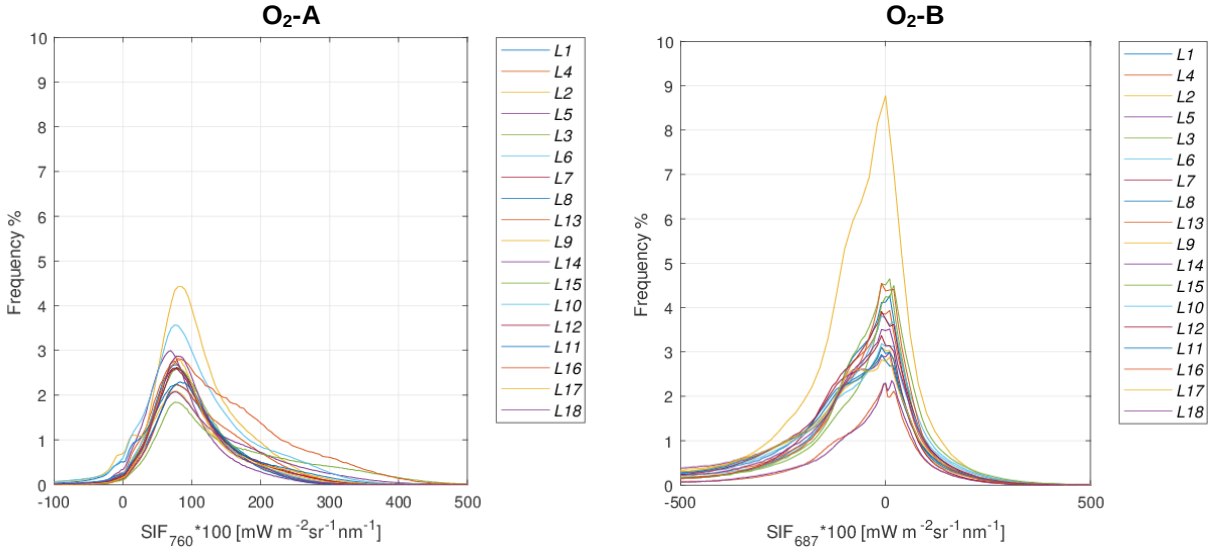

Figure 50: Distribution of fluorescence values for the entire imageries at O_2-A (left) and O_2-B (right) bands retrieved on the full image of all 18 flight lines of the TR32 map. Red and far-red fluorescence maps were derived from the deconvolved images.

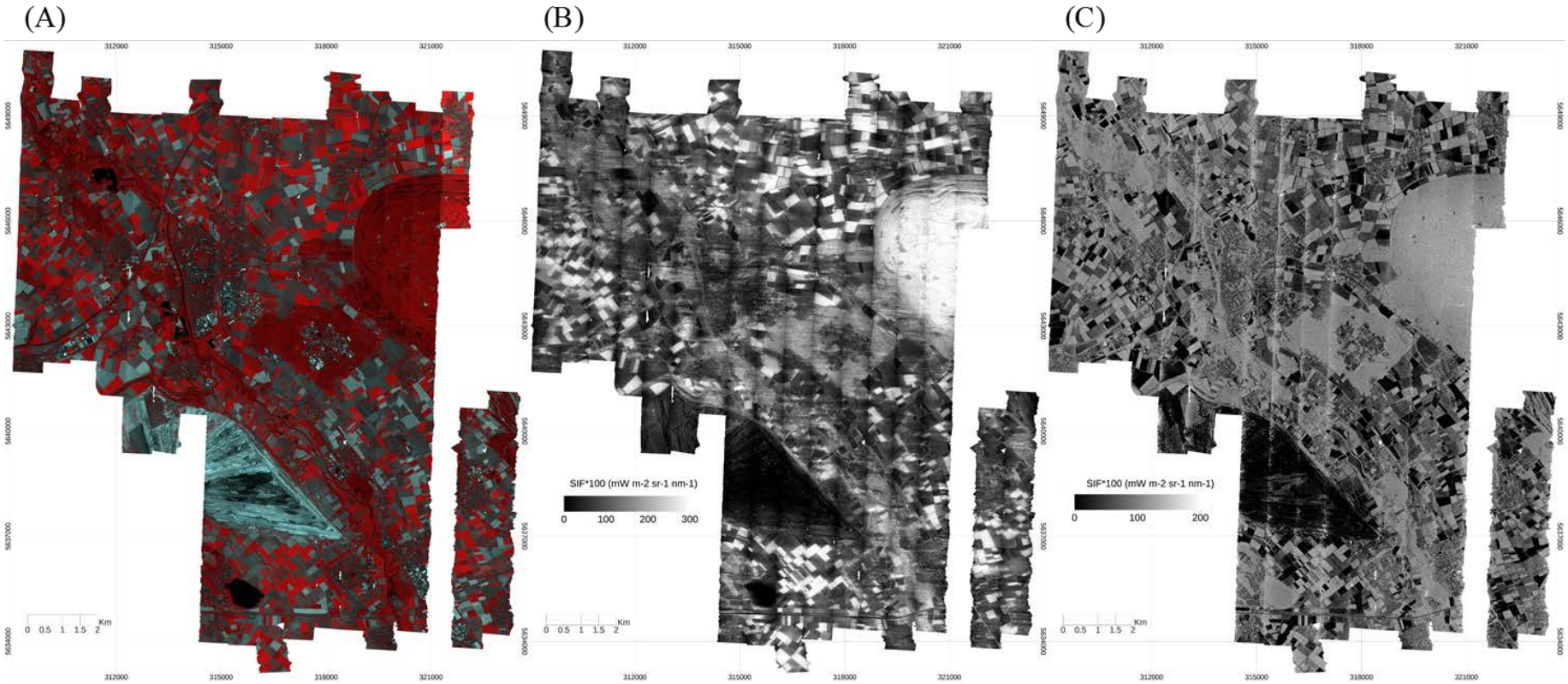

Figure 51: Maps of the anthropogenic, agricultural area around Jülich (TR32 map), Germany. (A) Reference false colour composite; (B) far-red fluorescence map retrieved at O_2-A band; (C) red fluorescence retrieved at O_2-B band. The fluorescence maps were derived with the Spectral Fitting method from the deconvolved imagery which were recorded on 19 July, 2016.

Fluorescence maps calculated with the iFLD method

Red and far-red fluorescence maps of the large TR32 map were also calculated with iFLD method. The red fluorescence map (Figure 52) shows values from 0 to 1 mW/m²/sr/nm, while the far-red fluorescence map (Figure 53) show values from zero up to 2.5 mW/m²/sr/nm. Those value ranges are in line with TOC fluorescence measurements of different vegetation types collected over the previous years (Rossini *et al.* 2016). In addition, the overall pattern in both fluorescence maps is consistent showing the highest values in the dense green vegetation such as sugar beet and values close to zero for non-vegetation pixels.

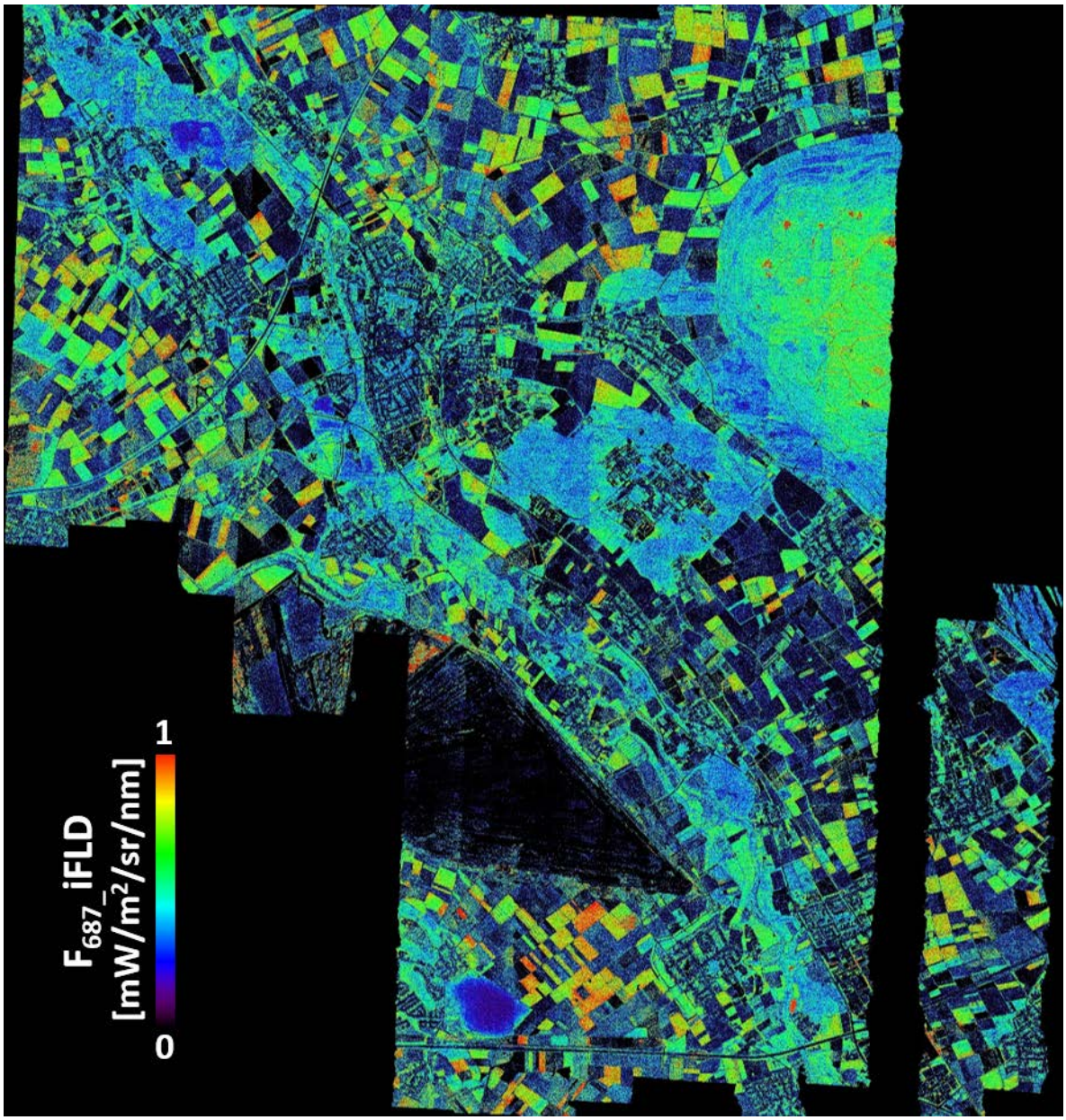

Figure 52: Red fluorescence map based on the improved Fraunhofer Line Discrimination (F_{687}_iFLD) of the anthropogenic, agricultural area around Jülich (TR32 map) recorded on 19 July 2016.

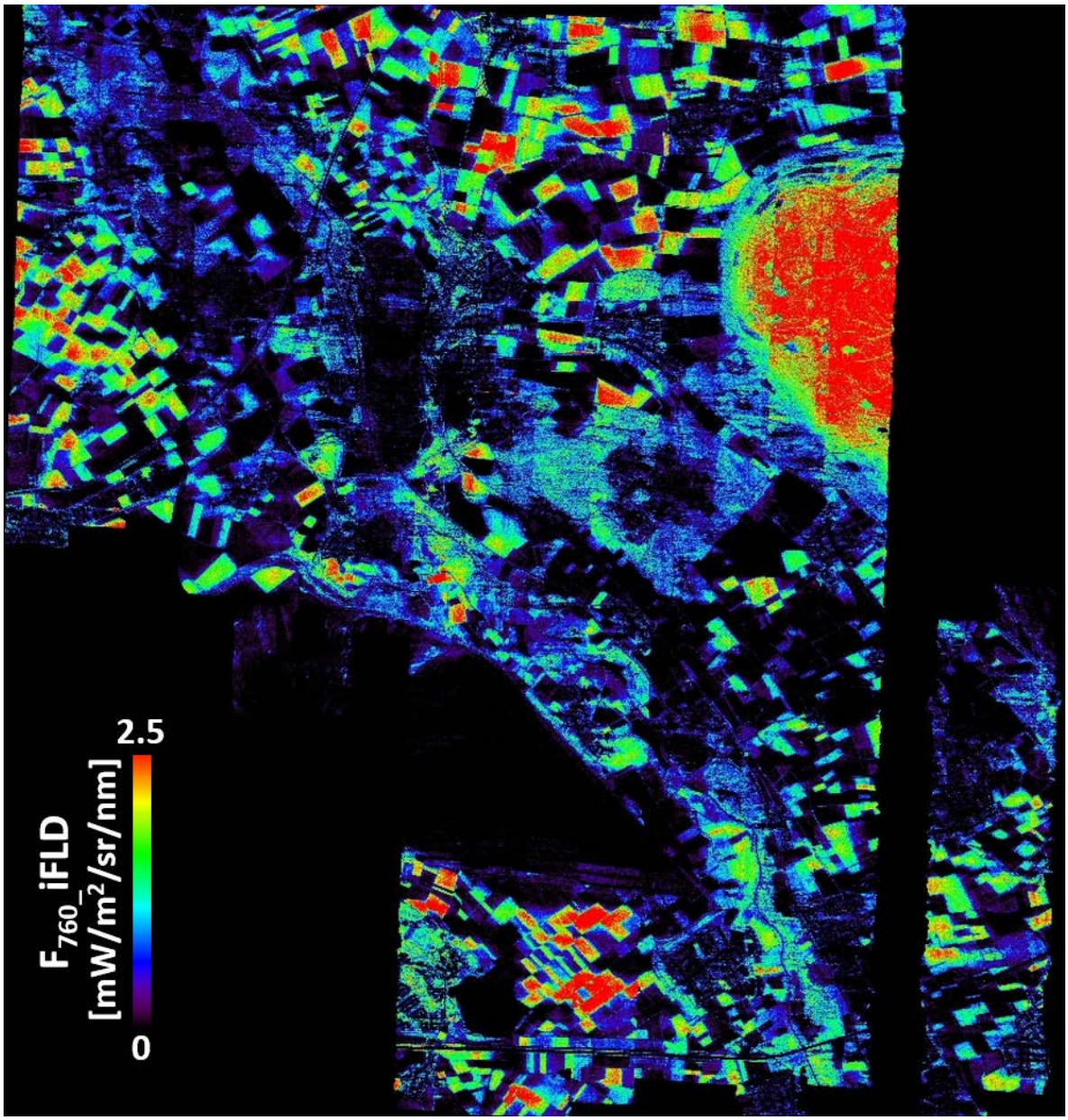

Figure 53: Far-red fluorescence map based on the improved Fraunhofer Line Discrimination (F_{687}_iFLD) of the anthropogenic, agricultural area around Jülich (TR32 map) recorded on 19 July 2016.

Comparison of the large TR32 map calculated with the SFM and the iFLD method

Fluorescence maps calculated with the *Spectral Fitting Method* (Figure 51) and the iFLD (Figure 52, Figure 53) method were also compared on field scale for different vegetation types and bare soil field. At the time of the *HyPlant* overpass (19 July 2016) the agricultural crops, namely sugar beet, maize and potatoes were still green, dense and photosynthetic active (Figure 54). Other crops such as (winter-) wheat and barley were already senescent and partly harvested at that time. The harvested fields are included a non-vegetation (bare soil) fields in the following comparison.

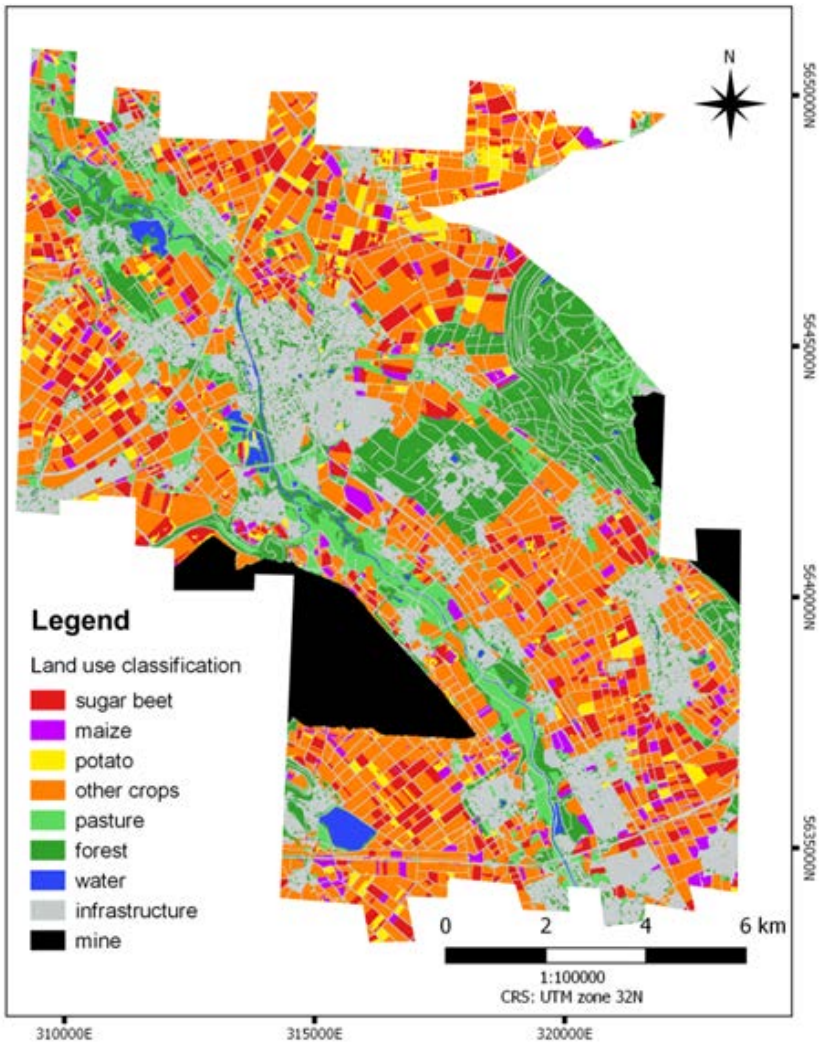

Figure 54: Land use map of the anthropogenic, agricultural area around Jülich. Sugar beet, Maize and potatoes are the main still green vegetation types on 19 July 2016, the day of the *HyPlant* overpass.

From the land use classification (Figure 54) 280 sugar beet fields, 158 maize fields 182 potato fields and 12 bare soil fields, which where for sure already harvested at the time of the data acquisition, were selected for further analyses. To eliminate possible border effects/artifacts of the fields a buffer of 2-3 pixels was excluded. The average and standard deviation of the remaining pixels per field were calculated. The distribution of the average field values of the red and far-red fluorescence from the SFM and iFLD method are presented in Figure 55.

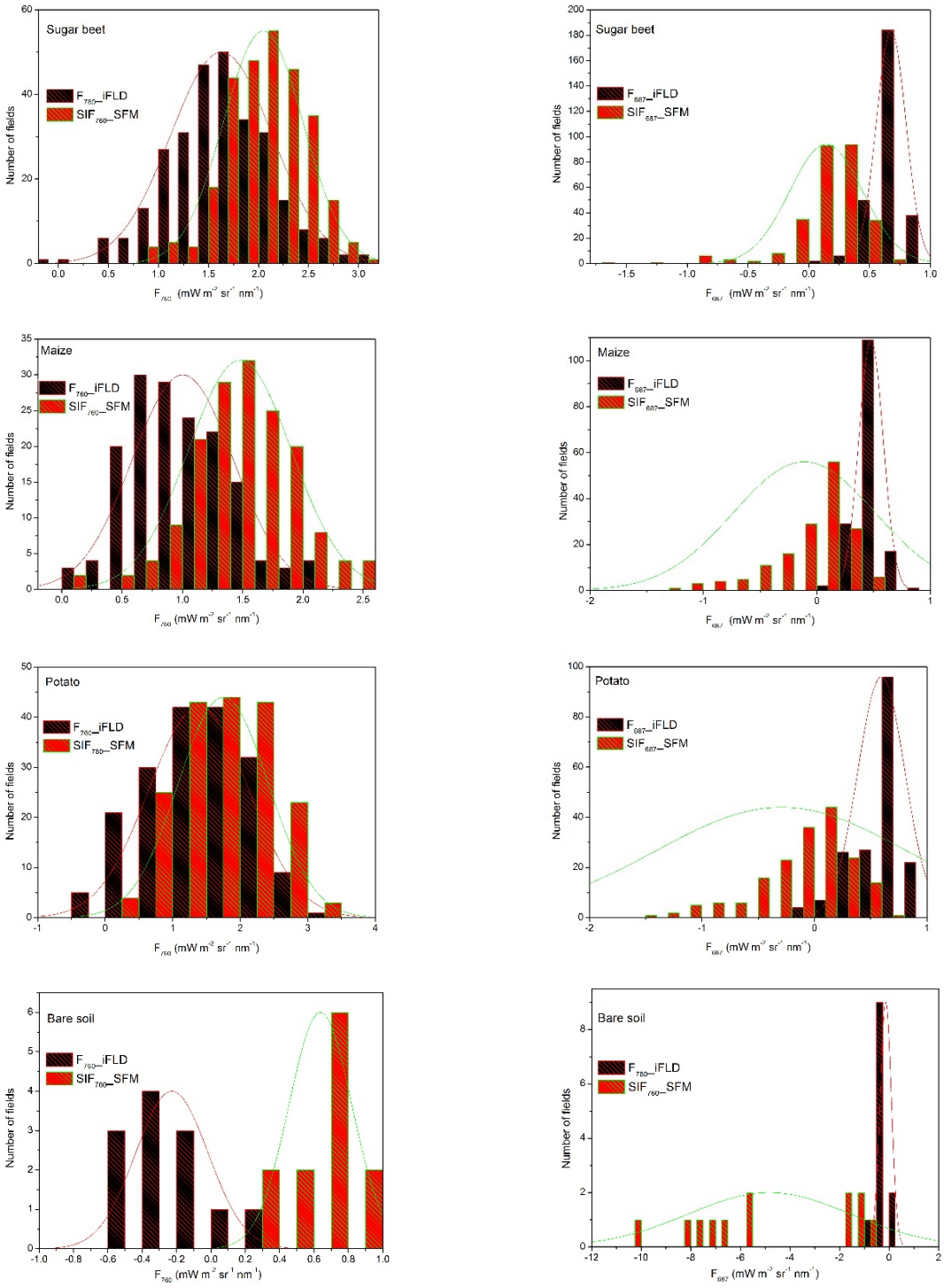

Figure 55: Distribution of far-red (left column) and red (right column) fluorescence values calculated from deconvoluted data with the Spectral Fitting Method (SFM) and the Improved Fraunhofer Line Discrimination (iFLD) averaged per field. 280 sugar beet fields, 158 maize fields 182 potato fields and 12 bare soil fields are included in the analyses.

For all three vegetation types, especially sugar beet and maize, the far-red fluorescence values averaged per field are higher for Spectral Fitting Method (SIF_{760}_SFM) that for the improved Fraunhofer Line Discrimination (F_{760}_iFLD) (Figure 55). However, the red fluorescence values derived from the O_2-B band show a different picture. The SIF_{687}_SFM are lower than the F_{687}_iFLD values for these vegetation types. As already presented in the histogram for the complete flight lines (Figure 50 right) the SIF_{687}_SFM show also negative values for all three vegetation types. While the maximum of the SIF_{687}_SFM distribution is slightly positive or around zero for sugar beet and maize, the maximum of the distribution for the potato is negative (Figure 55). The far-red fluorescence distribution of the bare soil fields, shows zero to slightly negative values for F_{760}_iFLD but only positive values for SIF_{760}_SFM. The red fluorescence values show values close to zero for the F_{760}_iFLD and unexceptional negative values for SIF_{760}_SFM.
The standard deviation of each field was calculated as well and given an idea about the variability of the fluorescence values of the maps. The averaged standard deviation of all fields for the different species in given in Table 28. In general the Spectral fitting Method shows a higher variability than the iFLD method, especially for the O_2-B band.

Table 28: Averaged standard deviation (mW/m²/sr/nm) of red-and far-red fluorescence of all sugar beet, maize potatoes and bare soils fields, calculated with the Spectral Fitting Method (SFM) and the improved Fraunhofer Line Discrimination (iFLD).

	Sugar beet	**Maize**	**Potato**	**Bare soil**
SIF_{687}_SFM	0.64	0.82	1.14	2.14
SIF_{760}_SFM	0.40	0.34	0.39	0.33
F_{687}_iFLD	0.18	0.18	0.23	0.39
F_{760}_iFLD	0.32	0.27	0.32	0.20

Concluding remarks

For the first time within the *HyPlant* campaigns it was possible to retrieve red and far-red fluorescence maps from a large area consisting of 18 flight lines using two different retrieval methods: the SFM (Figure 51) and the iFLD (Figure 52 and Figure 53). Both methods show in general consistent patterns with highest fluorescence values in green dense vegetation and low values in non-vegetation pixels. The value range of the red- and far-red fluorescence maps calculated with the iFLD method (Figure 52 and Figure 53) are in the expected range, comparable to TOC measurements of single vegetation types collected in previous years. The value range of the SFM however, is not always in the expected range. Especially the red fluorescence maps show negative values for vegetation and especially non vegetation pixels. In general the variability/noise of the SFM fluorescence maps higher than for the iFLD fluorescence maps. It was already reported in 2015 [RD-4] that the deconvolution of the PSF has large influence on the SFM retrieval, introducing noise and overcorrecting the signal. Those issues are still present and need to be further investigated and improved.

6.1.1.3 Vegetation indices and fluorescence maps of the Selhausen area

Figure 56: True colour map (R: 157, G: 105, B: 52) of the anthropogenic, agricultural area around Selhausen. Data were recorded on 19 July 2016.

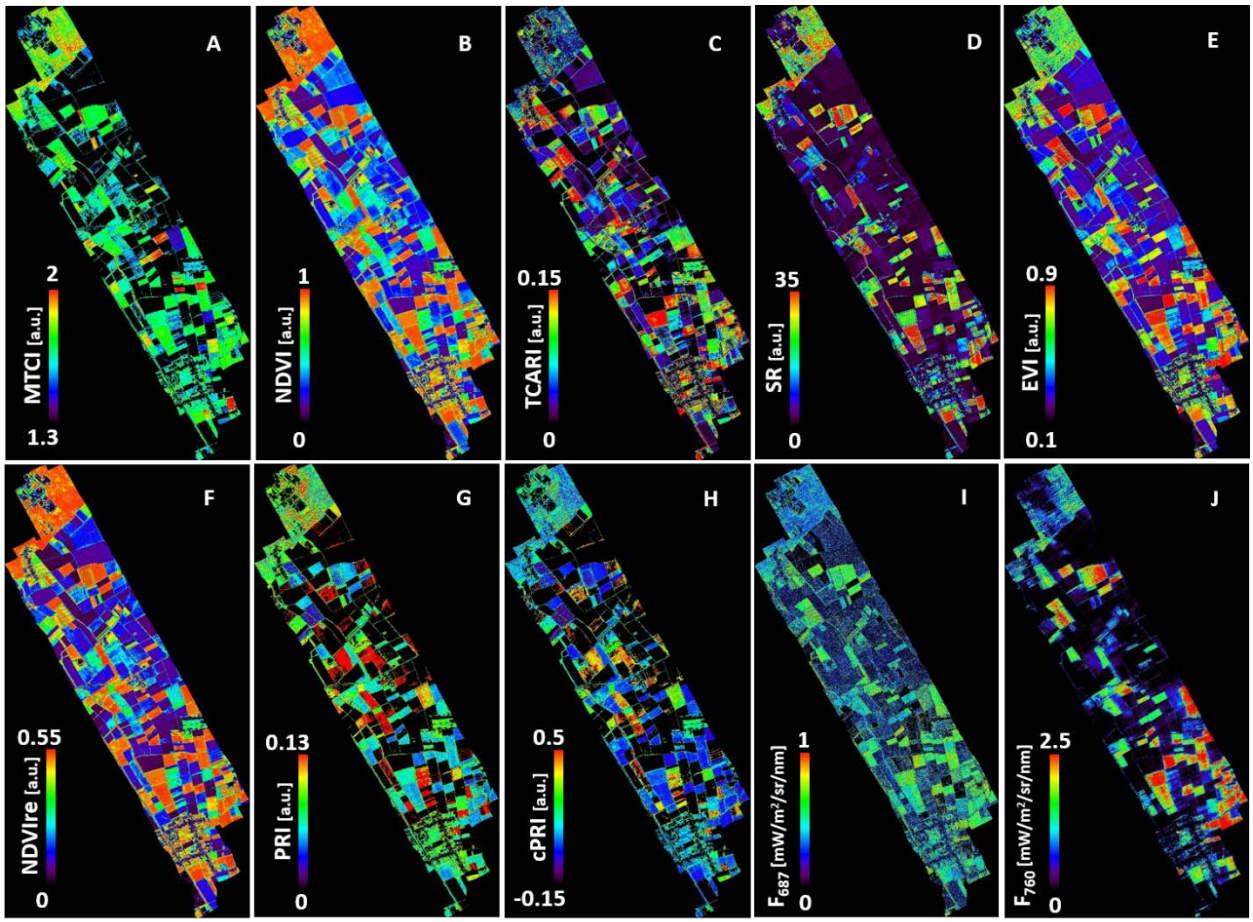

Figure 57: Maps of the agricultural area around Selhausen showing different selected vegetation indices: MERIS terrestrial chlorophyll index (MTCI) (A); Normalized Difference Vegetation Index (NDVI) (B); Transformed Chlorophyll Absorption in Reflectance Index (TCARI) (C); Simple Ratio (SR) (D); Enhanced Vegetation Index (EVI) (E); Red-Edge Normalized Difference Vegetation Index (NDVIre) (F); Photochemical Reflectance Index (PRI) (G) and canopy Photochemical Reflectance Index (cPRI) (H); fluorescence at 687 (F_{687}) (I) and fluorescence at 760 (F_{760}) (J) calculated with the iFLD method. Data were recorded on 19 July 2016.

6.1.2 Agricultural research Campus Klein-Altendorf

Figure 58: True colour map (R: 157, G: 105, B: 52) of the research campus Klein-Altendorf. Data were recorded on 20 July 2016.

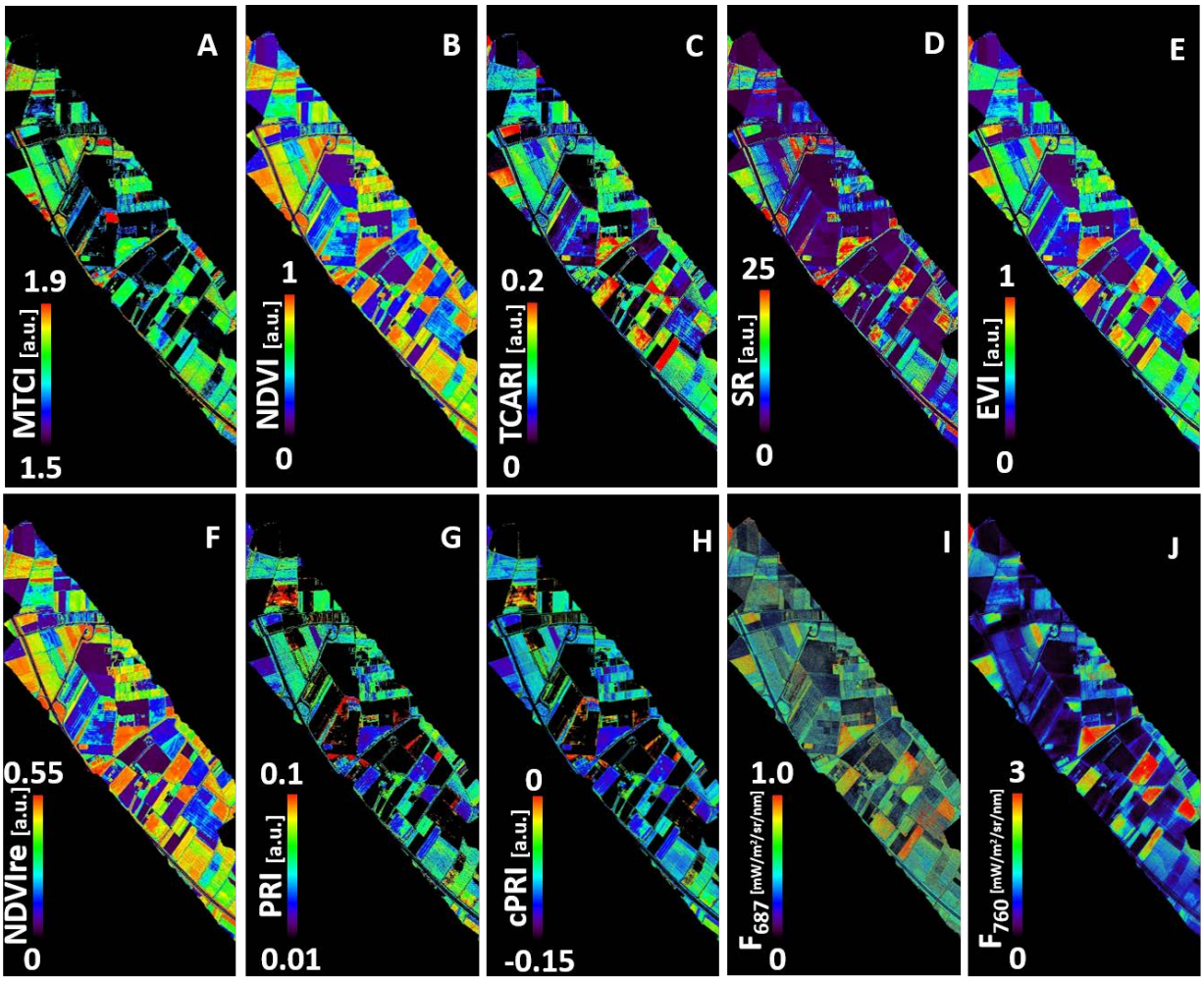

Figure 59: Maps of the research campus Klein-Altendorf showing different selected vegetation indices: MERIS terrestrial chlorophyll index (MTCI) (A); Normalized Difference Vegetation Index (NDVI) (B); Transformed Chlorophyll Absorption in Reflectance Index (TCARI) (C); Simple Ratio (SR) (D); Enhanced Vegetation Index (EVI) (E); Red-Edge Normalized Difference Vegetation Index (NDVIre) (F); Photochemical Reflectance Index (PRI) (G) and canopy Photochemical Reflectance Index (cPRI) (H); fluorescence at 687 (F_{687}) (I) and fluorescence at 760 (F_{760}) (J) calculated with the iFLD method. Data were recorded on 20 July 2016.

6.1.3 Forest area in Bílý Kříž, Czech Republic

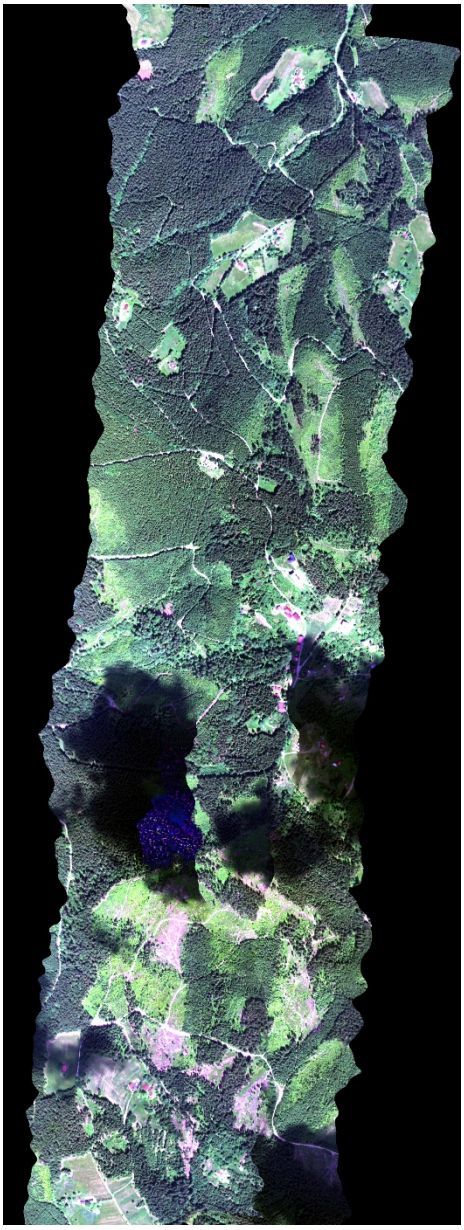

Figure 60: True colour map (R: 157, G: 105, B: 52) of Bílý Kříž recorded on 7 June 2016.

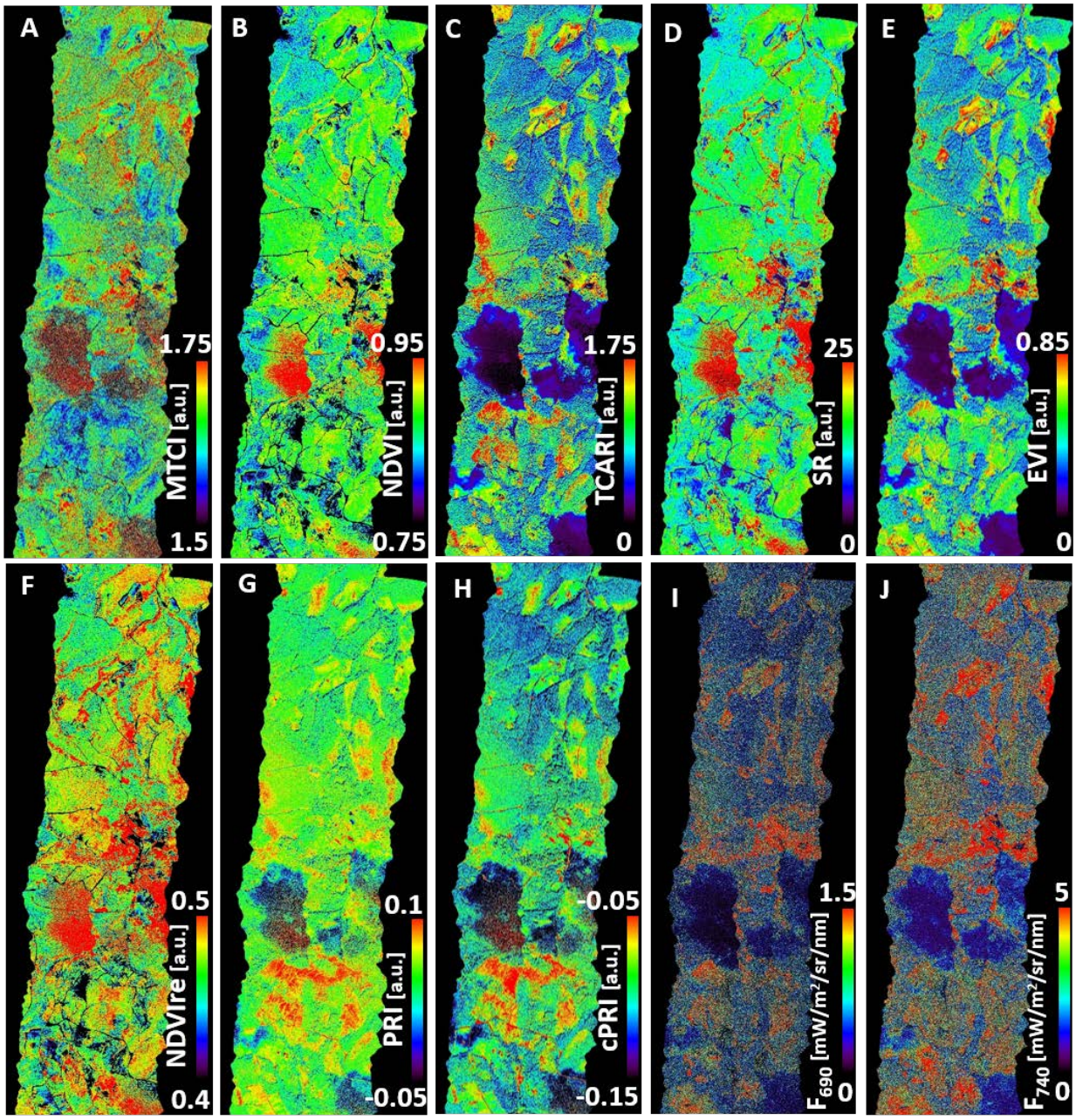

Figure 61: Maps of Bílý Kříž showing different vegetation indices: MERIS terrestrial chlorophyll index (MTCI) (A); Normalized Difference Vegetation Index (NDVI) (B), Transformed Chlorophyll Absorption in Reflectance Index (TCARI) (C); Simple Ratio (SR) (D); Enhanced Vegetation Index (EVI) (E); Red-Edge Normalized Difference Vegetation Index (NDVIre) (F); Photochemical Reflectance Index (PRI) (G) and canopy Photochemical Reflectance Index (cPRI) (H); fluorescence at 690 (F_{690}) (I) and fluorescence at 740 (F_{740}) (J) calculated with the SVD method. Data were recorded on 7 June 2016.

6.2 Vegetation indices and fluorescence maps and of the SoyFLEX2 experiment

In this chapter the true colour images (Figure 62), vegetation indices (Figure 63) and fluorescence maps retrieved with the iFLD (Figure 64) and SFM (Figure 67) are presented. Red and far-red fluorescence maps of both method are validated with TOC ground measurements (section 6.2.3).

Figure 62: True colour image (R: 157, G: 105, B: 52) of the SoyFLEX2 experimental site in Udine, (Italy) recorded on 22 July 2016.

6.2.1 Vegetation indices of the SoyFLEX2 experiment

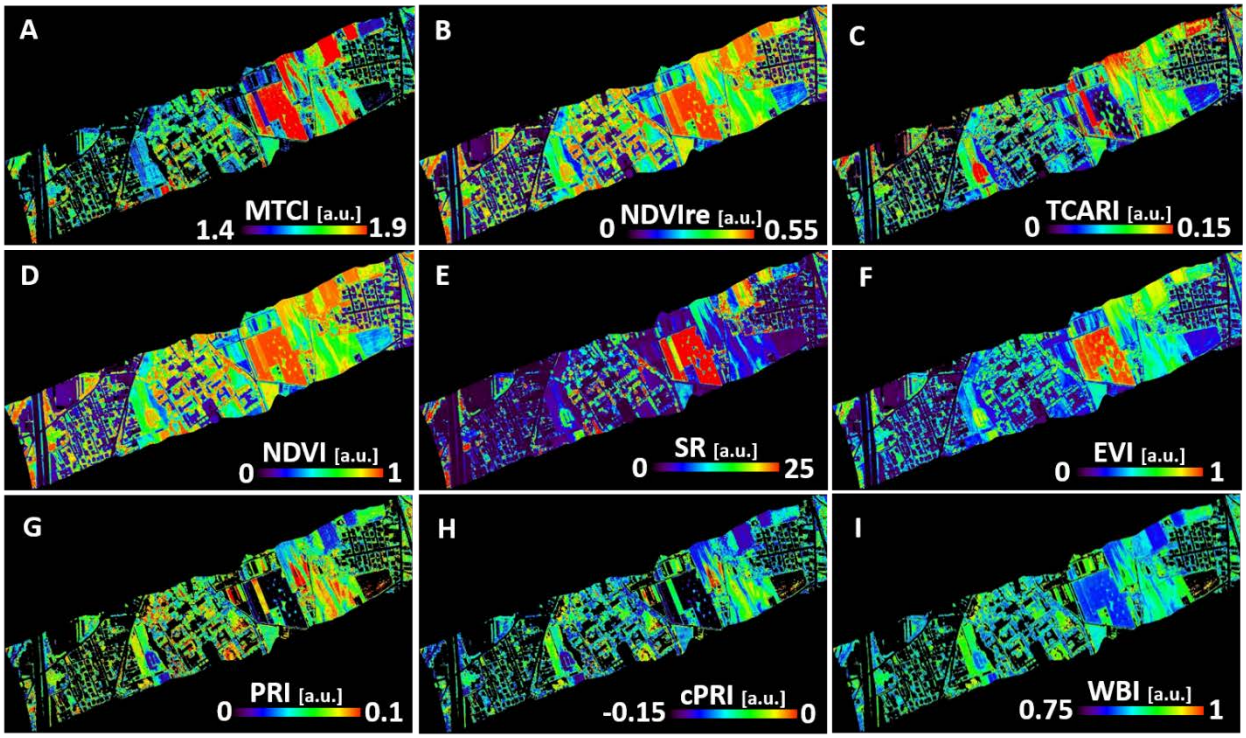

Figure 63: Maps of the SoyFLEX2 experimental site in Udi (Italy) showing different vegetation indices: MERIS terrestrial chlorophyll index (MTCI) (A); red-edge Normalized Difference Vegetation Index (NDVIre) (B); Transformed Chlorophyll Absorption Reflectance Index (TCARI) (C); Normalized Difference Vegetation Index (NDVI) (D); Simple Ratio (SR) (E); Enhanced Vegetation Index (EVI) (F); Photochemical Reflectance Index (PRI) (G); canopy Photochemical Reflectance Index (cPRI) (H); and Water Band Index (WBI) (I). Data were recorded on 22 July 2016.

6.2.2 Red and far-red fluorescence maps of the SoyFLEX 2 experiment

6.2.2.1 Improved Fraunhofer line discrimination (iFLD)

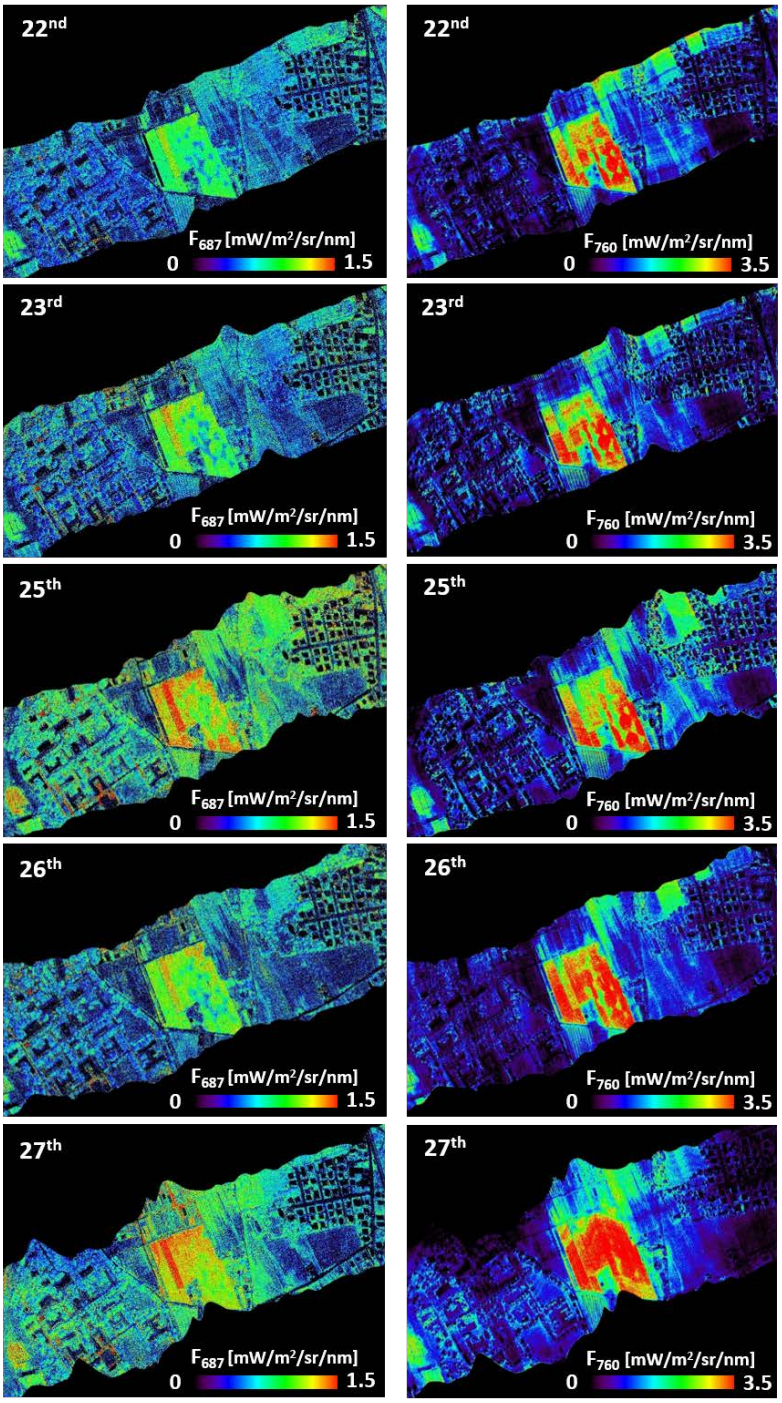

Figure 64: Maps of red (F_{687}) and far-red (F_{760}) fluorescence of the SoyFLEX2 experiment retrieved with the iFLD method. Presented are the flight lines of the core dataset, which were recorded between 22-27 July 2016.

6.2.2.2 Spectral Fitting Method

The Spectral Fitting retrieval algorithm were not applied in its complete form i.e. RT atmospheric forward modelling and successive canopy reflectance and fluorescence decoupling, as in FLEX configuration. This was due by the fact that atmospheric conditions were not always optimal during the five *HyPlant* measurement days. A first indication about the uncertainties in the illumination conditions between sunphotometer measurements and irradiance at surface level measured by field spectrometer is reported in Figure 65. In particular, we compared the irradiance spectrum at surface measured by field spectrometer and spectra simulated by MODTRAN5. The field spectrometer measurements collected as much as possible simultaneous to *HyPlant* overflights were extracted from the campaign data set. The irradiance spectra at surface level were simulated by MODTRAN5 considering the same model input parameters used to retrieve fluorescence from *HyPlant*. These values were derived from sunphotometer measurements as much as possible simultaneous to airborne overflight.

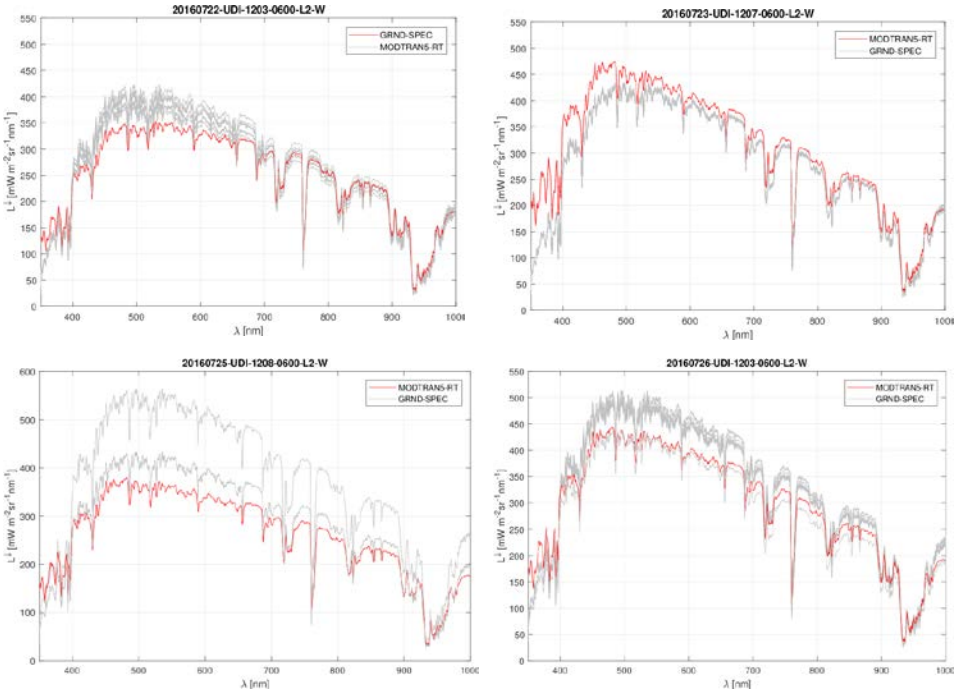

Figure 65: Comparison of irradiance spectrum at surface between field spectrometer measurements (grey lines) and MODTRAN5 simulations (red lines) corresponding to the different *HyPlant* flight lines. Ground-based data are not available on July 27th.

The irradiance spectra measured by field spectrometer during the experiment days show a broad range of variation, that it is symptomatic of not optimal clear-sky conditions. For example, the range of variation in the visible part of the spectrum shows changes in the order of 50 mW m^{-2} sr^{-1} nm^{-1} for July 22nd. The measurement conditions look even more challenging on July 25th and 26th.
A similar analysis was carried out directly comparing the radiance detected by *HyPlant* reference targets pixels available in the experimental area and the radiance signature detected by airborne sensor. The *HyPlant* radiance of tarps pixels were corrected for the actual reflectance signature measured by the ASD field spectrometer. Figure 66 shows the error in modelling the radiance signature around the O_2-A and O_2-B bands for the white reference tarp. The absolute error for O_2-A was around 5 mW/m-2/sr-1/nm-1 and larger than 10 mW m^{-2} sr^{-1} nm^{-1} at O_2-B band.

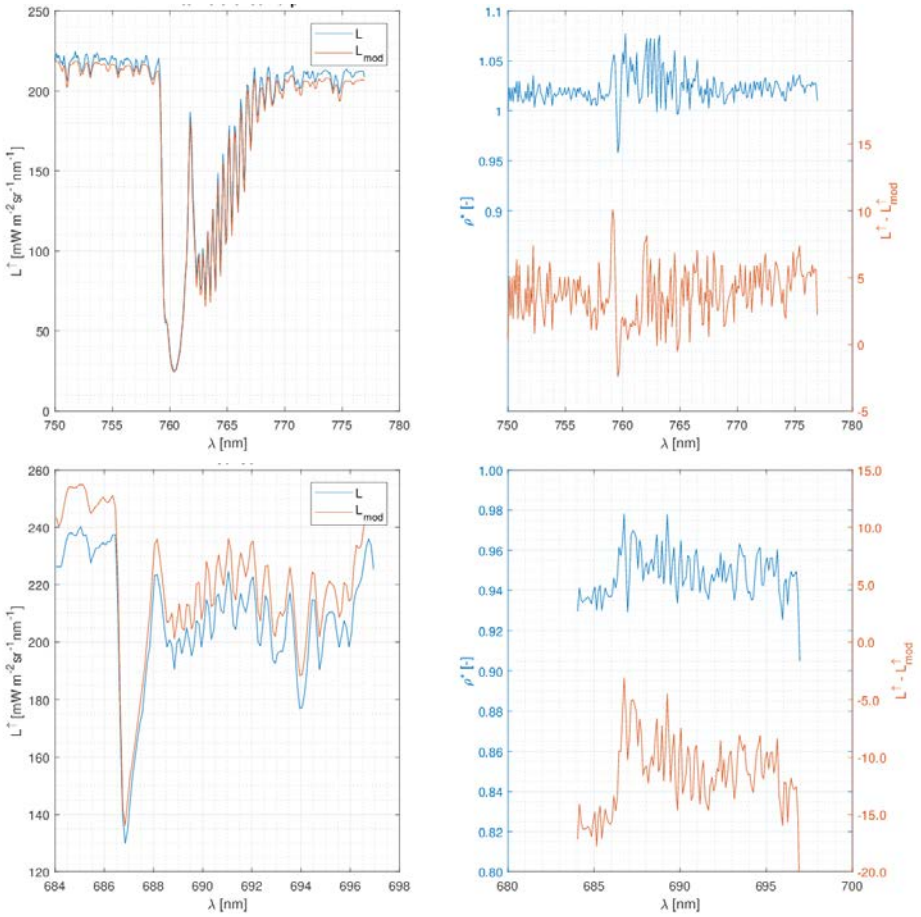

Figure 66: Left: comparison of radiance spectra observed by *HyPlant* (blue line) and MODTRAN simulation (orange line) for the white reference tarp at the O_2-A (top) and O_2-B (bottom). Right: apparent reflectance (blue line) and absolute error in radiance units.

The challenging atmospheric conditions make very difficult to accurately model the atmospheric radiative transfer because input parameters derived by sunphotometer may be not completely representative of the effective illumination conditions at the exact time of the *HyPlant* observations on the experimental fields. Therefore, we implemented an empirical version of the Spectral Fitting retrieval based on reference tarps within the imagery. In particular, the radiance detected on the white and grey reference tarps, corrected by their actual reflectance, were used as reference signal. The processing of the imagery based on this empirical approach was possible for a couple of reasons: i) the soybean fields cover a small area; ii) tarps were located close to the soybean fields and we can assume that the radiance from these panels is more representative of the effective illumination conditions for the soybean fields pixels. The fluorescence maps retrieved are depicted in Figure 67.

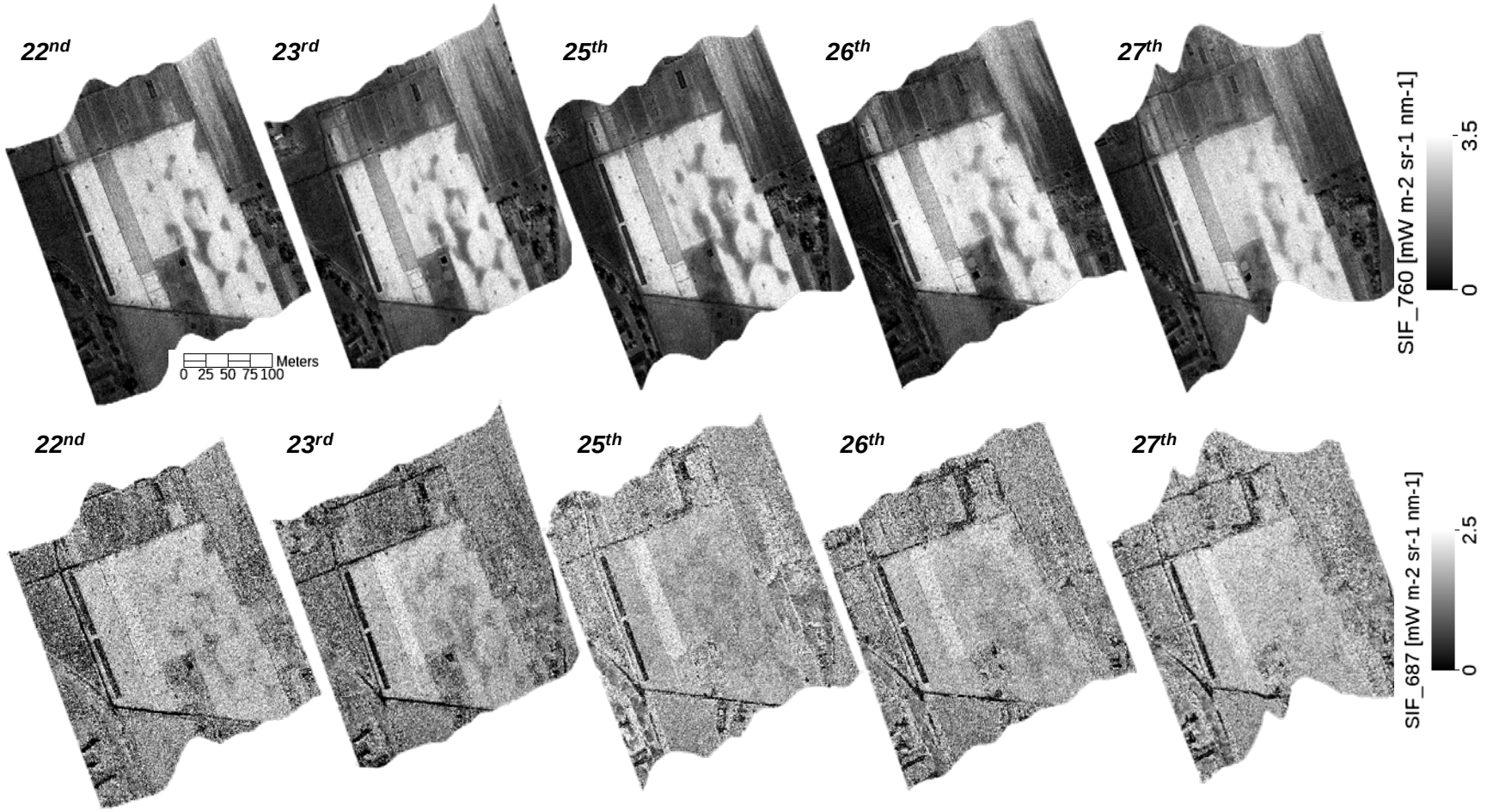

Figure 67: Red and far-red fluorescence maps of MinnGold and Eiko soybean fields retrieved for five different days (July 22nd, 23rd, 25th 26th and 27th) at O_2-A (top, SIF_760) and O_2-B (bottom, SIF_687).

The distributions of red and far-red florescence values retrieved at oxygen absorption bands for the entire imagery subsets (i.e. crops fields and surrounding bare soils) are shown in Figure 68. The fluorescence peaks have slightly different values along the experiment measurement days. The red fluorescence at 687 nm shows unimodal behaviour with the larger number of pixels values in the range between 1-2 mW m^{-2} sr^{-1} nm^{-1}, depending on different measurements days. The non-vegetated pixels have in general lower values that can be negative in some cases, while dense vegetated areas show larger (and positive) values up to 2-2.5 mW m^{-2} sr^{-1} nm^{-1}. Conversely, far-red fluorescence is characterized by a bimodal distribution: the first peak around 1 mW m^{-2} sr^{-1} nm^{-1} mostly represents non-densely vegetated pixels; the second maximum at larger fluorescence values 3-4.5 mW m^{-2} sr^{-1} nm^{-1} represents densely vegetated crops fields (soybean). In general, as already discussed, the retrievals at the O_2-B band show some negative pixels, that can be mostly caused by the overcorrection introduced from the PSF deconvolution algorithm. The red fluorescence does not show a bimodal distribution as far-red fluorescence probably because the larger amount of instrumental noise that it generally increases the deviation of values on a larger range of values.

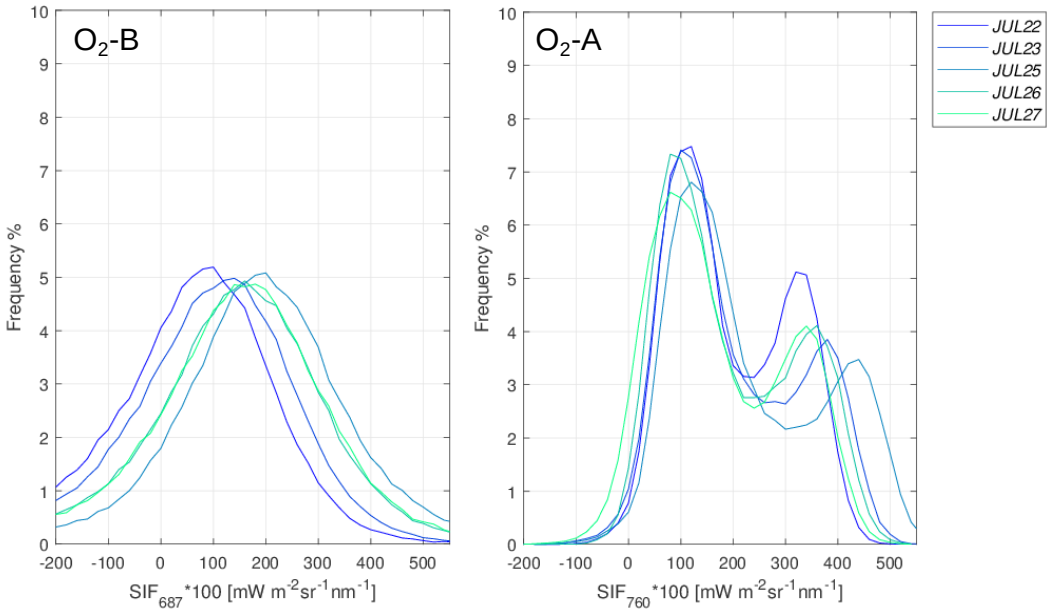

Figure 68: Distribution of fluorescence values for entire imagery subset retrieved for the different days. The left plot shows the fluorescence values at 687 nm; the right plot the fluorescence values at 760 nm. The frequency is normalized for the total number of pixel in the image.

The fluorescence retrieved of the different soybean variety is depicted in Figure 69. The mean values were extracted on “big roi” that cover more than 70% of each soybean field. The first important remark is that relative patterns between MinnGold and Wildtype Eiko are consistent through the diverse days and atmospheric conditions. The MinnGold shows larger red fluorescence values that is related with the lower chlorophyll content as described in the specific sections of the report. On the contrary, far-red fluorescence shows larger values for the Wildtype variety, the different soybean variety are completely separated also considering the standard deviation. The overall dispersion of values within the ROIs is larger for O_2-B band (2 mW m^{-2} sr^{-1} nm^{-1}) than for the O_2-A (< 1 mW m^{-2} sr^{-1} nm^{-1}). These results have not a general meaning because the overall noise in the fluorescence maps products could be also due to the noise in the reference signal used in the retrieval (i.e. radiance spectrum from white reference tarp). In fact, the fluorescence maps retrieved from the complete Spectral Fitting retrieval algorithm that includes atmospheric forward modelling (data not showed), have lower noise and a much better spatial pattern. The overall values seem slightly overestimated and they need to be further analysed, probably

the white reference tarp used as reference is not located at image nadir, therefore the depth of the absorption band is deeper and consequently the fluorescence is overestimated.
This approach has some limitations and it is not suggested as the best approach to be developed for processing *HyPlant* imagery, however it was necessary to process these imageries collected with not optimal and stable atmospheric conditions.

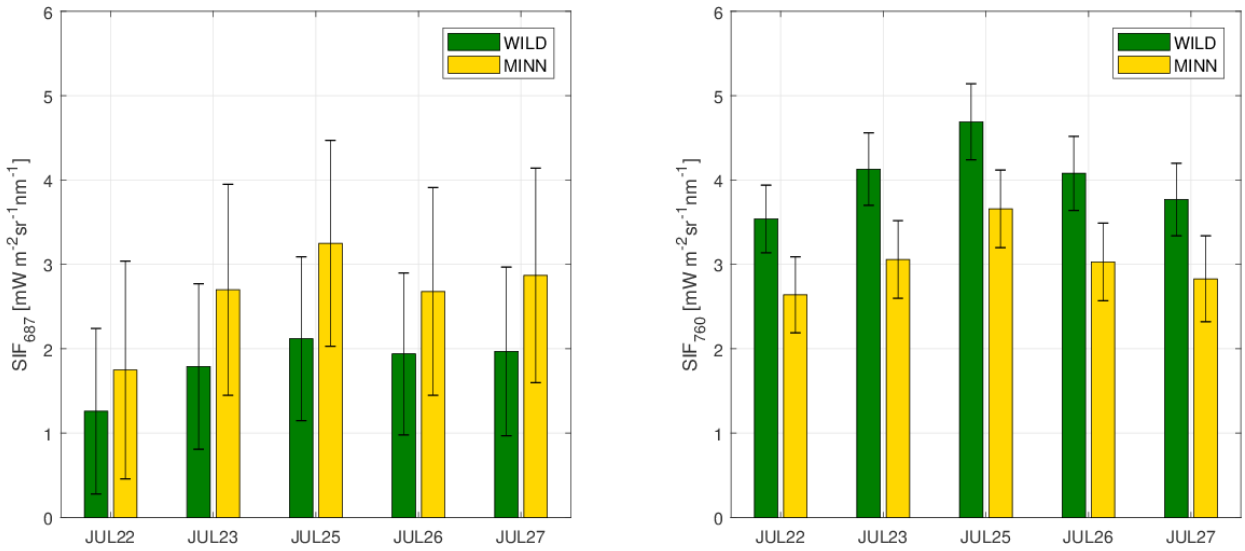

Figure 69: Mean fluorescence values and standard deviation for O_2-B (left) and O_2-A (right),computed over two "big roi" that almost cover the entire MinnGold (yellow) and Eiko (green) soybean fields.

6.2.3 Validation of fluorescence maps from iFLD and Spectral Fitting Method, with the ground reference measurements

The fluorescence maps obtained using the iFLD (Figure 64) and the SFM (Figure 67) retrieval methods were validated using top-of-canopy (TOC) spectral measurements acquired over the two soybean varieties concurrently with the *HyPlant* overflights.
The ground measurements were acquired with the FLOX system (JB Hyperspectral Devices, Düsseldorf, Germany) measuring alternatively the two varieties from a fixed position (FLOX), as well as with the Milano Manual System (MMS) measuring the two varieties from three different positions (M1-M2-M3) (Figure 70). A detailed description of the systems and of the ground measurements' acquisition is provided in section 4.2.2.
For validation purpose, for each plot a set of ground data including the F_{687} and F_{760} measurements in a time window of about ± 30 min around the *HyPlant* overpasses was averaged. These data were compared against the F values extracted from the *HyPlant* images from regions of interest (ROIs) of 10-12 pixels centred on the areas observed with the ground systems.

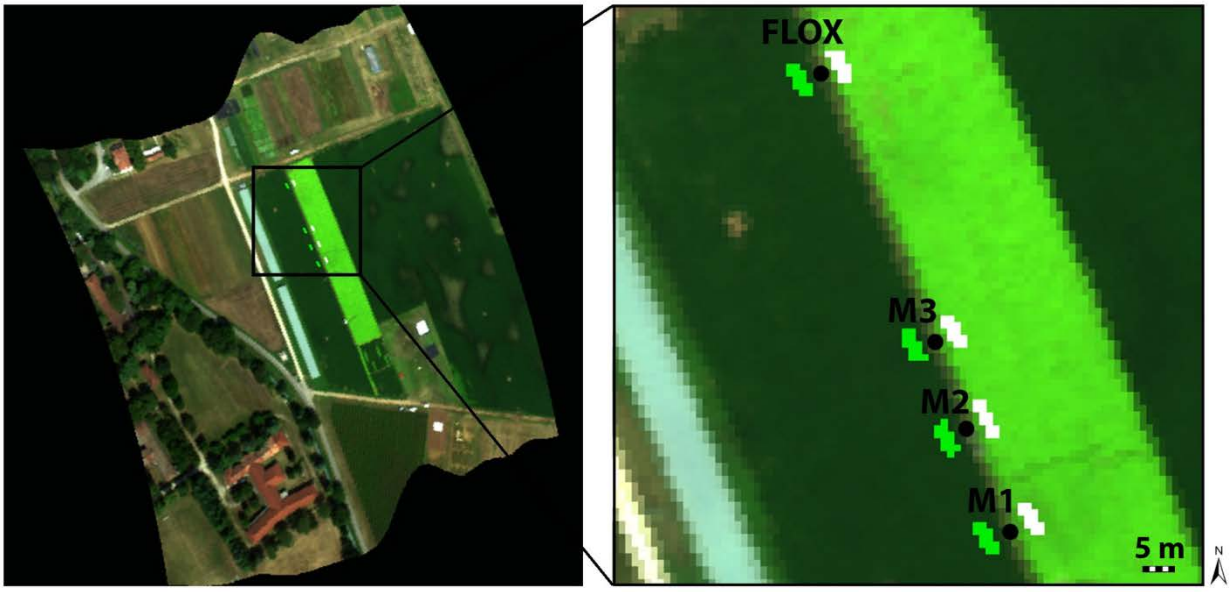

Figure 70: Location of the plots where TOC spectral measurements were performed (M1-M2-M3-FLOX) on *HyPlant* RGB true colour image. For each position the ground measurements were acquired alternatively over the MinnGold and the Wildtype variety Eiko. The regions of interest (ROIs) from which the values were extracted from the *HyPlant* images for validation are marked in white (MinnGold) and green (Eiko).

In the following bar plots (Figure 71), F_{687} and F_{760} retrieved from the TOC spectral measurements (white bars) and from the airborne data using the iFLD method (grey bars) and the SFM (striped bars) in correspondence of the different plots are shown. The comparison between the fluorescence values measured on the ground and retrieved from the airborne data using the iFLD and SFM method show that the general patterns observed in MinnGold and Eiko are maintained: F_{687} shows higher values in the MinnGold compared to the Eiko, while F_{760} values are higher in the Eiko.

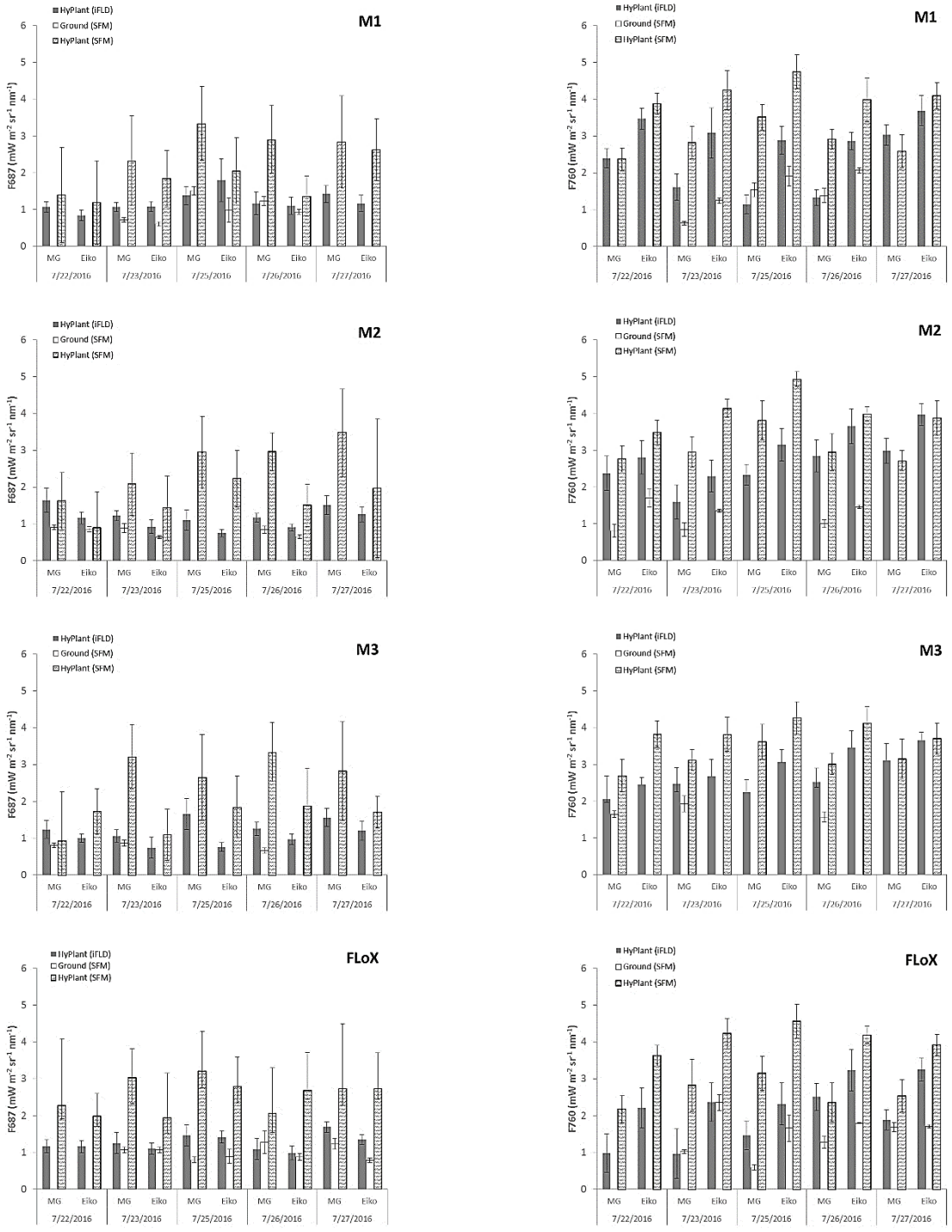

Figure 71: Comparison between F_{687} and F_{760} values retrieved from the TOC measurements acquired with MMS and FLOX (white bars) and from *HyPlant* using the improved Fraunhofer Line Discrimination (iFLD) and Spectral Fitting Method (SFM) over the two soybean varieties (MG=MinnGold, Eiko) on all the measurement dates. For each ground measurement position (M1-M2-M3-FLOX), one plot for F_{687} and one plot for F_{760} are showed.

The scatterplot of red (Figure 72) and far-red (Figure 73) fluorescence show the comparison of the ground measurements and *HyPlant* fluorescence maps calculated with the iFLD and the SFM. Each point of the scatterplots present the averaged value± standard deviation of one ground measurement point and the corresponding roi of 10-12 pixels (Figure 70). All available data of the five different measurements days were included in the comparison. The relationship between ground and airborne

measurements is very poor for both, red and far-red, fluorescence and both retrieval methods. The systematic overestimation for both red and far-red fluorescence, could be related to the different distance to the canopy surface by ground (1-2 meters) and airborne (570 meters). While the differences between both methods, SFM and iFLD, are driven by the different non-vegetation reference targets used. The iFLD method uses all across track soil pixels which are available in the complete flight line, while the SFM uses the white reference tarp for an empirical correction. The very high day to day variation of the fluorescence values, are related to the fact that, on none of the five measurement days we had stable atmospheric conditions (Figure 26).

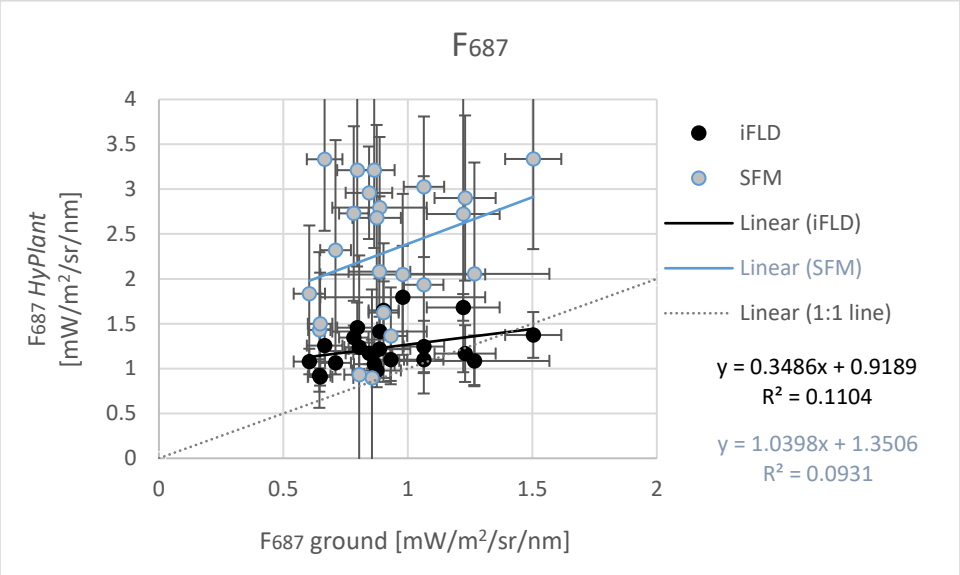

Figure 72: Relation between red fluorescence measurements collected over the SoyFLEX2 experiment on five different days in 2016. Fluorescence values were retrieved from airborne data using the iFLD and SFM and present an average ± standard deviation of 10-12 pixels per ground measurement position (M1-M2-M3-FLOX).

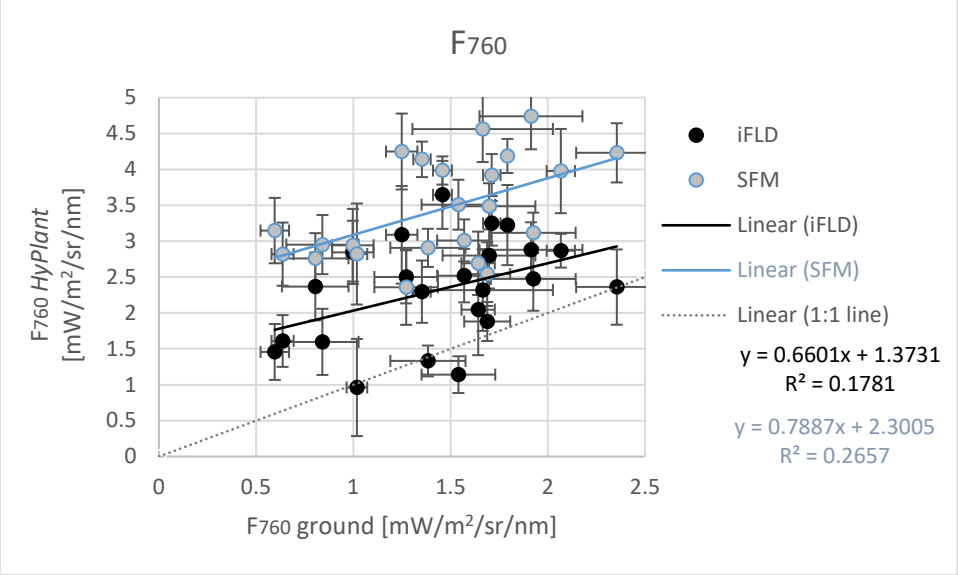

Figure 73: Relation between far-red fluorescence measurements collected over the SoyFLEX2 experiment on five different days in 2016. Fluorescence values were retrieved from airborne data using the iFLD and SFM and present an average ± standard deviation of 10-12 pixels per ground measurement position (M1-M2-M3-FLOX).

6.3 The SoyFLEX2 experiment

The SoyFLEX2 experiment made in the spring/summer 2016 was a repetition of an experiment that already took place during the 2015 Campaign in Germany. In this experiment the Chl-deficient MinnGold soybean line (Campbell *et al.* 2015) was compared with a commercially available cultivar in Europe, Eiko. The two varieties were sown in two non-replicated 1 ha plots at the experimental farm of the University of Udine at a density of 40 plants m^{-2} (Figure 37). The plots were fertilized before sowing and were fully irrigated throughout the growing season from April to September 2016. Meteorological data were collected by an automated weather station at hourly intervals. The two soybean experimental fields (MinnGold and Eiko) were equipped with two four bands net radiometers (CNR-1, Kipp & Zonen, Delft, the Netherlands) to monitor (at 1 Hz scan frequency) the surface energy balance (Rn - net radiation) between incoming shortwave and longwave radiation versus surface-reflected shortwave and outgoing longwave radiation of the fully developed canopies. Data were averaged over 1 minute (chapter 0). Canopy transpiration was measured by means of heat-balance sap-flow gauges (Peressotti & Ham, 1996). With this method, heat is applied to the entire circumference of the stem encircled by a heating tape and the mass flow of sap is obtained by the balance of the fluxes of heat into and out of the heated section of the stem (Sakuratani, 1981). Ten gauges were installed on an equivalent number of plants of each accession and the fluxes were calculated at half-hour intervals from July 22nd to August 8th to obtain reliable estimations of the amount of water transpired by both accessions.

The amount of biomass produced by MinnGold and Eiko canopies was quantified at the end of the canopy CO_2 exchange measurements in 2016 (July 27th) by harvesting all the plants (R5 growth stage) within each chamber collar. Leaves, stems, pods, and roots of each plant were separated manually and then dried at 60°C for 48 hours to determine biomass allocation to individual organs. Leaf area per collar (LA in m^2) was measured by means of a LI-3000C Portable Leaf Area Meter (LI-COR Inc., Lincoln, NE, USA) and leaf area index (LAI; m^2 m^{-2}) was calculated by dividing LA by the collar surface area (Figure 87). All statistical analysis were performed in SigmaPlot 11 (©Systat Software, Inc, San Jose, USA) and in STATA 10.1 (© StataCorp, College Station, TX, USA).

6.3.1 Motivation of the SoyFLEX2 experiment

Chlorophyll-deficient mutants are rather common in plants (Highkin, 1950; Gengenbach *et al.*, 1970; Specht *et al.*, 1975; Li *et al.*, 2013). Mutations leading to 100% albino plants are fatal, while other types of mutations that simply reduce the amount of chlorophylls (Chl) (Daloso et al., 2014) lead to plants that can successfully complete their lifecycle. These plants have been repeatedly used to investigate how carbon uptake in leaves scales with the Chl-content (Benedict *et al*., 1972), and comparable (Benedict *et al.*, 1972) or higher photosynthetic capacities (Li *et al.*, 2013; Slattery *et al.*, 2017) of Chl-deficient versus green leaves of different species have been observed. The most obvious interpretation of such an effect is that reduced Chl-content facilitates a more even distribution of light in the mesophyll (Vogelmann *et al.*, 1996; Vogelmann & Evans, 2002), which attenuates photoprotection (non-photochemical quenching - NPQ) and thus leads to an increase in the photochemical efficiency of photosystem II (ΦPSII) (Li *et al.*, 2013). As a consequence, more carbon dioxide (CO_2) can be fixed per absorbed photon and per unit of leaf area, so that the same photosynthetic rates can be maintained in spite of increased light reflectance/transmission (Ort & Melis, 2011). The idea that canopies of Chl-deficient plants can attain photosynthetic rates higher than those of the most common “green” cultivars has been thoroughly discussed (Drewry *et al*., 2014). When Chl-deficient crops are grown in the field and reach full canopy cover, they are not only expected to distribute light more uniformly across the leaf, but also across the whole canopy. Due to a higher light transmittance of the upper canopy layers, plants with lower Chl-content should enable more photons to reach the lower layers of the canopy, so that the total photosynthetic light absorption in the canopy space would compensate reduced light absorption of individual leaves (Long *et al.*, 2006). The use of Chl-deficient crops is expected to have an effect on the surface energy balance. Reduced Chl-content leads to an increase in reflectance and transmittance particularly in the region of the spectrum outside the Chl absorption peaks. This may increase the overall surface shortwave albedo, which is currently considered an effective bio-geophysical strategy to mitigate the increasing atmospheric radiative forcing (Bright et al., 2016) and potentially leading to significant water savings (Drewry *et al.*, 2014; Zamft & Conrado, 2015).

The main objectives of the SoyFLEX2 experiment are to:

- Corroborate the results presented at leaf in the Final Report from 2015 [RD-4] and add meaningful and reliable results for different canopy measurements.

- Show with a simple forward model how leaf chlorophyll content, canopy architecture and photosynthetic efficiency affect sun-induced fluorescence and reflectance based vegetation measurements. Therefore, SCOPE was used to demonstrate that the lower red fluorescence values in Eiko compared to MinnGold is due to higher re-absorption across the canopy in the Wildtype (Eiko) compared to the chlorophyll deficient variety (MinnGold) (Figure 74).

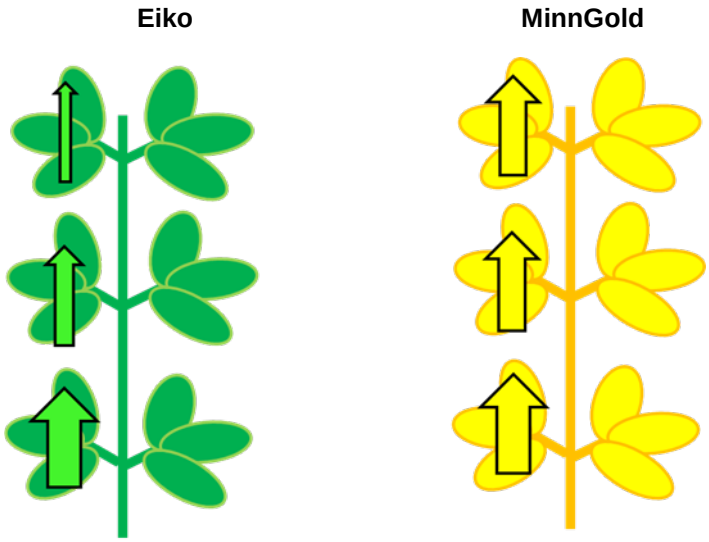

Figure 74: Scheme representing the higher re-absorption across the canopy in Eiko (left) compared to MinnGold (right).

6.3.2 Gas exchange chamber measurements on the canopy level

Gas exchange chamber measurements were carried out in the period started from 21st of July (DAY1) and were finished on 27th of July (DAY7) according to the measurement protocol given in chapter 4.2.7. As presented in Table 29 equal number of *NEE* and *Reco* measurements was taken each day and varied from 11 to 16, while number of *Rh* measurements was usually half of *Reco* (6-8), both on Eiko and Minngold sites. Total number of *NEE*, *Reco* and *Rh* measured within the whole period between 21-27th of July 2016 equalled respectively 68, 67, 34 and 66, 66, 35 for Eiko and Minngold, respectively (Table 14). Considering above, the total number of *GPP* fluxes calculated based on consecutive *NEE* and *Reco* fluxes measurements equals 68 for Eiko and 66 for Minngold. While total number of autotrophic respiration (*Ra*) calculated from measured *Reco* and *Rh* equalled 34 and 35 for Eiko and Minngold, respectively.

Table 29: Overview of the canopy gas exchange chamber measurements during the SoyFLEX2 campaign

Date	Time Start/end	PAR (umol m^{-2} s^{-1}) /air temperature (^oC) range	No. of NEE fluxes	No. of Reco fluxes	No. of Rh fluxes	No. of NEE fluxes	No. of Reco fluxes	No. of Rh fluxes	Total number of fluxes measured
			Eiko			Minngold			
21.07.16	7:17 16:47	450-2450 22.1-30.3	16	16	8	16	16	8	80
22.07.16	7:20 15:50	830-2045 23.7-303	16	16	8	16	16	8	80
23.07.16	8:20 16:00	350-2400 25.8-35.2	12	12	8	12	12	7	63
24.07.16	No measurements								
25.07.16	7:25 12:50	540-2200 22.0-30.3	11	10	6	12	12	6	57
26.07.16	8:20 14:30	790-2260 27.9-32.4	11	11	6	10	10	6	54
27.07.16	7:40 14:30	730-2260 24.8-32.8	14	14	6	12	12	7	64
		Total number	**68**	**67**	**34**	**66**	**66**	**35**	**335**

The meteorological conditions during the chamber measurements are presented in Figure 75 and Figure 76. No rain occurred during this period, while the site was irrigated at DAY5 (25th of July) in the late afternoon and over the night.
Measurements were carried out between 7 am and 4 pm at air temperatures varied from 22.0 to 35.2 ^oC and PAR values between 350 and 2400 µmol m^{-2} s^{-1}. Weather conditions were not very stable over the day (besides DAY1 and DAY2) and in the afternoon hours PAR values were often reduced due to appearing clouds. Measurements at DAY5 were shorter and finished close to 1pm due to the scheduled irrigation.

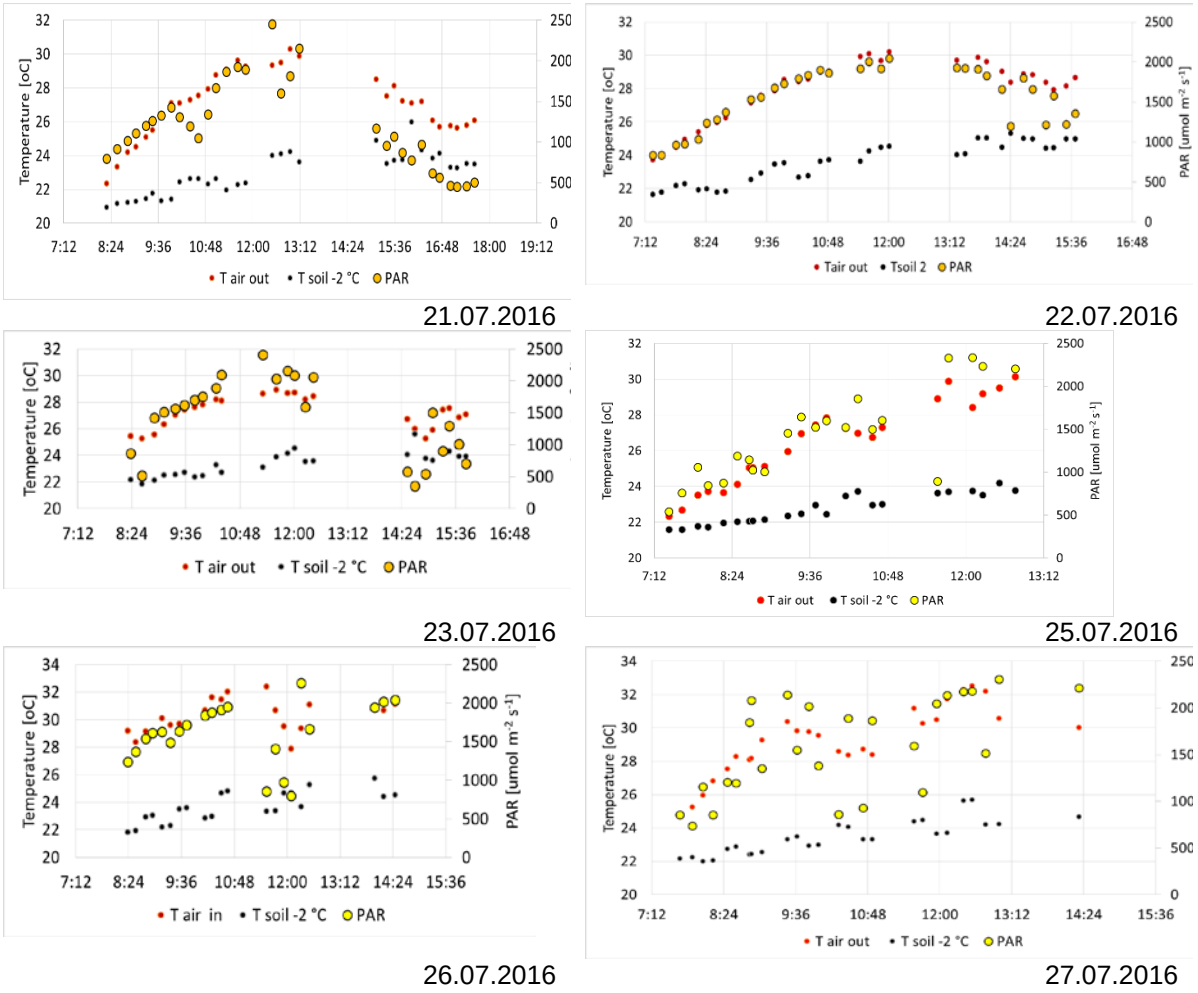

Figure 75: Weather conditions at the time of chamber measurements for the period between 21st and 27th of July 2016. Each set of dots for certain time refers to the single chamber measurement. Yellow dots refer to PAR (µmol m^{-2} s^{-1}), red to air temperature (ºC) in the chamber headspace and black to soil temperature (ºC) at 2 cm depth.

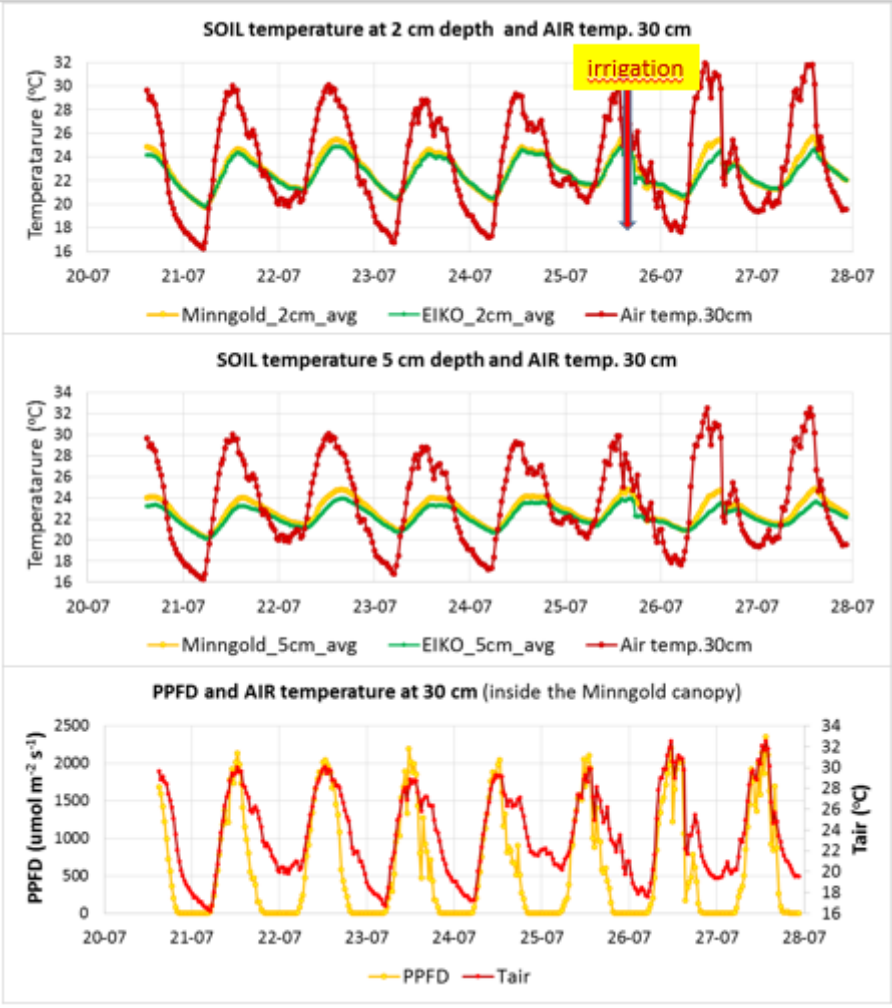

Figure 76: Inside canopy air temperature (ºC) at 30 cm, soil temperature (ºC) at 2 and 5 cm depths and PPFD (µmol m^{-2} s^{-1}) measured in the middle of the site in between E1-E3 & M1-3 and E4-E6 & M4-M6 plots at the mini weather station installed for the purpose of the chamber team.

Average NEE and Reco fluxes were different at each day for Eiko and Minngold canopies (Figure 77). NEE fluxes were increasing (fluxes were more negative) for the first 3 days at Minngold plots and were nearly the same for the next 3 days of the campaign. In contrast, NEE fluxes on Eiko sites were the same for the first 3 days and increased in the last 3 days of the campaign. There was no significant difference between NEE fluxes of all the plots (M1-M2, M4-M5 and E1-E2, E4-E5) if all dataset was considered, although Eiko NEE fluxes were higher at DAY1, 6 and 7 and lower ad DAY 3 and DAY 5 in relation to Minngold NEE.

Reco fluxes were significantly higher on Eiko plots at the first 3 days of measurements and lower at the last day in relation to Minngold Reco. At DAY 5 and DAY 6 Reco fluxes were the same at both varieties. There was significant difference between Reco fluxes measured at north and south part of the field, and generally Reco measured on plots M4-M5 and E4-E5 was higher than on M1-2 and E1-E2, which reflects heterogeneity of the soil in the field.

If the complete dataset is considered, no significant difference in Reco fluxes between two varieties can be detected (Figure 78). This is also presented in the NEE data. When all Eiko and Minngold plots is considered (for the whole period), than there is no significant difference between the NEE fluxes of both variates and NEE vs PAR light response curves are overlapping (Figure 78).

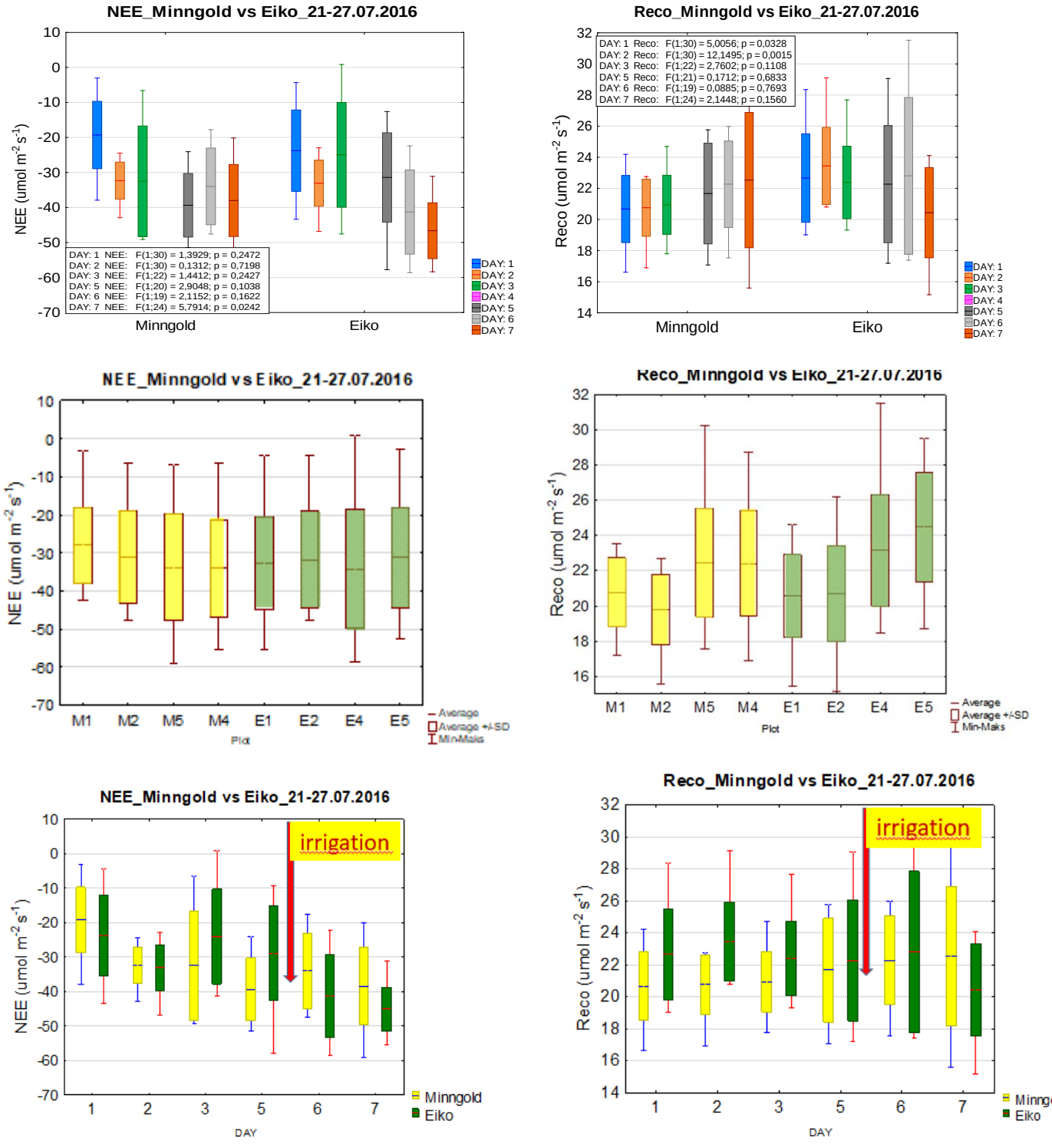

Figure 77: *NEE* and *Reco* fluxes measured on Eiko and Minngold plots for the period from 21st to 27th of July 2016.

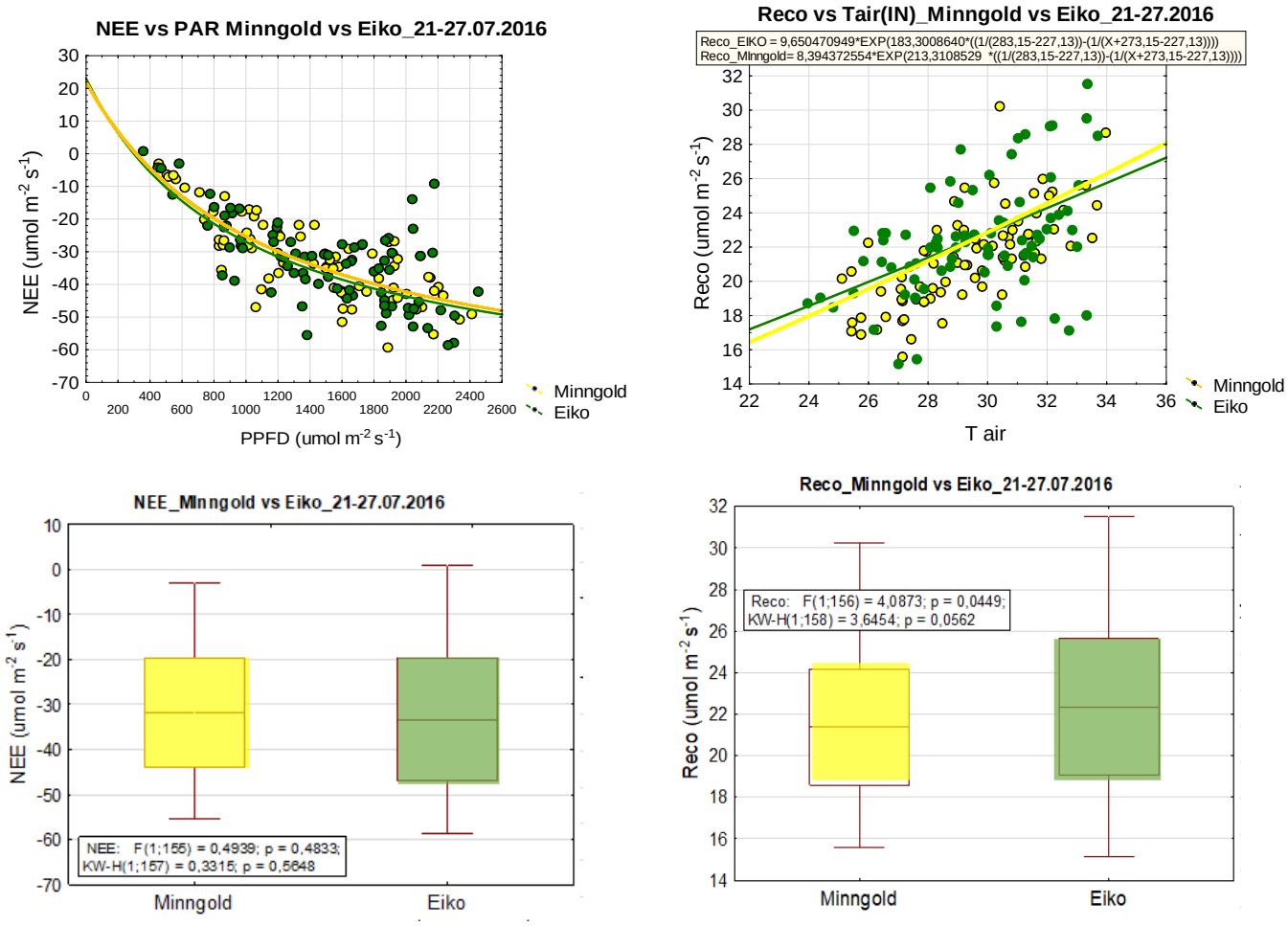

Figure 78: Net Ecosystem Exchange (*NEE*) and Ecosystem respiration (*Reco*) fluxes plotted against photosynthetic photon flux density (PPFD) and air temperature (Tair) respectively. Boxplot of NEE and Reco for the two different varieties Eiko and MinnGold considering all the complete dataset acquired in the period from 21st to 27th of July 2016.

Heterotrophic respiration (Rh) of Eiko plots was significantly higher for the whole period and each day of the campaign (Figure 79). Although Rh fluxes at Minngold sites were at the same level for DAY1 to DAY5, Rh at Eiko plots was gradually decreasing in this time. Rh fluxes on both variates decreased nearly three times after irrigation, but still the fluxes were significantly higher on Eiko plots than on Minngold. The calculated autotrophic respiration (Ra) fluxes were not different for the first 5 days of the campaign for both varieties and significantly increased at day 6 and 7 after irrigation. Although Rh on Eiko plots was significantly different ($p<0.0000$) than on Minngold, the Ra fluxes are the same for both varieties (Figure 80). Contribution of Ra to Reco was equal to 77% and 71% in MinnGold and in Eiko, respectively.

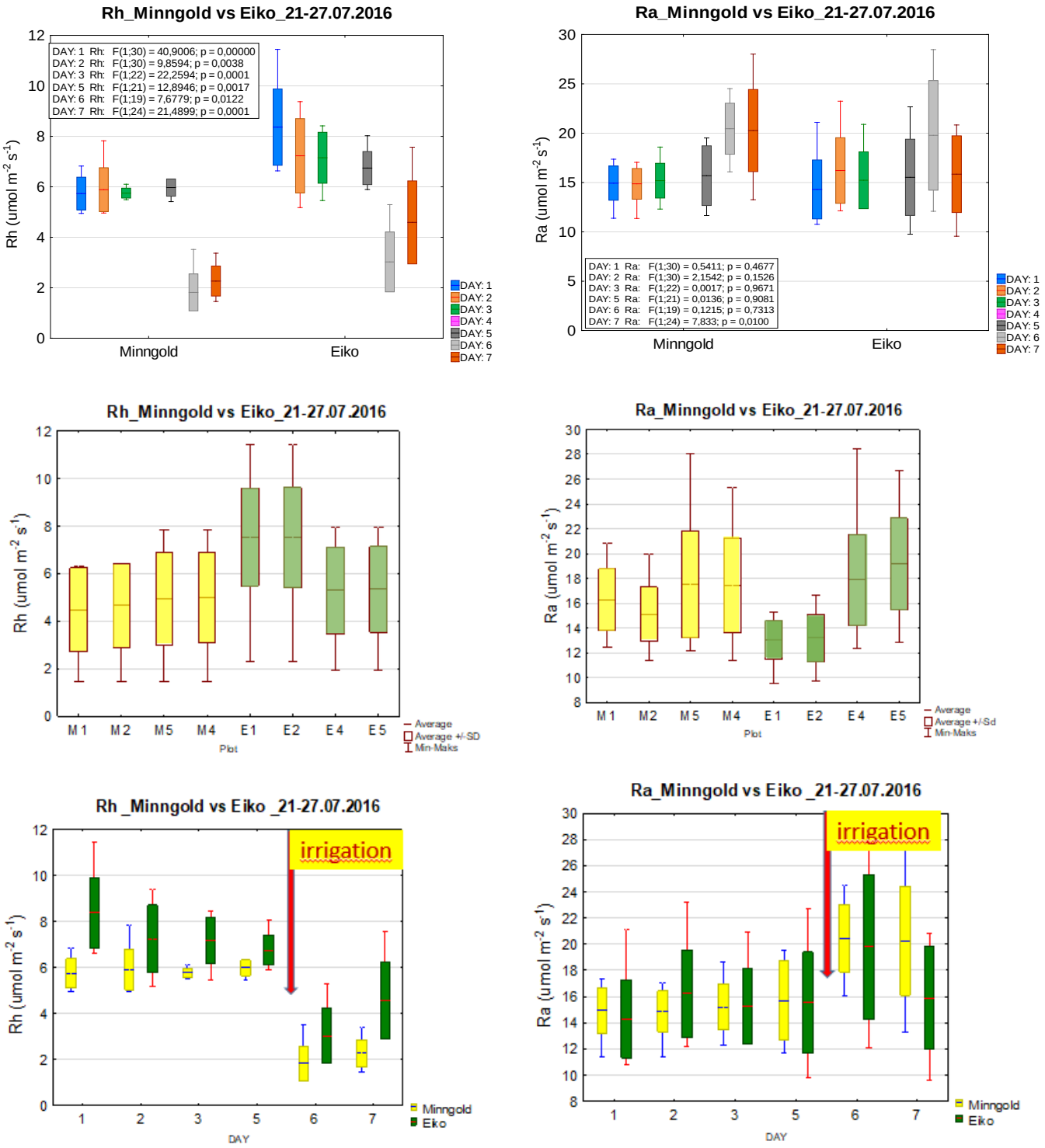

Figure 79: Measured heterotrophic respiration (*Rh*) and calculated autotrophic respiration (*Ra*) fluxes for Eiko and Minngold plots for the period from 21st to 27th of July 2016.

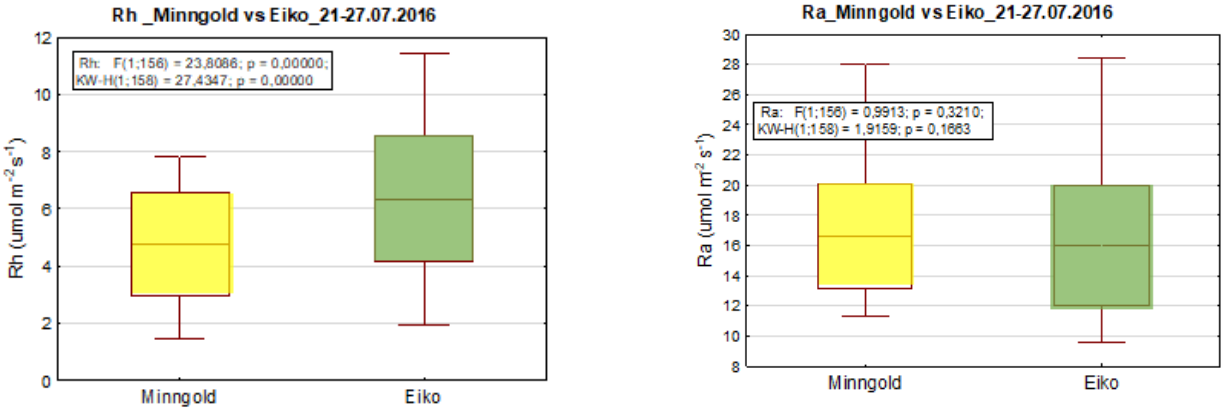

Figure 80: Boxplot of the measured heterotrophic respiration (*Rh*) and calculated autotrophic respiration (*Ra*) fluxes for Eiko and Minngold considering all the complete dataset acquired in the period from 21st to 27th of July 2016.

GPP calculated based on the consecutive *NEE* and *Reco* measurements was higher (average fluxes were more negative) at the first 2 and the last 2 days (after irrigation) of the campaign and lower on DAY3 and 5 for Eiko plots than on Minngold (Figure 81). However it must be noted that all these differences were not statistically significant. Decreasing GPP fluxes on Eiko plots may indicate that Eiko plants suffer due to drought stress. Signs of drought stress were visible on the Eiko leaves.

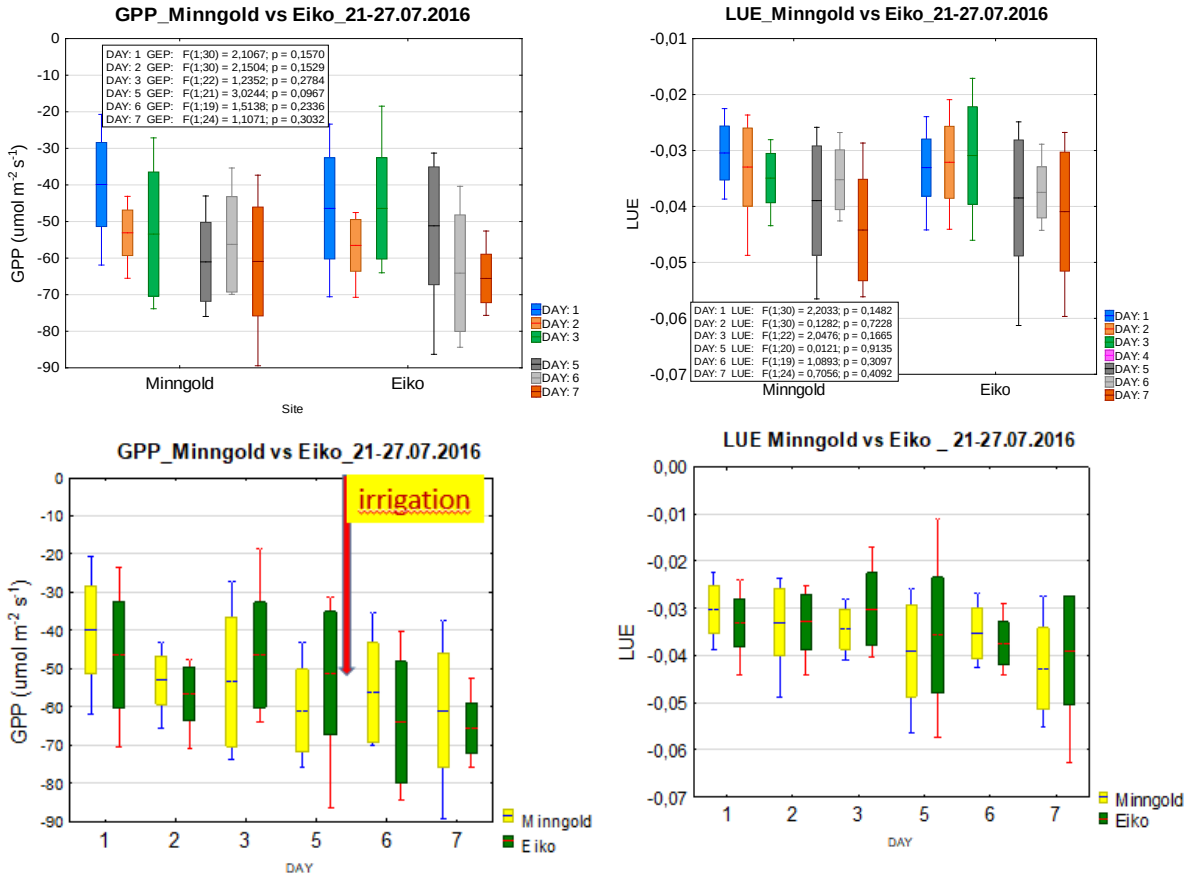

Figure 81: *GPP* calculated based on the consecutive *NEE* and *Reco* measurements for Eiko and Minngold plots for the period from 21st to 27th of July 2016

However, when the whole dataset for the whole campaign is considered there is no significant difference in GPP fluxes between Eiko and Minngold varieties. The light response curves for Eiko and Minngold plots are overlapping when GPP fluxes are referred to calculated APAR (Figure 82).

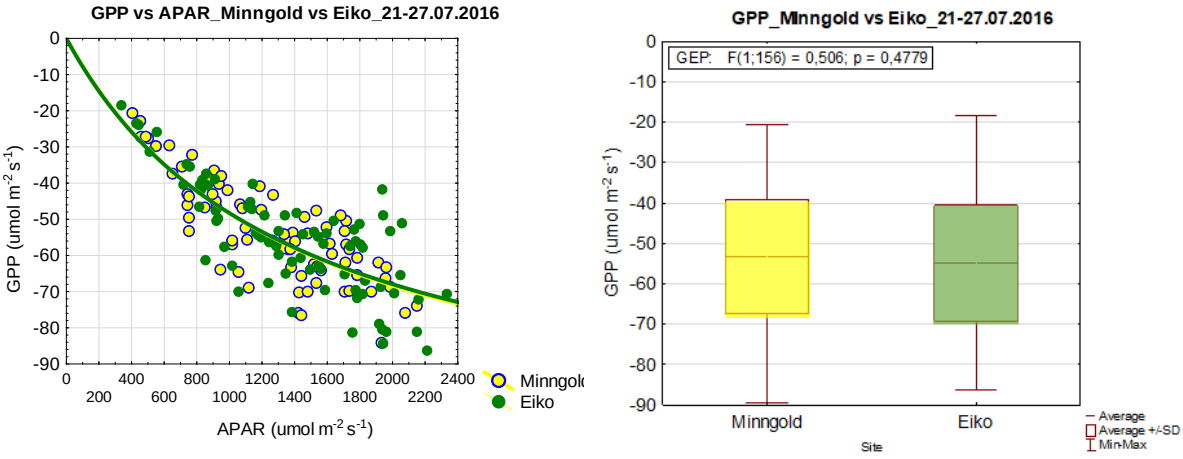

Figure 82: *GPP* plotted versus APAR (left); Boxplots of the two different varieties Eiko and Minngold considering the complete dataset acquired in the period from 21st to 27th of July 2016.

6.3.3 Chlorophyll content and canopy structure

6.3.3.1 Chlorophyll content at leaf level

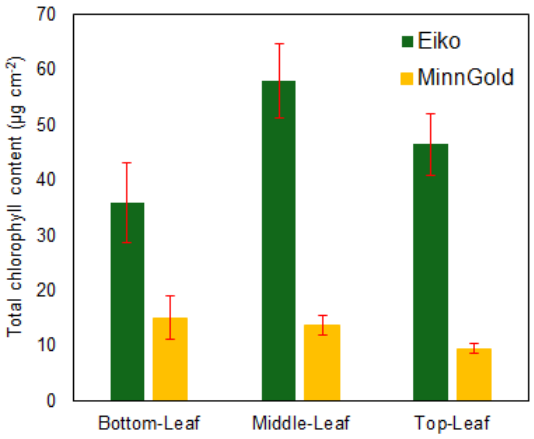

Figure 83: Total chlorophyll content in µg/cm2 from top, middle and bottom derived from destructive chlorophyll measurements. The values are averages from 6 samples, error bars represent standard deviation.

The total chlorophyll content (Chlorophyll a+b) is significantly higher in Eiko, than in the chlorophyll deficient MinnGold type (Figure 83).

6.3.3.2 Fraction of absorbed photosynthetic active radiation at canopy level

Fraction of absorbed photosynthetic active radiation at canopy level ($FAPAR_{canopy}$) were conducted on July 22nd and 23rd with the SunScan instrument (chapter 4.2.6). The $FAPAR_{canopy}$ of the Eiko soybean accession was approximately 7% higher than the $FAPAR_{canopy}$ of the Minngold chlorophyll deficient mutant (p value <0.001, Mann-Whitney-Wilcoxon test; Figure 84).

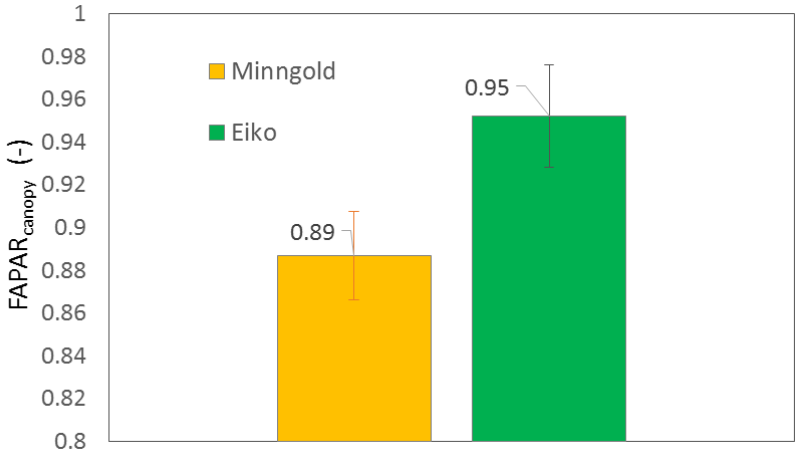

Figure 84: Fraction of absorbed photosynthetically active radiation ($FAPAR_{canopy}$) measured on the 22nd of July 2016 in the two investigated soybean accession fields. The values are averages of 24 measurements taken in six randomly chosen field locations. Error bars represent standard deviation. The values of absorbed photosynthetically active radiation (APAR) corresponding to the *HyPlant* overpass taking place on the same day at 12:03 of local time was equal to 1567 µmol m^{-2} s^{-1} and 1682 µmol m^{-2} s^{-1} for Minngold and Eiko canopies, respectively.

The $FAPAR_{canopy}$ measurements conducted at different time of the day revealed no variability in $FAPAR_{canopy}$ during the measurement time window for both Minngold and Eiko canopies (p value of 0.41 and 0.50 for Minngold and Eiko, respectively; ANOVA; Figure 85). The main reason for such a stable

$FAPAR_{canopy}$ values is the fact that the measurements were performed under conditions of almost full canopy closure.

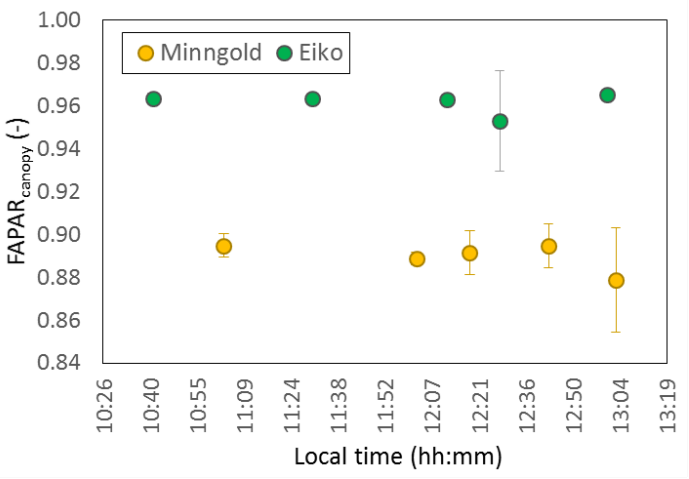

Figure 85: Diurnal courses of fraction of absorbed photosynthetically active radiation ($FAPAR_{canopy}$) measured on the 23rd of July 2016 in the footprint of the FLOX fluorescence system. The values are averages of 4 measurements and error bars represent standard deviation.

The Mann-Whitney-Wilcoxon test results used to compare the transmittance vertical profiles of Minngold and Eiko canopies indicated that (at 0.01 significance level) the distribution of PAR at different canopy layers was identical in the Minngold and Eiko canopies (p values of 1.0, 0.686, 0.029, 0.114 and 0.057 for T_4/PAR_C, T_3/PAR_C, T_3/PAR_C, T_1/PAR_C, T_C/PAR_C respectively; Figure 86).

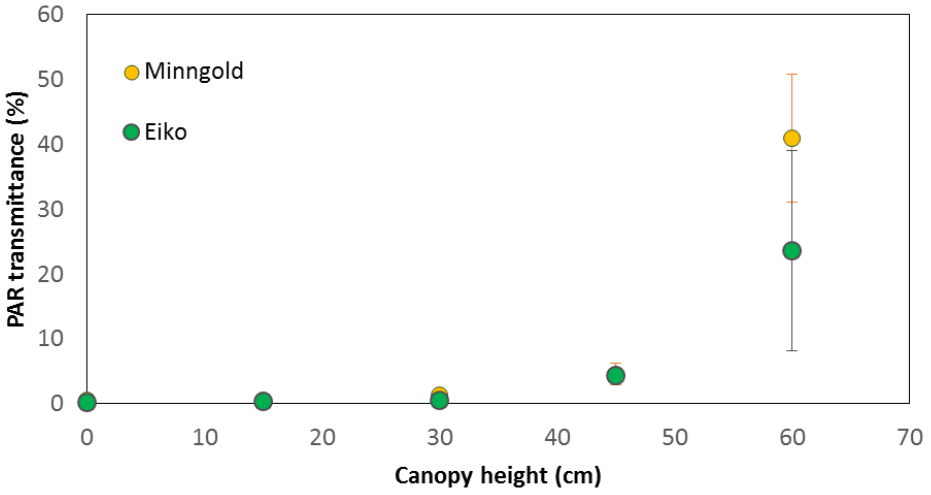

Figure 86: Vertical profiles of photosynthetically active radiation (PAR) transmittance (calculated as a ratio between transmitted PAR measured at different canopy heights and the PAR incident at the top of the canopy (PARC)) for MinnGold and Eiko soybean canopies. The values are averages of 4 measurements performed on the 22nd of July 2016, error bars represent standard deviation.

6.3.3.3 Vertical profile of the leaf area index

The vertical profile of the Leaf Area Index of both MinnGold and Eiko varieties is shown in Figure 87. Five different canopy layer were identified from top of the canopy (0 cm) to bottom of the canopy (>80

cm).These are: layer 1 (0-20 cm), layer 2 (20-40 cm), layer 3 (40-60 cm), layer 4 (60-80 cm), and layer 5 (>80 cm). Similar results can be observed between MinnGold and Eiko in layer 1, 2, and 4. Interestingly in layer 3 MinnGold present a 10% higher LAI than Eiko. Additionally, in contrast to Eiko, MinnGold does not present any leaf at the bottom layer (>80 cm).

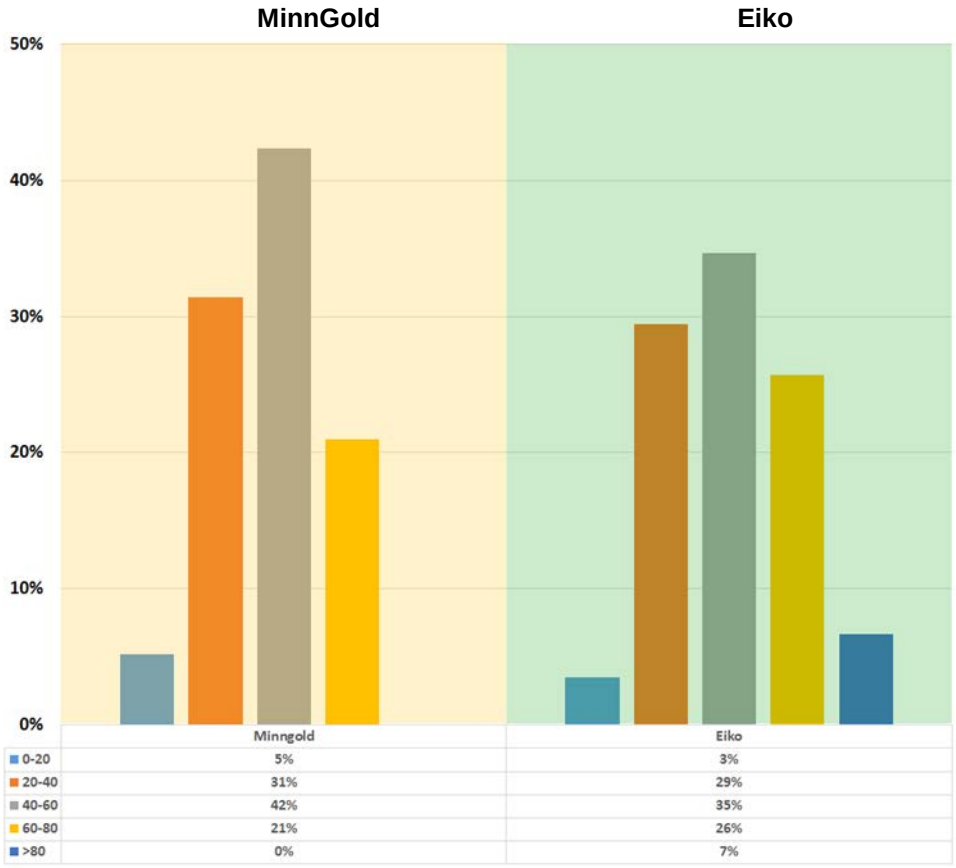

Figure 87: Vertical profile of the Leaf Area Index (LAI) or MinnGold (left) and Eiko (right) varieties.

6.3.4 Leaf-level FluoWat measurements

In order to measure Fluorescence at different canopy layers (top, middle and bottom) two types of artificial LED light sources characterized by different emission spectra were used: 1) LED1 – producing white light and 2) LED2 – producing solely blue peak. Figure 88 - Figure 91 show the fluorescence and fluorescence yield measured when using the WHITE LED light and Figure 92 - Figure 96 the fluorescence and fluorescence yield measured when using the BLUE LED light. From data acquired with the WHITE and BLUE-LED light source it can be concluded that fluorescence at bottom leaves is higher than middle and top leaves (Figure 88 to Figure 95). One reason for this higher fluorescence values could be the sudden exposure of shade adapted leaves in the lower part of the canopy to light. Although we let the leaves adapt to the new light conditions (i.e. lamp) for five minutes before measuring, we might have still capture a Kautsky effect in our measurements. When using the artificial WHITE-LED we observed an in-filling in the fluorescence spectrum, which shows as a large off-set of the fluorescence emission from zero (Figure 88 - Figure 91). Taking into account that the WHITE-LED lamps intensity was smaller than the sun light intensity (i.e. maximum WHITE-LED PAR = 13 W/m^2/sr/nm vs approximately sun-light PAR = 1500 W/m^2/sr/nm) the reason for such an in-filling might be caused by the contaminated our measurements set up by sun-light.
Additionally, when comparing the BLUE led versus WHITE upwelling fluorescence spectrum for both Eiko (Figure 88 and Figure 92) and MinnGold (Figure 89 and Figure 93) varieties we can observe how the fluorescence spectrum shape change when using a WHITE or BLUE LED light source. It is, when using a BLUE LED light the ratio between the red and far-red fluorescence peaks decreases.

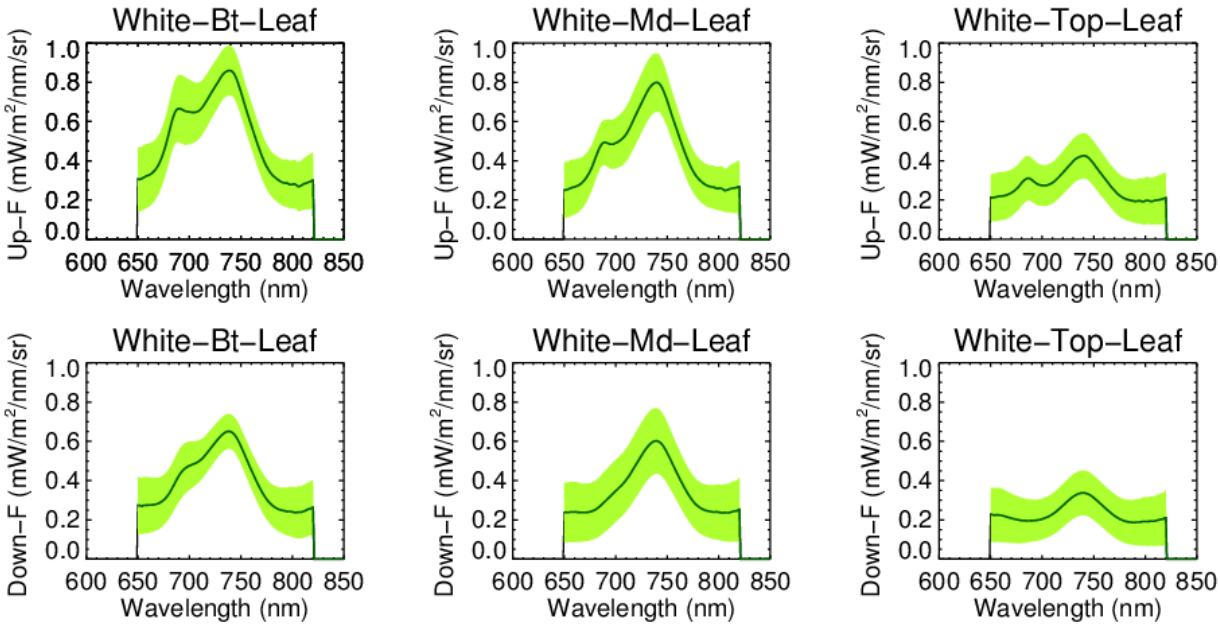

Figure 88: Eiko: Contribution of the upwelling (top) and downwelling (bottom) fluorescence leaves illuminated by WHITE-LED.

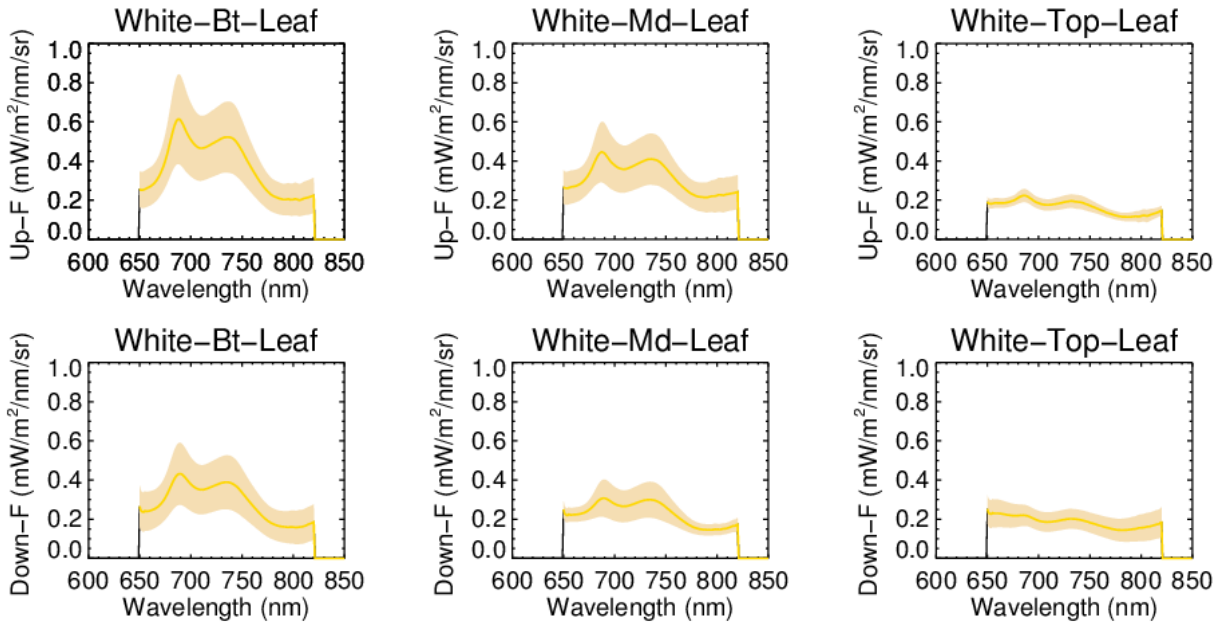

Figure 89: Minngold: Contribution of the upwelling (top) and downwelling (bottom) fluorescence leaves illuminated by WHITE-LED.

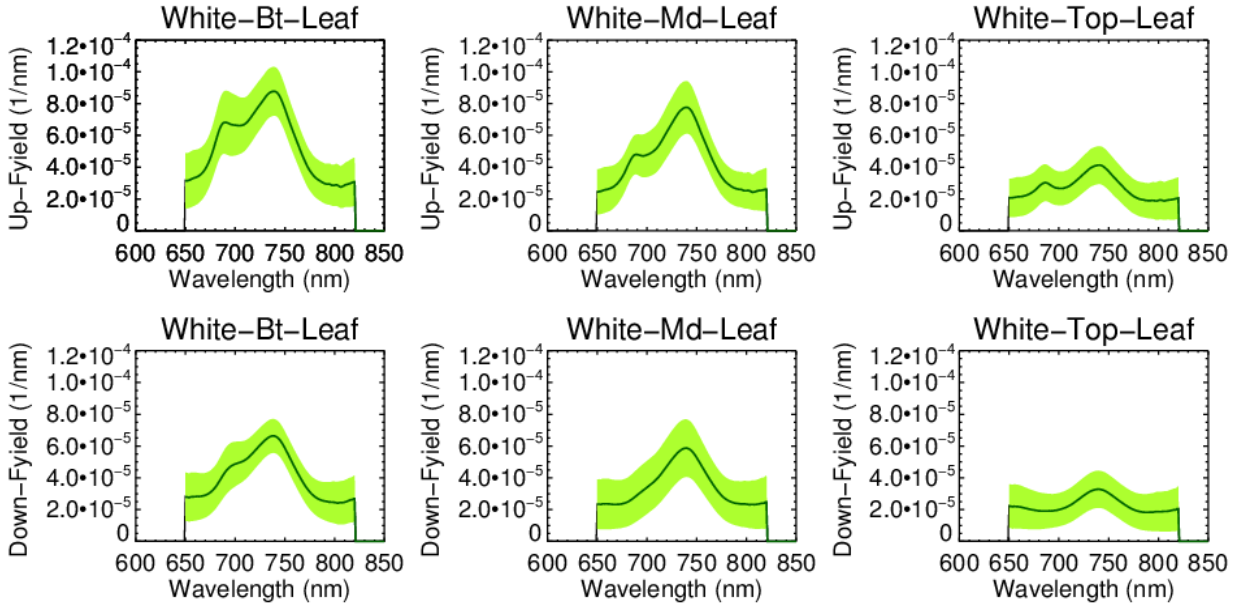

Figure 90: Eiko: Contribution of the upwelling (top) and downwelling (bottom) fluorescence yield leaves illuminated by WHITE-LED.

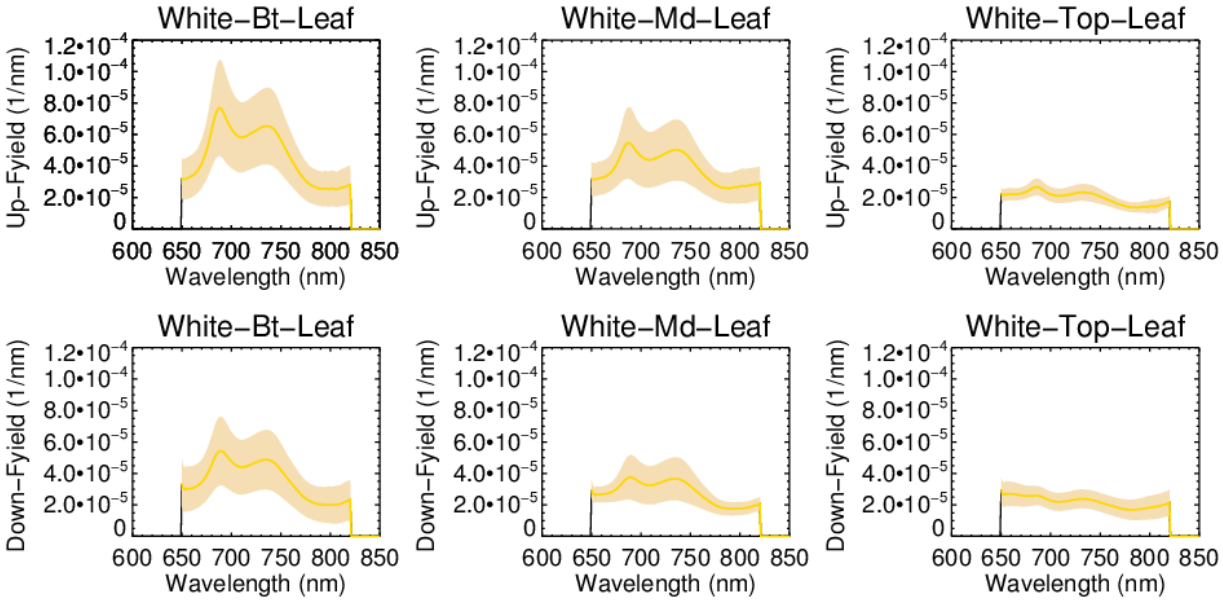

Figure 91: Minngold: Contribution of the upwelling (top) and downwelling (bottom) fluorescence yield leaves illuminated by WHITE-LED.

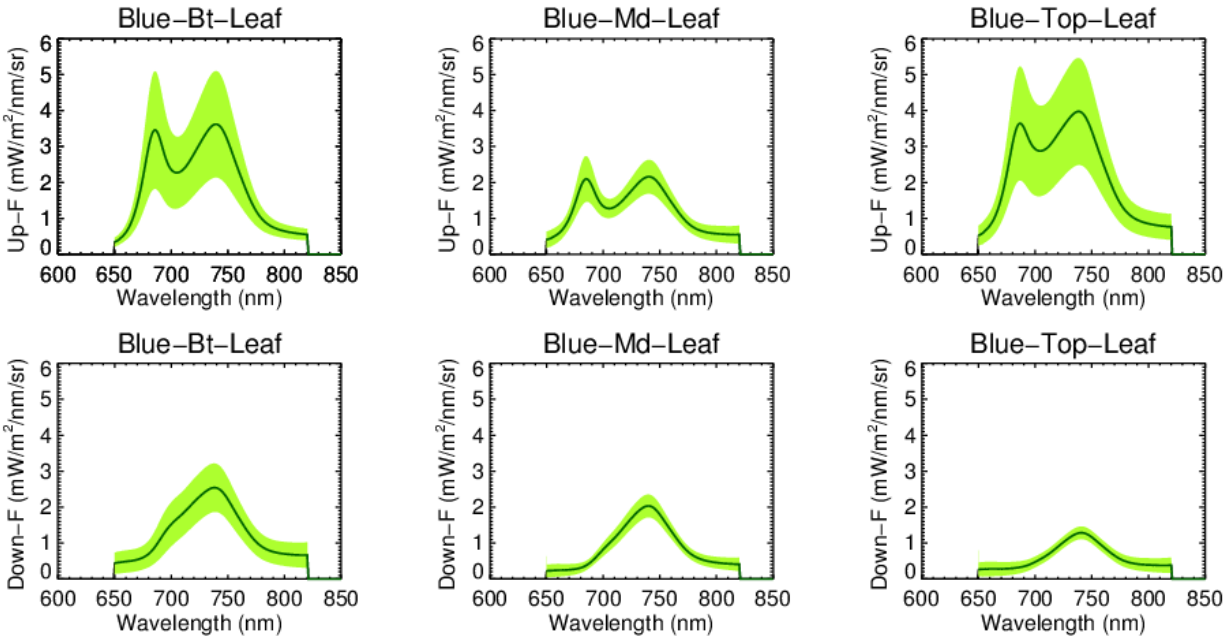

Figure 92: Eiko: Contribution of the upwelling (top) and downwelling (bottom) fluorescence leaves illuminated by BLUE-LED.

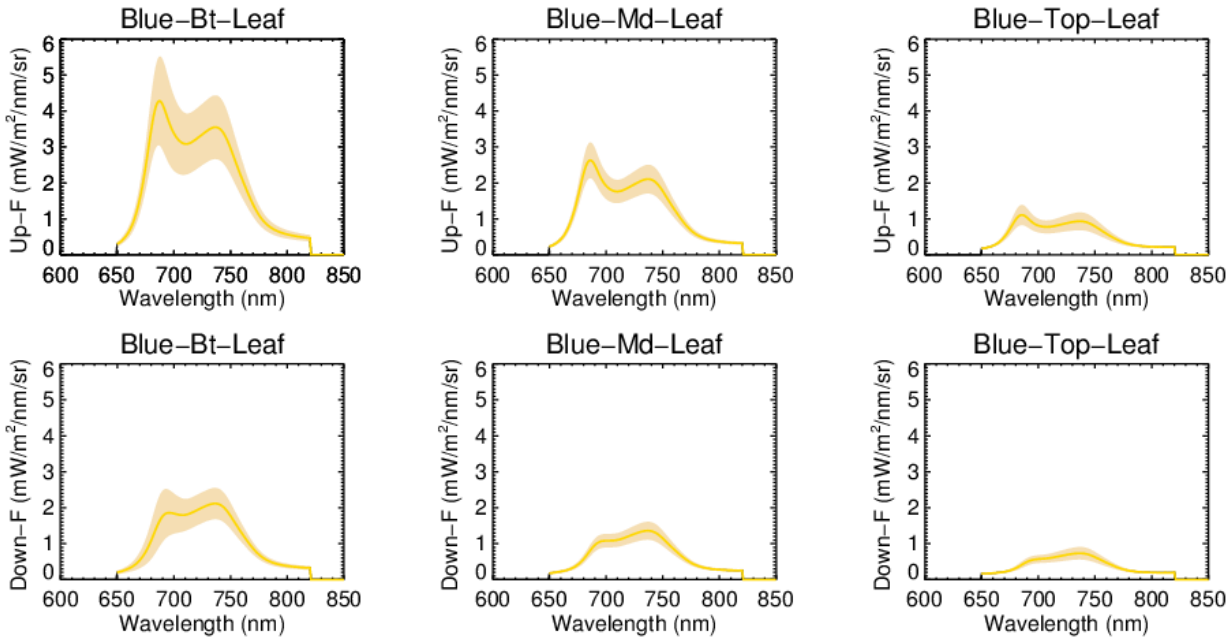

Figure 93: Minngold: Contribution of the upwelling (top) and downwelling (bottom) fluorescence leaves illuminated by BLUE-LED.

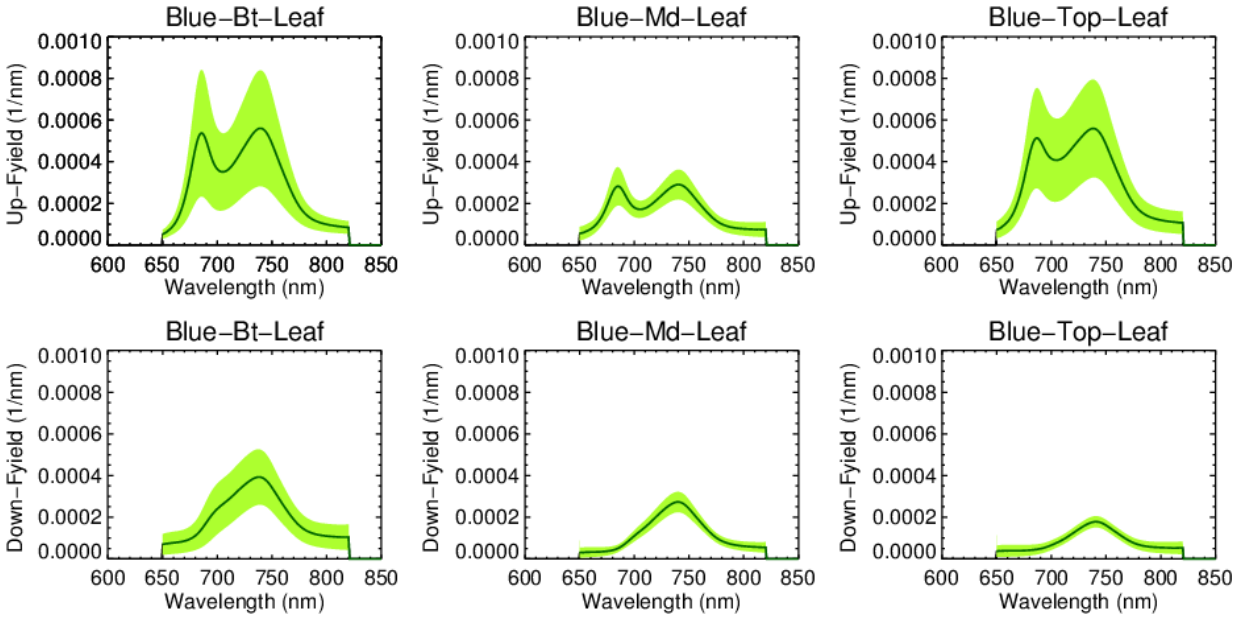

Figure 94: Eiko: Contribution of the upwelling (top) and downwelling (bottom) fluorescence yield leaves illuminated by BLUE-LED.

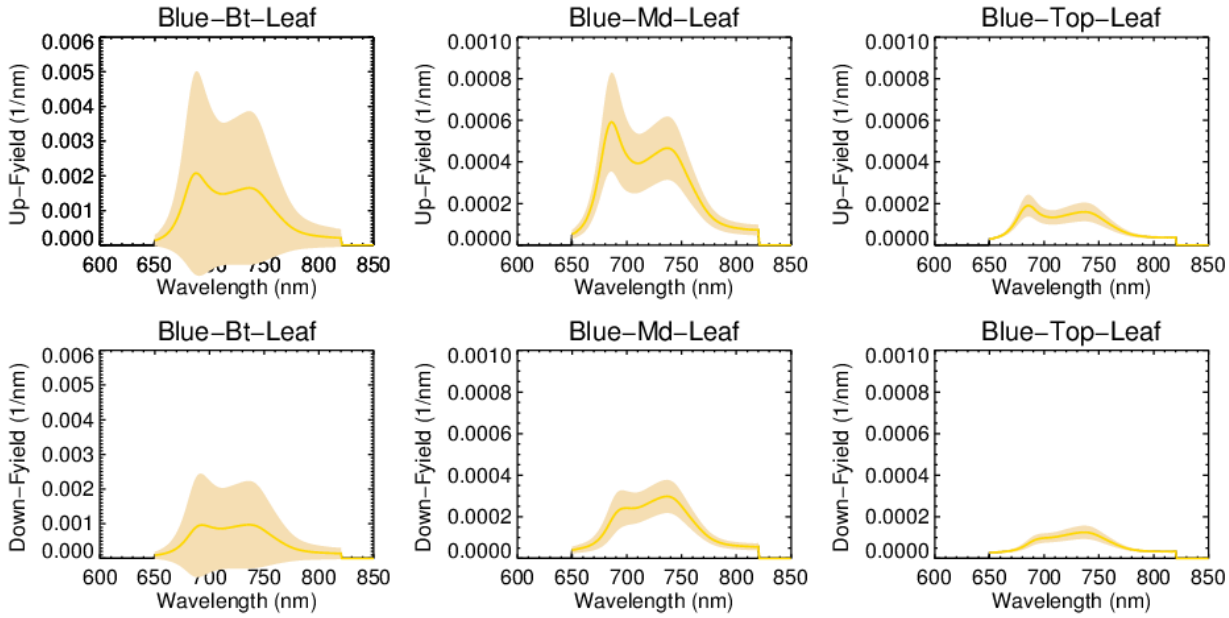

Figure 95: Minngold: Contribution of the upwelling (top) and downwelling (bottom) fluorescence yield leaves illuminated by BLUE-LED.

Additionally, passive fluorescence measurements were conducted on fully developed, sun exposed leaves located in the top layer of the canopy. The upwelling (Fup) and downwelling (Fdw) fluorescence and fluorescence yield emission of both soybean varieties is shown in Figure 96. From this data set we can corroborate the leaf-level results reported in the final report of the 2015 SoyFLEX campaign [RD-4]. The upwelling Eiko fluorescence shows a higher far-red fluorescence peak that the MinnGold, but a reversed behaviour for the red fluorescence peak. The downwelling fluorescence emission of MinnGold has the same shape as the upwelling. The downwelling emission of the Eiko shows higher fluorescence values in the far-red peak and the emission in the red is so low that no red peak signal is visible, due to the reabsorption of the red fluorescence in the Eiko. Finally, when computing total fluorescence Eiko presents lower fluorescence values than Minngold at 680nm but not at 760 nm (Figure 96).

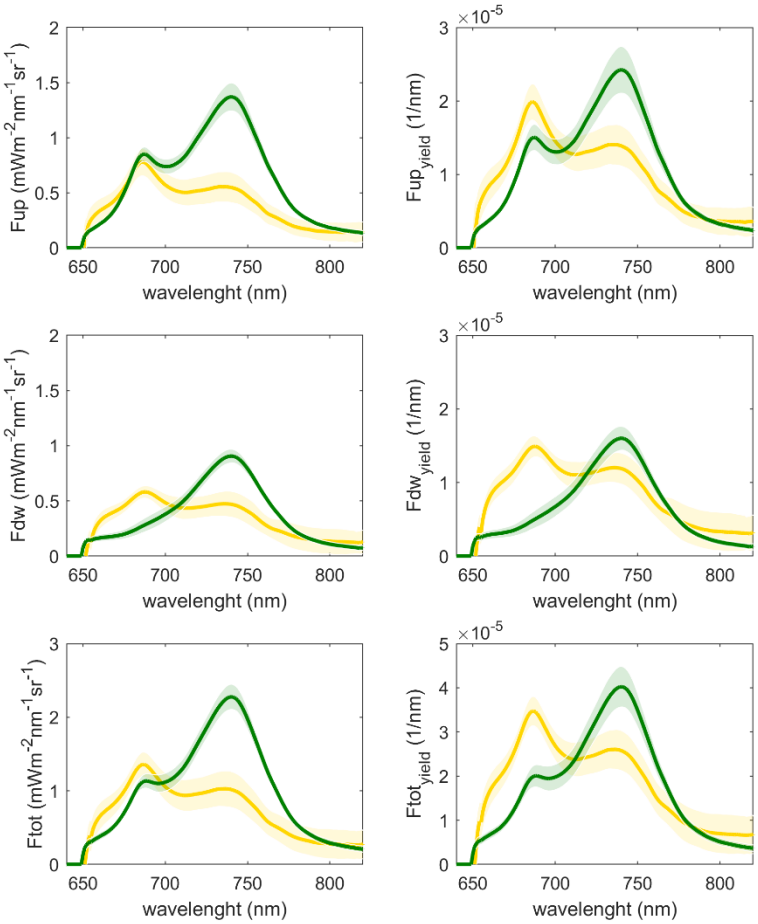

Figure 96: Contribution of the upwelling (Fup), downwelling (Fdw), and total (Ftot = Fup + Fdw) fluorescence (left-panels) and fluorescence yield (right- panels -panels) leaves illuminated sun light. Green lines (Eiko) and yellow lines (Minngold).

Finally, reflectance (Figure 97) and transmittance (Figure 98) were measured on leaves sampled at the three heights (bottom, middle and top canopy) under sunlight illumination. Measurements were carried out on detached leaves. By using the measured reflectance and transmittance we calculated the Fraction of Absorbed Photosynthetic Active Radiation for each measured bottom, middle and top leaf ($FAPAR_{leaf}$) as described in chapter 4.2.4 (Figure 99). At leaf level $FAPAR_{leaf}$ Eiko is higher than $FAPAR_{leaf}$ Minngold for all three canopy layers. Additionally, in both varieties not clear difference were observed between the $FAPAR_{leaf}$ measured bottom, middle, and top leaves (Figure 99).

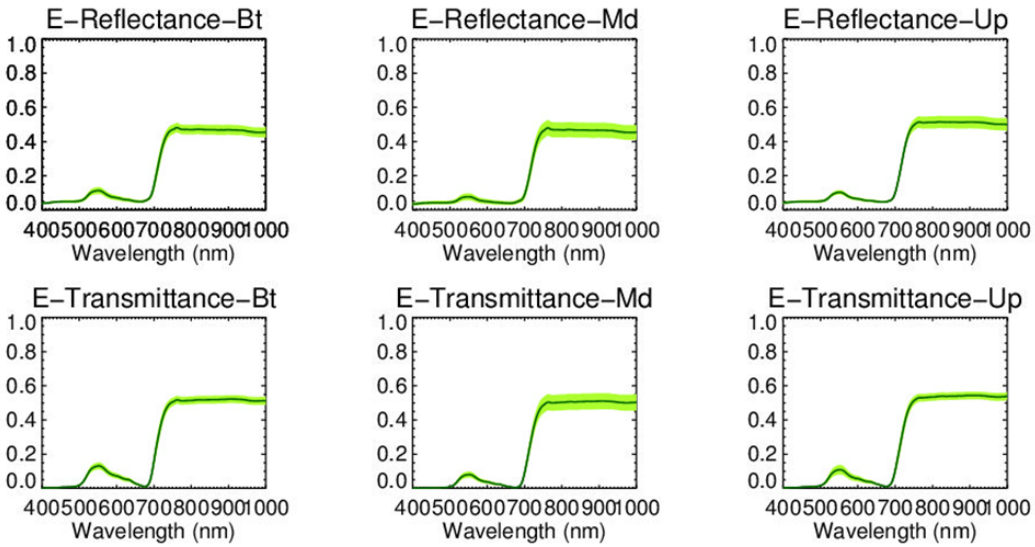

Figure 97: Eiko reflectance (top graphs) and transmittance (bottom graphs) spectrum for bottom (Bt), middle (md), and top (Up) leaves.

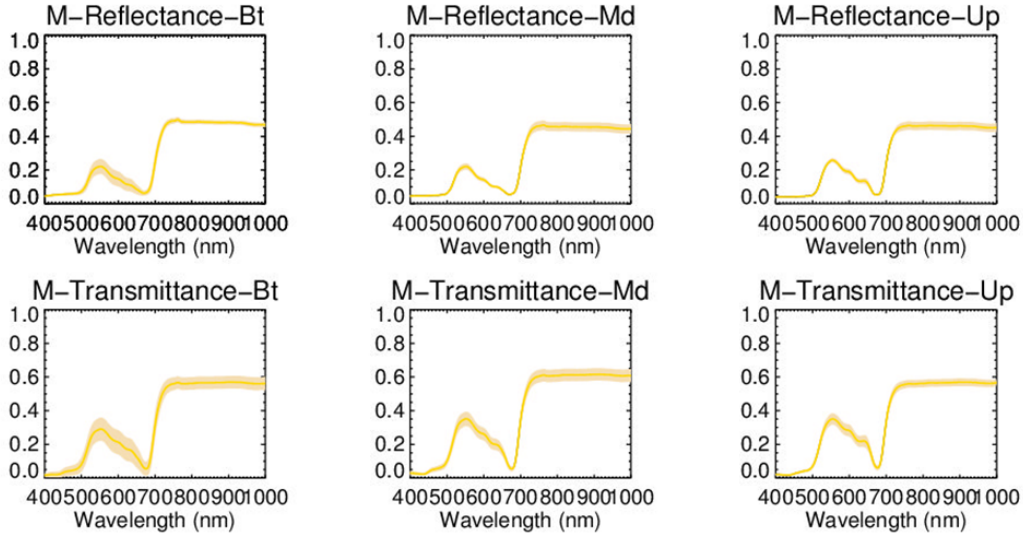

Figure 98: Minngold reflectance (top graphs) and transmittance (bottom graphs) spectrum for bottom (Bt), middle (md), and top (Up) leaves.

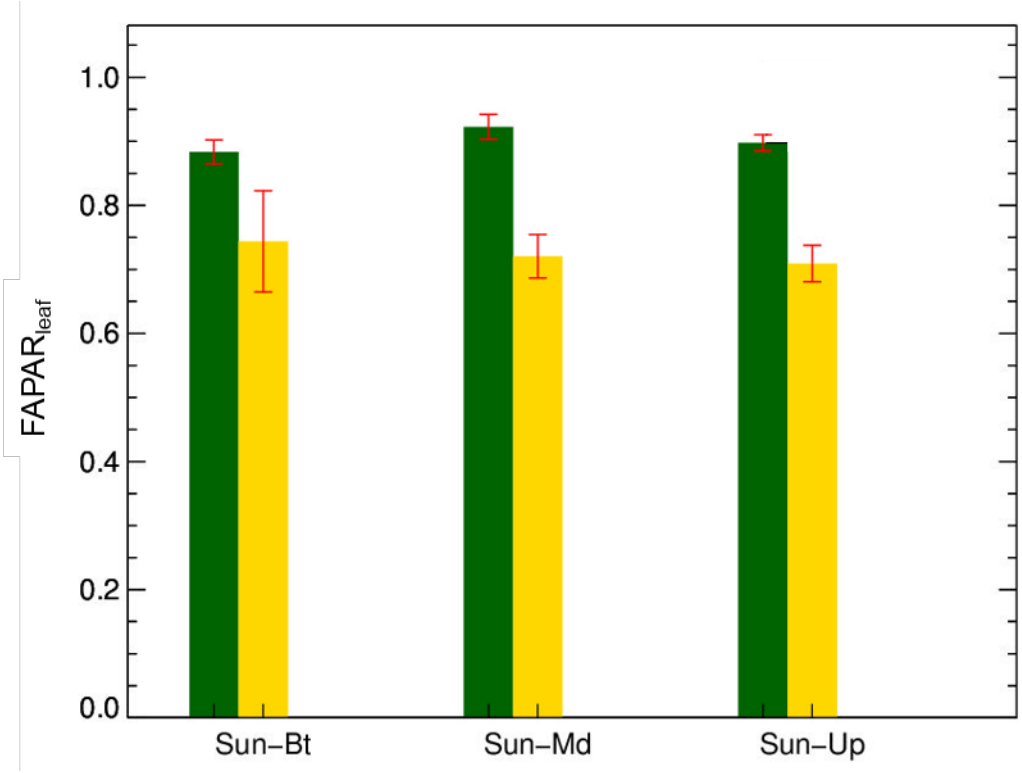

Figure 99: MinnGold (yellow) and Eiko (green) $FAPAR_{leaf}$ for bottom (Bt), middle (md), and top (Up) leaves.

6.3.5 TOC reflectance and fluorescence

The average and standard deviation of the reflectance spectra of the two soybean varieties of M1 plot in a single day of measurements (25th July, DOY 207) is shown in Figure 100. Compared to the WildType, MinnGold shows higher reflectance in the green region, a shift of the red-edge towards shorter wavelengths and higher reflectance in the NIR region. In the visible region, WildType and MinnGold differ mainly due to the different chlorophyll content (average total chlorophyll content: ≈45 µg cm^{-2} in WildType and ≈12 µg cm^{-2} in MinnGold, see section 6.3.3) and due to the different leaf structure in the near-infrared region.
Figure 101 shows the corresponding fluorescence spectra estimated from TOC radiance measurements. The two investigated soybean varieties exhibit large differences in the fluorescence shape within the 670-780 spectral range. The WildType is characterized by a strong emission in the far-red region, while in the red region values are relatively low, with a peak ratio (fluorescence maximum in the far-red / fluorescence maximum in the red region) greater than 2. In the MinnGold there is a strong reduction in the emission in the far-red and a significant increase in the red region. As result, the magnitude of the two peaks is more similar and the peak ratio is close to 1. The fluorescence change of the chlorophyll-deficient variety leaves clearly reveals changes in pigment content and different re-absorption processes, which are associated to the overall canopy photosynthetic activity.
The temporal behaviour of NDVI, MTCI, F_{687}, F_{760}, Fy_{687} and Fy_{760} for both the varieties is shown in Figure 102. Due to variability in illumination conditions and fast changes in soil moisture related to rainfall and irrigation, it is not possible to properly evaluate a potential trend in such a short time. However, WildType seems to be quite resistant to fast changes and the overall fluorescence variability is less pronounced than in MinnGold. Both red and far-red fluorescence and yields of the MinnGold variety seem more reactive to changes in environmental conditions. In the MinnGold, the total red fluorescence that escapes the canopy is larger than the scattered far-red fluorescence and often higher than the WildType red fluorescence. We can preliminary consider that higher absorbed PAR radiation (APAR WildType≈1682 µmol m^{-2} s^{-1}, APAR MinnGold≈1567 µmol m^{-2} s^{-1},see section 6.3.3) drives the higher values of the far-red fluorescence of the green variety, and that the leaves in the lower layer strongly contribute to increase the emitted flux of the MinnGold variety in the red region.
The TOC reflectance and fluorescence measurements acquired over the two soybean varieties are needed for comparison with *HyPlant* estimates (section 6.2.3) and useful in the context of the modelling study presented in section 6.3.6, aimed at testing the impact of the re-absorption processes in the TOC fluorescence signal.

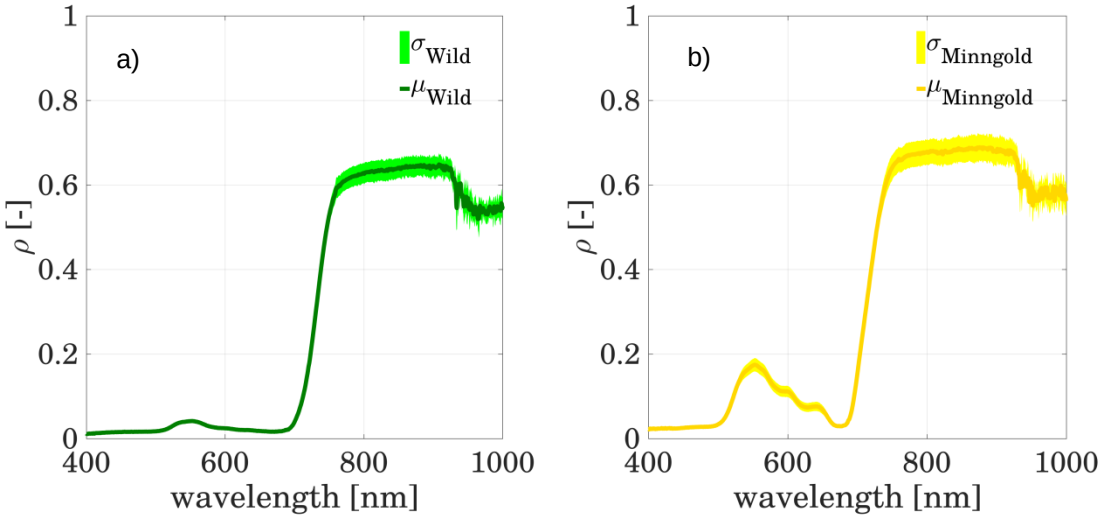

Figure 100: Example of reflectance spectra (mean and standard deviation) calculated from hyperspectral TOC measurements acquired over the WildType Eiko (a) and MinnGold (b).

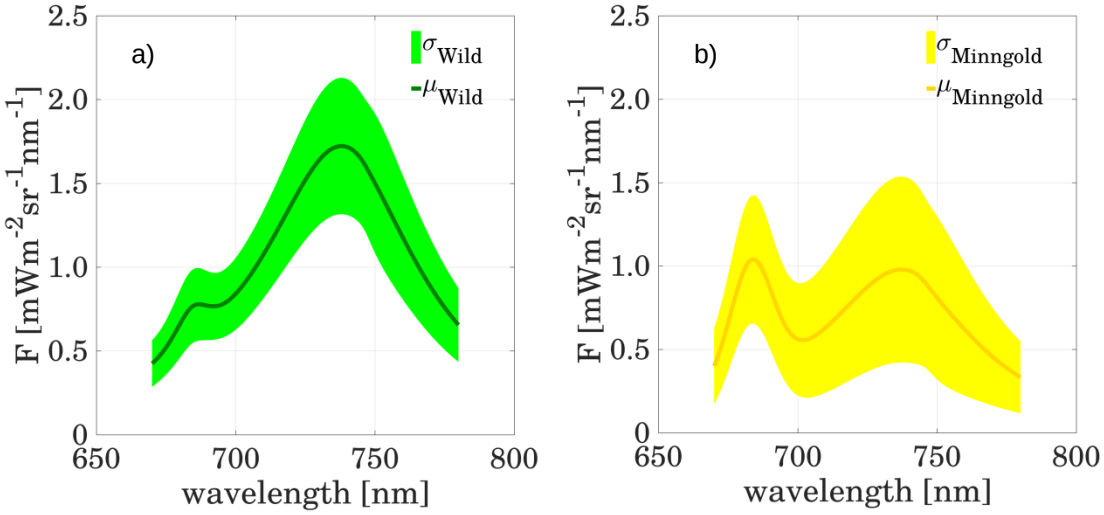

Figure 101 Example of fluorescence spectra (mean and standard deviation) retrieved from hyperspectral TOC measurements acquired over the WildType Eiko (a) and MinnGold (b).

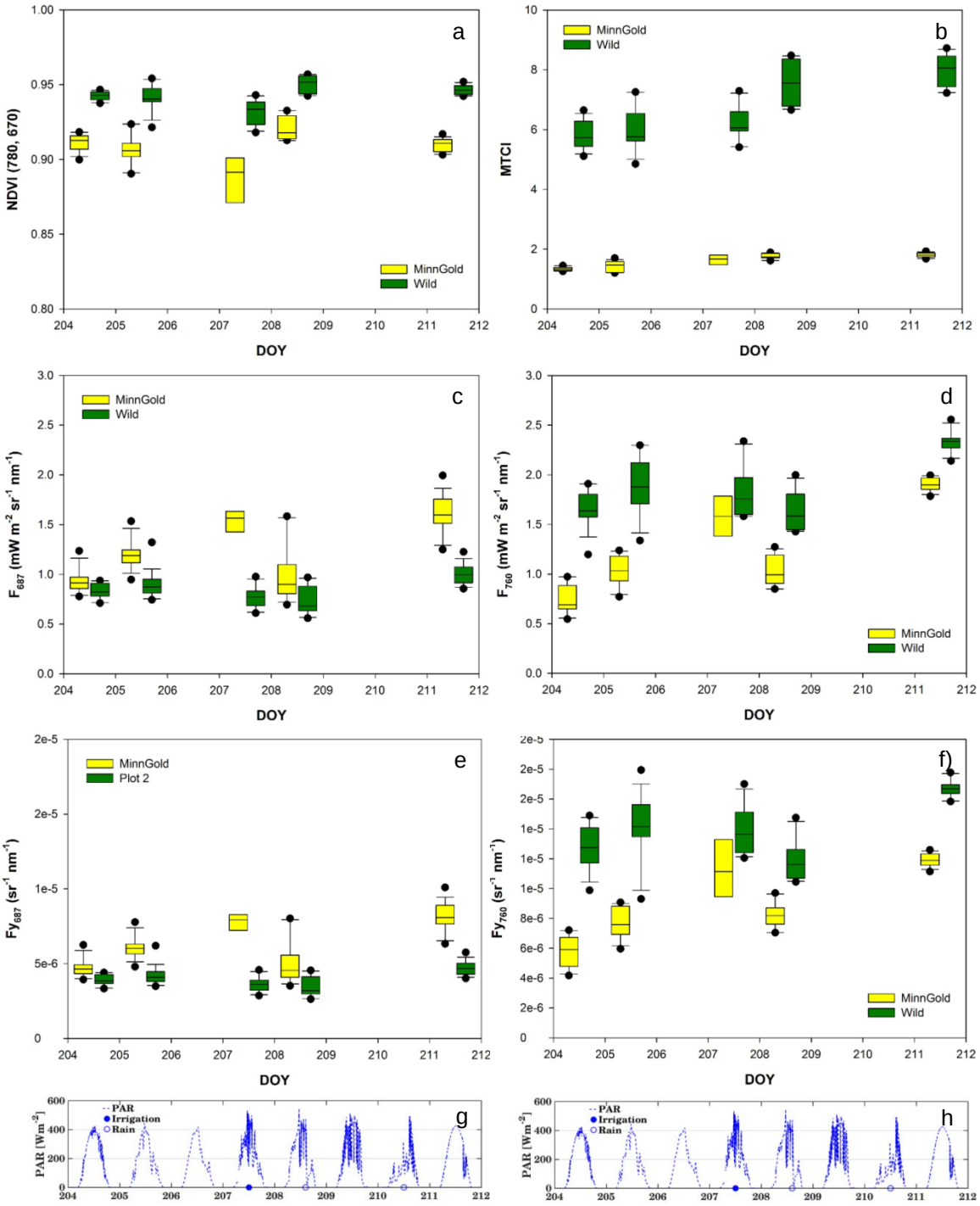

Figure 102: Temporal variation of NDVI (a), MTCI (b), F_{687} (c), F_{760} (d), Fy_{687} (e) and Fy_{760} (f) in MinnGold and WildType over the different measurements days. In plots g and h the diurnal cycle of incoming photosynthetically active radiation (PAR) for each day is shown. Days where rain and irrigation occurred are also marked (empty and full dots respectively).

6.3.6 Analysis reflectance and fluorescence of Eiko and MinnGold with SCOPE

For the SoyFLEX2 experiment, we worked with two soybean varieties (Eiko and MinnGold) with significantly different chlorophyll content (Figure 83) but with the same photosynthetic rate (Figure 82). When measuring the sun-Induced fluorescence emission spectra on fully developed, sun-exposed

leaves located in the top layer of the canopy (Figure 96) we observed that fluorescence of Eiko was similar to that of MinnGold for the red fluorescence peak at 680 nm, but higher than that of MinnGold for the far-red fluorescence. Those results are in line with the observation from the SoyFLEX experiment in 2015 [RD-4] and support already known results from the literature (Porcar-Castell *et al.*, 2014). Changes in the red fluorescence peak (F680) are associated with the plant photochemistry and the far-red fluorescence peak (F760) is related to the chlorophyll content and structural parameters.
However, top of canopy (TOC) sun-induced fluorescence values measured at ground (Figure 101) and from the *HyPlant* airborne sensor (Figure 64, Figure 67) show lower red fluorescence values (F687) for Eiko than for MinnGold, but a higher far-red fluorescence peak (F760) in Eiko than in MinnGold.
The difference observed between leaf and TOC measurements may be due to the scattering and re-absorption of the fluorescence emitted within a leaf and in the canopy (Gitelson *et al.*, 1998).

The model SCOPE enables the quantification of the three processes leading to SIF: (1) absorption of PAR, (2) emission of fluorescence and (3) scattering and re-absorption of fluorescence. With the model, the difference between the two varieties of all three steps can be calculated. By outputting the emitted fluorescence directly, the step of re-absorption can be artificially avoided. The ratio of fluorescence with to without re-absorption, gives the so-called 'escape probability': the probability that an emitted fluorescence photon escapes the leaf or canopy, and the complementary fraction: the probability that an emitted photon is re-absorbed. This computation can be done for both for individual leaves (to estimate the re-absorption immediately after emission) and in the canopy (to estimate the re-absorption due to multiple interactions among leaves and soil).

In ensure a correct representation of the three processes of absorption, emission and re-absorption, SCOPE needs to be parameterized. This was done by retrieving the model input parameters using measured reflectance, transmittance and fluorescence of leaves, and measured reflectance of the whole canopy. These measurements enable the characterization of the scattering and absorption properties of the canopy, via the model input parameters of pigments, leaf thickness, leaf area and orientation. The retrieval and simulation of re-absorption was carried out in the following three steps (Figure 103):

- Step 1: we used leaf reflectance and transmittance measurements to retrieve the following leaf biochemical parameters: C_{ab}, C_{dm}, C_s, C_w, C_{ca}, and N. These parameters characterize the leaf optical properties, and determine the absorption of PAR, the emission of fluorescence, and the re-absorption of fluorescence in the leaf as described in the model Fluspect (Vilfan et al., 2016).
- Step 2: we used TOC reflectance to retrieve 1) the leaf biochemical (i.e. C_{ab}, C_{dm}, C_s, C_w, C_{ca}, and N), and 2) canopy structural parameters (i.e. LAI, LIDfa, and LIDFb). Furthermore, we retrieved the parameter C_x (Vilfan et al, in review), which quantifies the status of the Xanthophyll cycle in the spectral region of 500-600 nm, a parameter related to NPQ. We used the mean value from the leaf biochemical parameters computed in step 1 as a starting point and prior information to retrieve the same parameters but with TOC reflectance. The values of biochemical parameters retrieved in Step 1 help overcome the common problem of ill-posed parameter retrievals from TOC data alone.
- Step 3: we used the retrieved parameters in step 2 plus meteorological parameters to run the forward simulation and estimate canopy photosynthesis (A_{net}), absorbed PAR (APAR), the fraction of absorbed PAR (FAPAR), the distribution of APAR among leaves in the canopy, sun-induced fluorescence considering and not considering the re-absorption at leaf and canopy level (Figure 104), and the escape probability (i.e. the probability of a photon the skip the leaf or/and canopy and reaches the sensor).
  - ➔ Step 2 and 3 were carried out using both TOC ground reference data and *HyPlant* data.

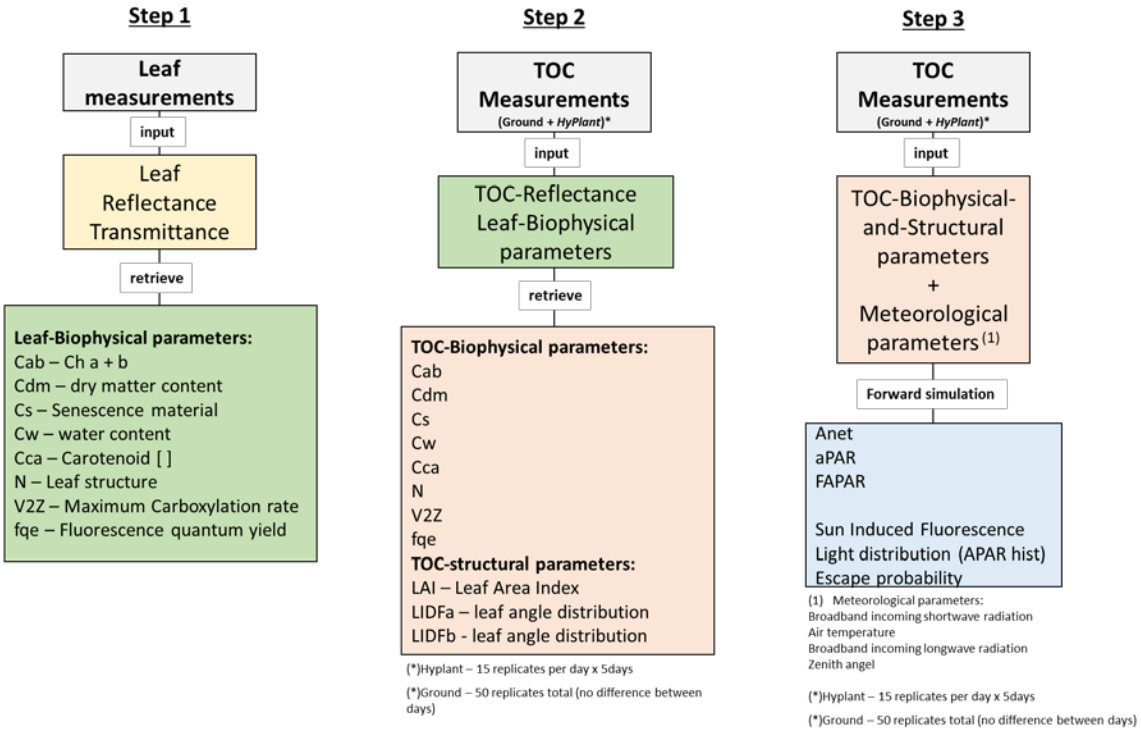

Figure 103: Scheme followed to model plant photosynthesis (Anet), APAR, FAPAR, and sun-induced fluorescence.

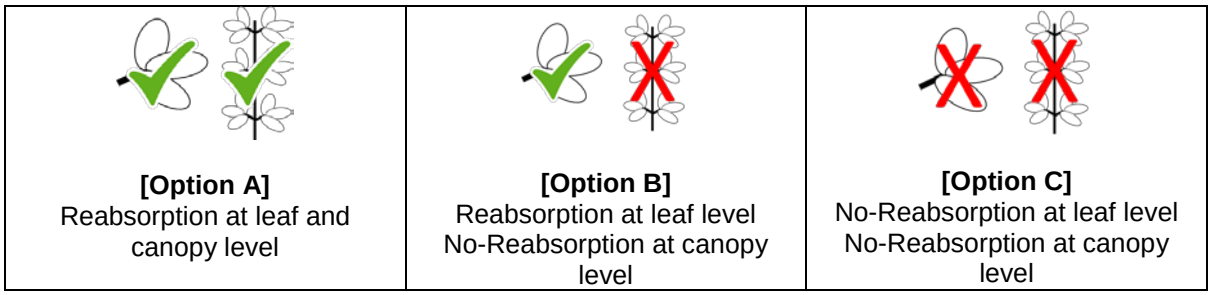

Figure 104: Sun-induced fluorescence forward simulation considering and not considering the re-absorption at leaf and canopy level.

From these three forward simulations options, the escape probability is calculated as follows:

$$f_{esc,canopy} = \frac{\pi L_{F,option\,A}}{E_{F,option\,B}} \quad (17)$$

$$f_{esc,leaf+canopy} = \frac{\pi L_{F,option\,A}}{E_{F,option\,C}} \quad (18)$$

Where E_F is the emitted fluorescence by all leaves together ($Wm^{-2}\ \mu m^{-1}$) in the scenarios A and B, and πL the fluorescence radiance at the TOC multiplied by π in scenario A, in which re-absorption and scattering at both leaf and canopy level is calculated. The definitions above are strictly speaking an 'observation probability' rather than an escape probability: The enumerator is the directional radiance (i.e. the radiance in observation direction) times π rather than the hemispherically integrated fluorescence radiation escaping the canopy. Therefore it also accounts for the bi-directionality of the fluorescence emission.

6.3.6.1 Comparison of measured ground and *HyPlant* reflectance spectra

The average reflectance spectra measured with the ground reference system and by the *HyPlant* sensor are presented in **Error! Reference source not found.** and **Error! Reference source not found.** for Eiko and MinnGold, respectively. Those data were used to retrieve the leaf biophysical and canopy structural parameters. Ground and *HyPlant* average reflectance spectra of Eiko (**Error! Reference source not found.**) are similar in the red region of the spectrum. In contrast *HyPlant* reflectance spectra present higher values in the far-red region For MinnGold *HyPlant* reflectance spectra present higher values in the green-red and far-red regions compared with ground measurements. These spectra were used as input for the step 2 described above.

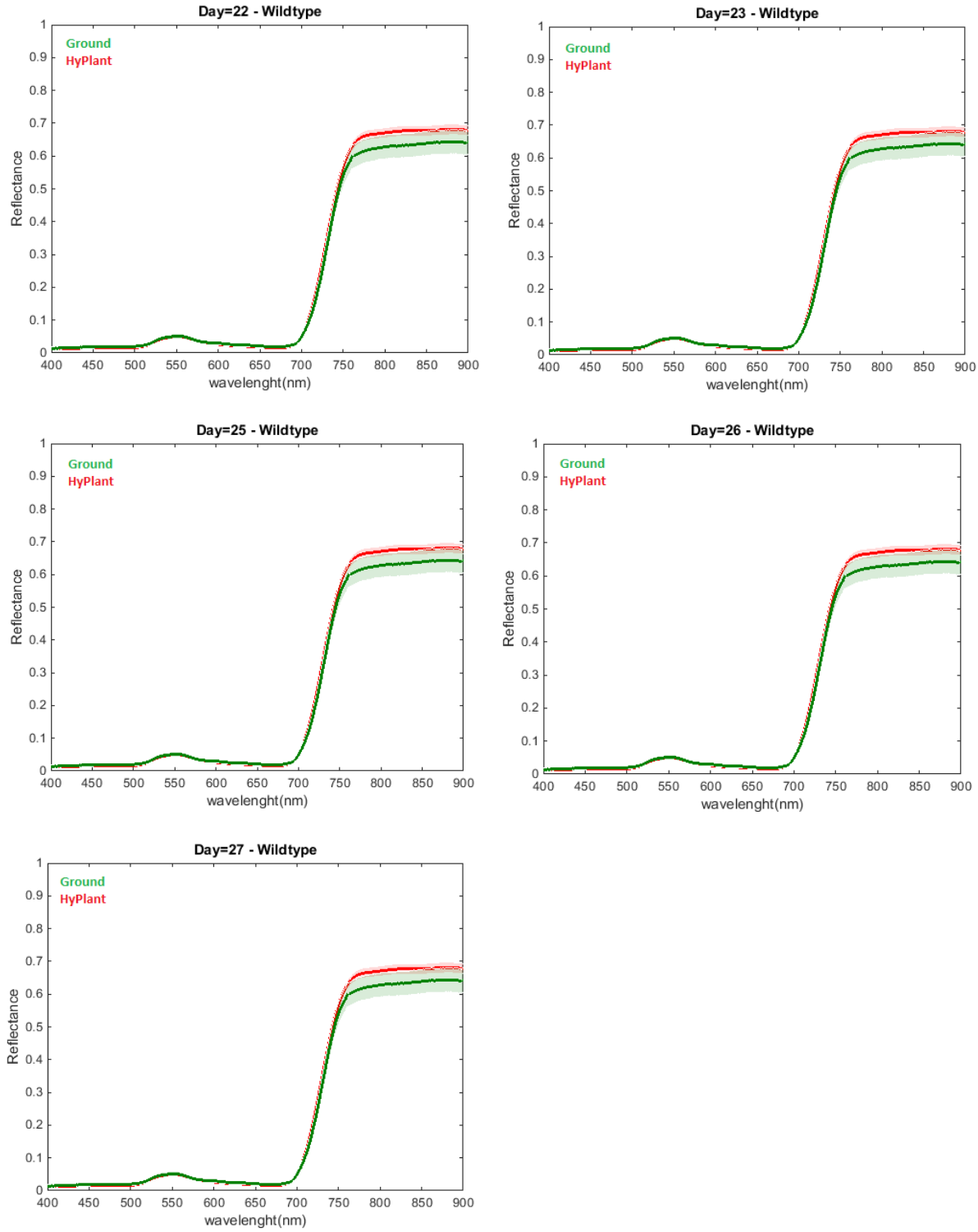

Figure 105: Eiko - Ground (green) vs *HyPlant* (red) reflectance spectrum for all measurements days.

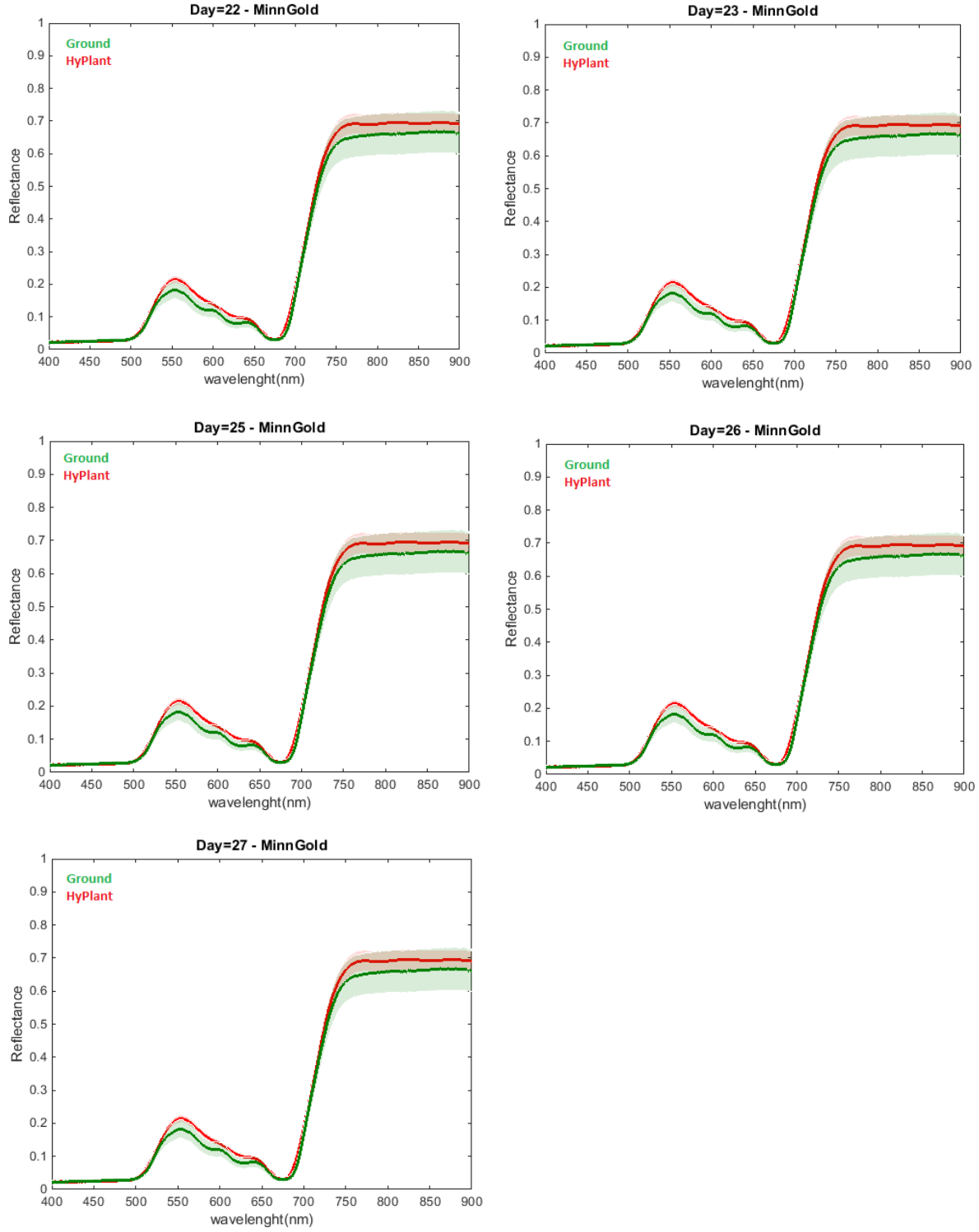

Figure 106: MinnGold - Ground (green) vs *HyPlant* (red) reflectance spectrum for all measurements days.

6.3.6.2 Comparison between measured and simulated reflectance spectra

Figure 107 shows the match between (average) measured and simulated reflectance at the ground (TOC) in the field, and Figure 108 shows the match between measured and simulated reflectance of HyPlant, both for 23 July 2016. Because HyPlant covers a wider spectral range, some parameters such

as leaf water content C_w with absorption features in the SWIR may be retrieved more accurately than from the ground. The model follows the measurements rather accurately, with a few exceptions for Eiko: green reflectance is overestimated and reflectance between 740 and 800 nm is underestimated. In the simulation of HyPlant reflectance, we find additional mismatches in the region affected by water vapour. This can be caused by imperfect atmospheric correction, but also by the fact that SCOPE does not consider water vapour absorption in the air in the vegetation.

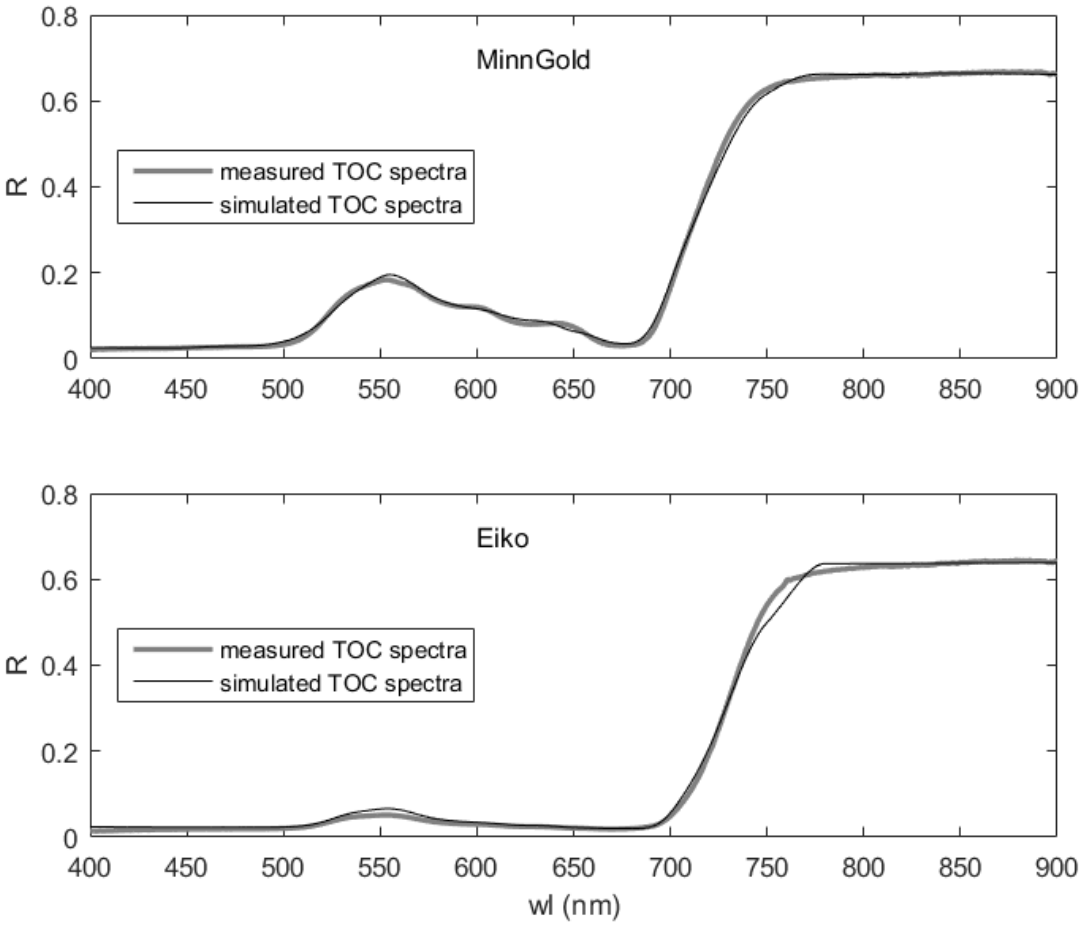

Figure 107 Measured and simulated TOC (field measured) reflectance spectra for MinnGold (top) and Eiko (bottom) for on 23 July 2016.

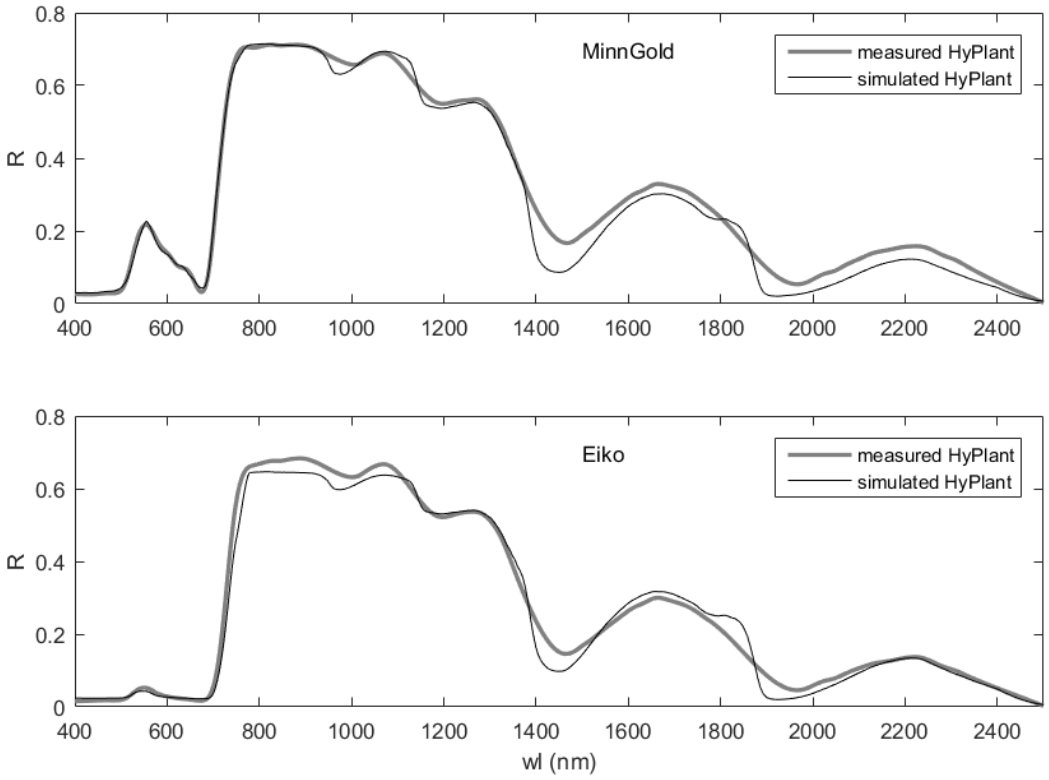

Figure 108 Measured and simulated HyPlant reflectance spectra for MinnGold (top) and Eiko (bottom) for the flight of 23 July 2016.

6.3.6.3 Leaf biophysical and canopy structural parameters

Leaf biophysical and canopy structural parameters were retrieved from the reflectance and transmittance spectra of the leaf level measurements from the FLUOWAT (Figure 97 and Figure 98), top of canopy reflectance spectra from the high resolution reference measurements (Figure 100), and top of canopy reflectance spectra from the *HyPlant* data (**Error! Reference source not found.** and **Error! Reference source not found.**). For the *HyPlant* data 15 reflectance spectra for each soybean varieties from each flight line were randomly selected. The retrieved leaf biophysical and canopy structural parameters are presented in Figure 109 and Figure 110. From these results we conclude

Eiko:

- Similar values of C_{ca}, C_w, C_s, C_x, LAI, and LIDFa can be observed between leaf, ground, and *HyPlant* retrieved parameters.
- C_{ab}: Values retrieved from *HyPlant* were lower than those retrieved from leaf and TOC reflectance.
- C_{dm}: Values retrieved from *HyPlant* where higher than those retrieved leaf and ground retrieved results.
- LIDFb: opposite results are observed between ground and *HyPlant.* LIDFb represents the bi-modality of the leaf inclination distribution function. It should be noted that reflectance exhibits little sensitivity to LIDFb, and therefore, the retrieval of LIDFb is known to be ill-posed (Verhoef et al., 2017).

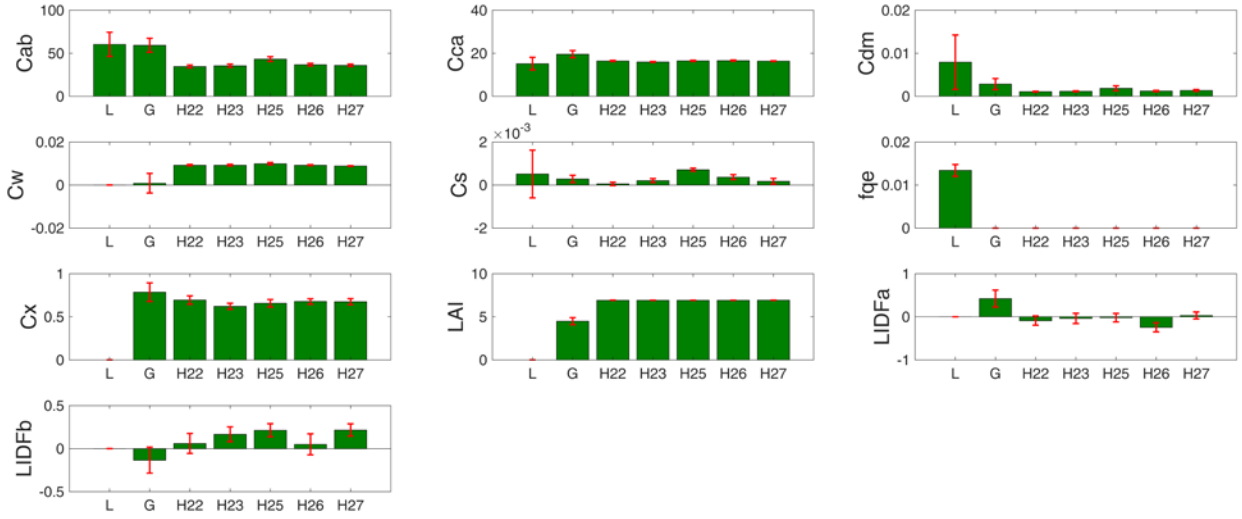

Figure 109: Wildtype - comparison between leaf (L), ground (G), and *HyPlant* (H) retrieved leaf biophysical and canopy structural parameters. H22, H23, H25, H25, and H27 correspond to *HyPlant* measurements days (step 1-2 of Figure 104).

MinnGold:

- Similar values of C_{ca}, C_w, C_s, LAI, and LIDFa can be observed between leaf, ground, and *HyPlant* retrieved parameters.
- C_{ab}: Values retrieved from *HyPlant* were lower compared with those retrieved from leaf and ground data.
- C_{dm}: Values retrieved from *HyPlant* were lower compared with those retrieved from leaf and ground data.
- C_x: Values retrieved from *HyPlant* were lower compared with those retrieved from leaf and ground data .
- LIDFb: opposite results are observed between ground and *HyPlant*.

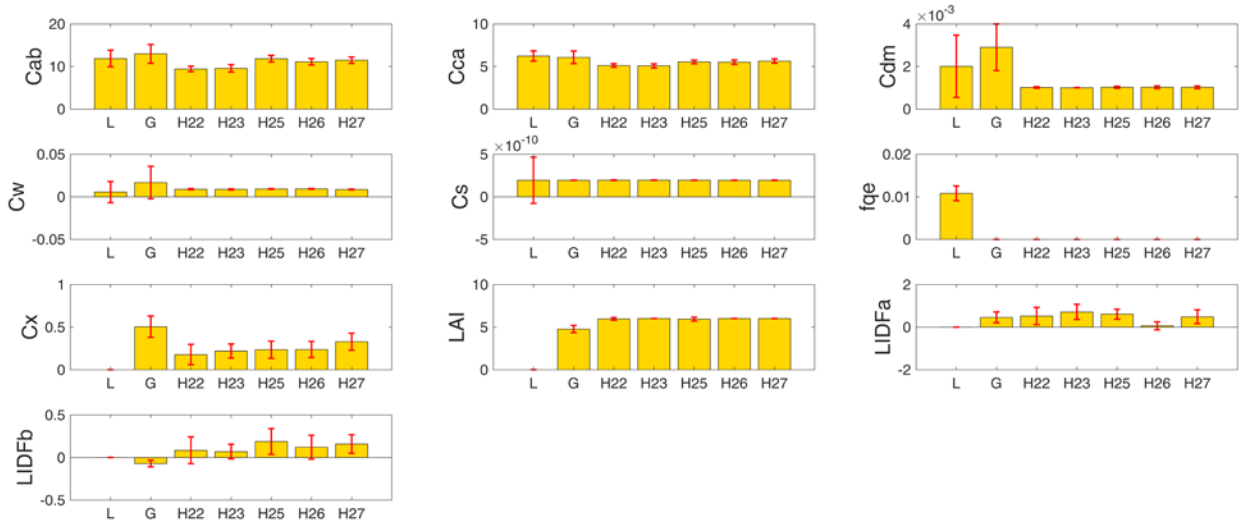

Figure 110: MinnGold - comparison between leaf (L), ground (G), and *HyPlant* (H) retrieved leaf biophysical and canopy structural parameters. H22, H23, H25, H25, and H27 correspond to *HyPlant* measurements days (step 1-2 of Figure 104).

Comparing the two varieties shows that chlorophyll concentration (C_{ab}) is the most different, as expected, with values in the order of 10 microgram cm^{-2} for Minngold and 50 microgram cm^{-2} for the Eiko. Carotenoid content also differs, and it is in the range of 35 to 50 percent of the chlorophyll concentration in both varieties. Brown/senescent material (C_s) was practically absent in both varieties. Both had a high leaf area index (LAI), but Minngold had a more horizontal leaf orientation, while Eiko has a more spherical leaf angle distribution (lower value of LIDFa). The C_x parameter indicates the status of the Xanthophyll cycle in the PRI region (500-600 nm), and it is an indicator of non-photochemical quenching. This parameter is slightly higher in the Eiko than in the MinnGold, indicating a higher non-photochemical quenching in the Eiko.

6.3.6.4 Absorbed light distribution

The chlorophyll content, but also the leaf inclination distribution (LIDFa) affect the distribution of Photosynthetic Active Radiation (aPAR). The way in which these to traits differ between the varieties, determines how aPAR differs among leaves in the two varieties. The modelled distribution (using the leaf biophysical and canopy structural parameters derived from the ground and *HyPlant* reflectance) corroborate the results presented in the final report 2015 [RD-4]. The light distribution in the MinnGold is more concentrated around intermediate values than in the Eiko, and the highest values of aPAR (for sunlit leaves) in MinnGold are lower than those in Eiko (Figure 111). These high values of aPAR correspond to light saturated conditions. The curvature of the light response curve in the biochemical model (Van der Tol etl al., 2014) in combination with the more concentrated distribution of aPAR in the MinnGold explains why SCOPE simulates similar photosynthesis rates despite lower aPAR of Minngold, and thus a higher light use efficiency in Minngold than in Eiko.

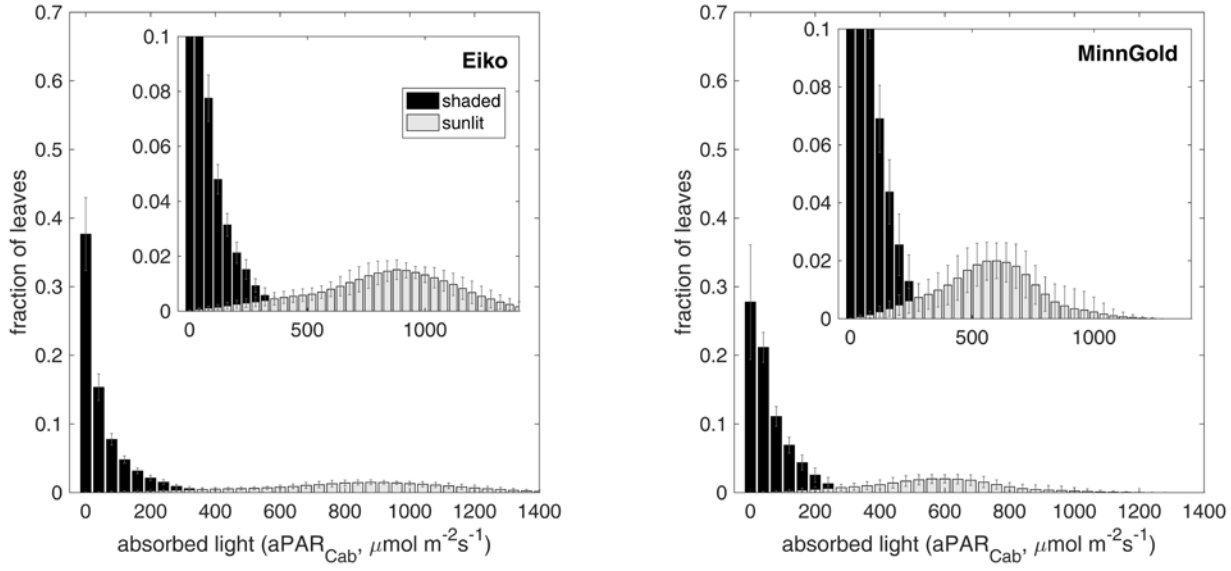

Figure 111: Top of Canopy aPAR distribution retrieved from ground measurements of TOC reflectance.

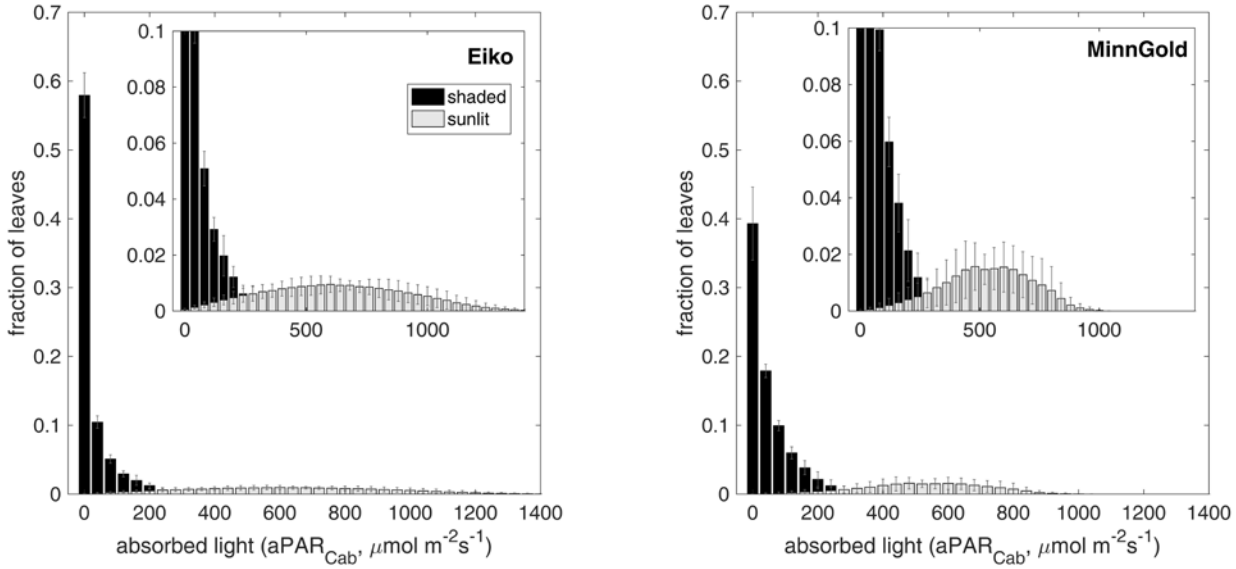

Figure 112: Top of Canopy aPAR distribution retrieved from *HyPlant* reflectance data.

6.3.6.5 Photosynthesis rate and fraction of absorbed photosynthetic active radiation

Two additional output parameters, the photosynthetic rate in μmol m^{-2}s^{-1} and the Fraction of Absorbed Photosynthetic Active Radiation (FAPAR) at canopy level are produced by the SCOPE forward simulation. The results are presented in Table 30. When using the input parameters derived from both ground and HyPlant measurements the modelled photosynthetic rate of Eiko and MinnGold are similar. The comparison of the modelled photosynthetic rates with measured GPP values (Figure 82) at the same amount of aPAR showed considerably lower values for modelled photosynthetic rate than measured photosynthesis.
The fraction of absorbed photosynthetic active radiation FAPAR at canopy level showed rather similar values between both modelled (Table 30) and measured FAPAR$_{canopy}$ values (Figure 84).

Table 30: Top of CANOPY forward simulation: Photosynthesis and FAPAR (step 3 of Figure 104).

	Parameter	Eiko	MinnGold	Units
Ground	**Photosynthesis**	34.50±1.37	36.05±3.41	μmol $m^{-2}s^{-1}$
	aPAR	1592±132	1375±231	μmol $m^{-2}s^{-1}$
	FAPAR	0.95±0.01	0.88±0.02	
HyPlant	**Photosynthesis**	33.50±3.76	36.85±4.29	μmol $m^{-2}s^{-1}$
	aPAR	1515±308	1385±267	μmol $m^{-2}s^{-1}$
	FAPAR	0.95±0.00	0.87±0.00	

n-ground = 50 and n-*HyPlant* = 45 (15 points x 3 days)

6.3.6.6 Sun-induced fluorescence forward simulation

The sun-induced fluorescence emission was modelled in three different options as forward simulation (Figure 104) considering:

- Option A – Reabsorption leaf and canopy level (the fluorescence 'as observed')
- Option B – Reabsorption leaf and no-reabsorption canopy level (i.e. the fluorescence emitted by all leaves together)
- Option C – No-Reabsorption at leaf and canopy level (i.e. the fluorescence emitted by all photosystems together)

All option were simulated first with the vegetation parameters retrieved from TOC ground measurements as input (simulation1) and then with those retrieved from *HyPlant* measurements as input (simulation2).

SIMULATION 1: GROUND input data

The fluorescence and fluorescence yield resulting from the three different forward simulations for MinnGold and Eiko are presented in Figure 113 and Figure 114, respectively. The three simulation options represent (A) the 'as observed' fluorescence, including the emission and re-absorption, (B) the fluorescence emitted by all leaves, including leaf re-absorption but no canopy reabsorption, and (C) the total emitted fluorescence by all photosystems.
Comparing the three cases gives insight in the process of reabsorption, which is particularly strong in the Eiko.
The forward model considering both the reabsorption at leaf and canopy level (Option A) produces the SIF 'as observed'. Hence, similar patterns as for the field conditions should be observed. In fact, red-fluorescence emission (F680) was lower in Eiko than in MinnGold, while the far-red fluorescence emission was higher in MinnGold. However, the model overestimates the fluorescence modelled at F760 in both Eiko and MinnGold (Figure 101 and Figure 113).
When considering re-absorption only at leaf level (Option B), the total fluorescence spectral emission increases compared to option A. In general, the emission spectra of both varieties (Figure 113, lower left) show a similar pattern as the measured total fluorescence (Fup + Fdw) at leaf level (Figure 91), showing lower fluorescence emission at F680 in Eiko than in MinnGold and vice versa for the far-red fluorescence peak (F760). The forward modelling without considering any re-absorption, neither on the leaf nor on the canopy level (Option C) resulted in a further increase of the total fluorescence emission for both soybean varieties (Figure 113). For both varieties, Eiko and MinnGold, the fluorescence emitted at F680 is higher than the fluorescence emitted at F760. Where the overall fluorescence spectrum is higher in Eiko than MinnGold due to higher chlorophyll content of the Wildtype variety.

Normalization of fluorescence by aPAR provides the fluorescence yield. This calculation was carried out for all three scenarios (options A, B and C) (Figure 114) When the emitted fluorescence is normalized by the absorbed PAR the difference between Eiko and Minngold varieties decrease. For top of canopy fluorescence, MinnGold present higher fluorescence yields at both F680 and F760 (Option A, Figure 114 left). As in Figure 113 when considering re-absorption only at leaf level (Option B, Figure

114 middle) F680 is higher in MinnGold than Wildtype, however after normalizing by absorbed PAR similar values are observed between MinnGold and Wildtype at F760. Finally, when not considering any re-absorption at leaf and canopy level (Option C, Figure 114 right), this modelling scenario resembles the fluorescence emission at chloroplast level, for which both varieties show a very similar fluorescence yield. This indicates that physiological differences between the two varieties, i.e. differences in the photochemical and non-photochemical pathways, are small.

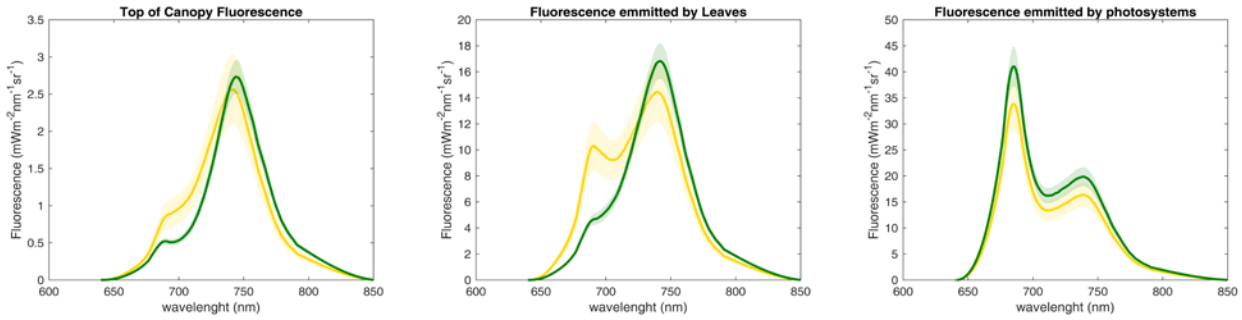

Figure 113: Top of Canopy – Ground – Sun Induced Fluorescence: considering and not considering the re-absorption at leaf and canopy level.

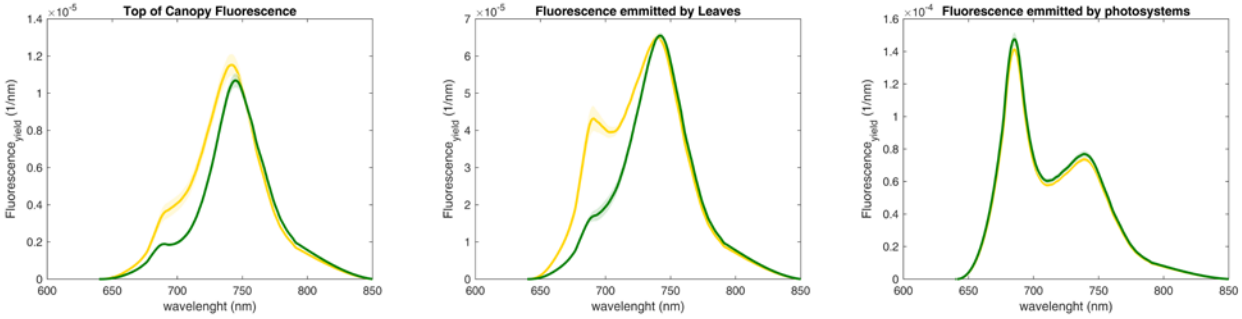

Figure 114: Top of Canopy – Ground – Sun-induced fluorescence yield ($Fluorescence_{yield}$): considering and not considering the re-absorption at leaf and canopy level.

SIMULATION 2: *HYPLANT* input data

When using *HyPlant* reflectance data to model fluorescence an overestimation of the fluorescence emitted by MinnGold variety can be observed (Figure 115) compared to field measurements (Figure 101) and ground modelled results (Figure 113). This overestimation translates to all different simulations (Figure 115 and Figure 116).
As described in Figure 103 the TOC ground and *HyPlant* reflectance spectrum is used to retrieve 1) leaf biochemical (i.e. Cab, Cdm, Cs, Cw, Cca, V2Z, fqe, and N) and 2) canopy structural parameters (i.e. LAI, LIDfa, and LIDFb) (Figure 109 and Figure 110) – [step 2]; which later [step 3] are used to run the forward simulation and estimate Sun induced fluorescence considering and not considering the re-absorption at leaf and canopy level. Thus the results observed when using *HyPlant* data could be explained by the differences between ground and *HyPlant* reflectance spectrum (**Error! Reference source not found.** and **Error! Reference source not found.**) which also drive the mismatch found between ground and *HyPlant* retrieved biochemical and structural parameters (Figure 109 and Figure 110).

Further investigations should be done to corroborate this hypothesis. Currently we are evaluation all the factors involved in the *HyPlant* forward simulation (i.e. input data, model, code used…) to understand the origin of the problem and then fix it.

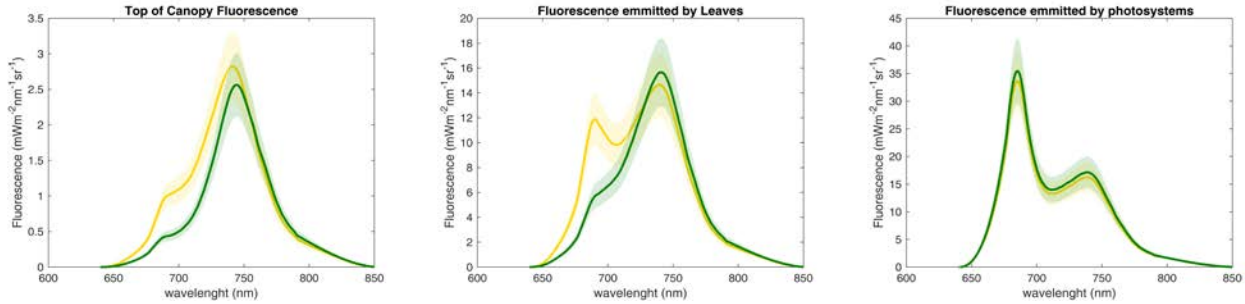

Figure 115: Top of Canopy – *HyPlant* – Sun-induced fluorescence: considering and not considering the re-absorption at leaf and canopy level

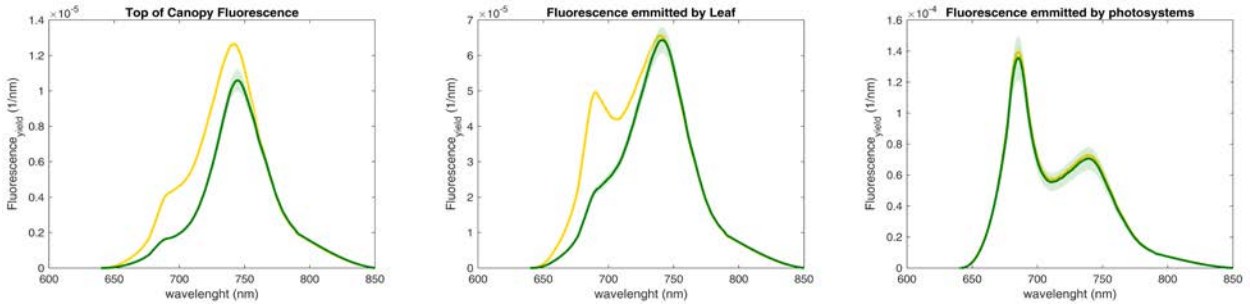

Figure 116: Top of Canopy – *HyPlant* – Sun-induced fluorescence yield ($Fluorescence_{yield}$): considering and not considering the re-absorption at leaf and canopy level

6.3.6.7 Escape probability

The escape probability is presented in Table 31. Due to differences in chlorophyll content, the escape probability is slightly higher in Minngold than Eiko. However, the difference observed between both varieties is not as pronounced as may be expected; it may be explained by the similar LAI found between both varieties (Figure 87, Figure 109, and Figure 110).

Table 31: Escape probability (%) for both soybean varieties, Eiko and MinnGold canopy and leaf + canopy level. The escape probability was calculated for Simulation 1 using ground input data and simulation two using *HyPlant* data as input parameters.

	Escape probability (%)	Eiko	MinnGold
Simulation 1 - Ground	Canopy	0.47 ± 0.02	0.46 ± 0.02
	Leaf + Canopy	0.21 ± 0.01	0.27 ± 0.02
Simulation 2 - *HyPlant*	Canopy	0.45 ± 0.00	0.48 ± 0.01
	Leaf + Canopy	0.23 ± 0.01	0.30 ± 0.00

n-ground = 50 and n-*HyPlant* = 45 (15 points x 3 days)

6.3.7 Concluding remarks

The SoyFLEX2 experiment was a repetition of the experiment held in 2015 in Campus Klein-Altendorf (Germany), set up on a large scale, using two different soybean varieties. Those varieties, Eiko and MinnGold, mainly differ in the leaf chlorophyll content (Figure 83) and leaf inclination distribution, which translates into substantial and well detectable changes in leaf and canopy optical properties. Measured steady-state photosynthesis is comparable in the two varieties both at the leaf (Sakowska et al., submitted) and at the canopy scale (Figure 82). Leaf area index (LAI, Figure 87) is also similar. Those two varieties were investigated to show the added value of the fluorescence signal to separate leaf and canopy effects and provide input data to propose a simple forward model, how leaf chlorophyll content,

canopy architecture and photosynthetic efficiency affect sun-induced fluorescence and reflectance based vegetation measurements. The acquired dataset on leaf and canopy level were used as input for the SCOPE modelling.

The difference in leaf and TOC fluorescence between the two varieties is due to (1) higher absorption of PAR and (2) higher reabsorption of fluorescence in the wild type, and these differences can be explained with radiative transfer modelling (i.e. SCOPE). Using SCOPE together with the ground top of canopy reflectance data we were able to prove that 1) the fluorescence emitted at leaf level is re-absorbed by the leaf and by the different canopy layers before reaching the sensor (Figure 113 and Figure 114) which explains the difference in the spectral shape of fluorescence between the two varieties and 2) when cancelling the leaf and canopy re-absorption and normalizing by aPAR (i.e. estimating the fluorescence emission at chloroplast level), both Eiko and MinnGold present equal total fluorescence spectrum (Figure 114). These results prove that sun-induced fluorescence can be used as a good indicator of plant photochemistry, once the effects due to reabsorption at leaf and canopy level are taken into account. However, further studies needs to be done to (i) correct to overestimation of the fluorescence modelled at F760 nm (Figure 113) and (ii) to correct for the underestimation in photosynthesis estimation (Table 30).

7 Recommendations for future campaigns

Leaf spectra of reflectance and transmittance provide an excellent means to constrain the retrieval of canopy level parameters. These leaf spectra limit the problem of ill-posed retrievals of leaf parameters such as leaf thickness. They preferably include the SWIR and the NIR spectral region, and both the reflectance and transmittance of the leaf. For future activities these leaf level properties shall be considered as prior information to constrain the top-of-canopy retrievals, rather than as exact pixel representative measurements.

The fluorescence yield, which is the fluorescence normalized for reabsorption and by APAR, is a useful measure for estimating the efficiency of NPQ and photochemical electron transport rate. It can be calculated by making use of the full reflectance spectrum as measured with *HyPlant*. However, the differences in fluorescence yield between the two varieties were almost zero, and certainly substantially smaller than differences in fluorescence caused by leaf chlorophyll content and canopy structure. This may be expected because of the similarity in photochemical properties between the two varieties. In future activities is may be useful to include contrasting species or varieties, which have great differences in photosynthetic functioning and different photochemical capacity. Such plant varieties may help to better scale canopy measurements to the photosynthetic function of leaf photosynthesis.

The correct quantification of the degree of non-photochemical energy dissipation (NPQ) remains a challenge and also after this campaign no effective way could be established to determine NPQ by remote sensing approaches. Nevertheless, this SoyFlex study suggests that there is some potential for including the 500-600 nm spectral range of canopy reflectance for quantifying NPQ. The data suggest that NPQ was higher in the Eiko than in the MinnGold, which is consistent with the higher light absorption by Eiko, however we could not establish a robust quantitative transfer function.

For future activities we recommend to independently measure NPQ on the leaf level to have a solid basis for validating NPQ estimates that are derived from the from the 500-600 nm spectral range. Such data can be obtained with active fluorescence measurements at selected leaves. Additionally, we recommend to explore alternative paths to estimate NPQ in case the quantification from the spectral range remains unclear. Such alternative ways may use machine learning or neural networks, which take the complete spectral information into account that is available from the FLEX and Sentinel-3 tandem mission.

In this study we used direct numerical inversion for the retrievals. This leads to a single best performing parameter set, and a local model sensitivity analysis can reveal how sensitive model outputs (such as GPP) are to model inputs (reflectance spectra, fluorescence). A more computationally expensive but statistically solid approach is the use of Monte-Carlo Markov Chains to quantify posterior parameter distributions from *HyPlant* measurements and prior information (field or literature values). It is recommended that a future study considers the use of Markov Chain computations.

References

Alonso L, Gomez-Chova L, Vila-Frances J, Amoros-Lopez J, Guanter L, Calpe J, Moreno J. (2008). Improved Fraunhofer Line Discrimination Method for Vegetation Fluorescence Quantification. *IEEE Geoscience and Remote Sensing Letters,* 5, 620–624.

Asrar G., Fuchs M., Kanemasu E.T. & Hatfield J.L. (1984) Estimating absorbed photosynthetic radiation and leaf-area index from spectral reflectance in wheat. *Agronomy Journal*, 76, 300–306.

Benedict CR, McCree KJ, Kohel RJ (1972). High Photosynthetic Rate of a Chlorophyll Mutant of Cotton. *Plant physiology*, 49, 968–971.

Berk, A.; Anderson, G. P.; Acharya, P. K.; Bernstein, L. S.; Muratov, L.; Lee, J.; Fox, M. J.; Adler-Golden, S. M.; Chetwynd, J. H.; Hoke, M. L.; Lockwood, R. B.; Cooley, T. W.; Gardner, J. A. (2005). MODTRAN5: A reformulated atmospheric band model with auxiliary species and practical multiple scattering options. *Proceedings of the Society of Photo-Optical Instrumentation Engineer*, 5655, 662–667.

Bright RM, Bogren W, Bernier P, Astrup R (2016). Carbon-equivalent metrics for albedo changes in land management contexts: relevance of the time dimension. *Ecological Applications*, 26, 1868–1880.

Campbell BW, Mani D, Curtin SJ, Slattery RA, Michno J-M, Ort DR, Schaus PJ, Palmer RG, Orf JH, Stupar RM. (2015). Identical Substitutions in Magnesium Chelatase Paralogs Result in Chlorophyll-Deficient Soybean Mutants. *G3-Genes Genomes Genetics*, 5, 123–131.

Chojnicki BH, Michalak M, Acosta M, Juszczak R, Augustin J, Droesler M, Olejnik J (2010). Measurements of carbon dioxide fluxes by chamber method at Rzecin wetland ecosystem in Poland. *Polish Journal of Environmental Studies*, 19(2), 283–291.

Cogliati, S., Verhoef, W., Kraft, S., Sabater, N., Alonso, L., Vicent, J., Moreno, J., Drusch, M. and Colombo, R. (2015). Retrieval of sun-induced fluorescence using advanced spectral fitting methods. *Remote Sensing of Environment*, 169, 344–357.

Daloso D de M, Antunes WC, Santana TA, Pinheiro DP, Ribas RF, Sachetto-Martins G, Loureiro ME (2014) Arabidopsis gun4 mutant have greater light energy transfer efficiency in photosystem II despite low chlorophyll content. Theoretical and Experimental Plant Physiology, 26, 177–187.

Damm A, Guanter L, Laurent VCE, Schaepman ME, Schickling A, Rascher U. (2014). FLD-based retrieval of sun-induced chlorophyll fluorescence from medium spectral resolution airborne spectroscopy data. *Remote Sensing of Environment*, 147, 256–266.

Damm, A., A. Erler, M. Meroni, W. Verhoef, M. Schaepman, W. Hillen, and U. Rascher (2011). Modeling the impact of spectral sensor configurations on the FLD retrieval accuracy of sun-induced chlorophyll fluorescence. *Remote Sensing of Environment*, 115(8), 1882–1892.

Damm, A., L. Guanter, V. C. E. Laurent, M. E. Schaepman, A. Schickling, and U. Rascher (2014). FLD-based retrieval of sun-induced chlorophyll fluorescence from medium spectral resolution airborne spectroscopy data. *Remote Sensing of Environment*, 147, 256–266.

Dash J. & Curran P.J. (2007). Evaluation of the MERIS terrestrial chlorophyll index (MTCI). *Advances in Space Research*, 39, 100–104.

Davidson EA, Savage K, Verchot LV, Navarro R (2002). Minimizing artefacts and biases in chamber-based measurements of soil respiration. *Agriculture and Forest Meteorology*, 113, 21–37.

Dawson T.P. & Curran P.J. (1998). A new technique for interpolating the reflectance red edge position, *International Journal of Remote Sensing*, 19, 2133–2139.

Drewry DT, Kumar P, Long SP (2014). Simultaneous improvement in productivity, water use, and albedo through crop structural modification. *Global Change Biology*, 20, 1955–67.

Drusch, M.; Moreno, J.; Bello, U. D.; Franco, R.; Goulas, Y.; Huth, A.; Kraft, S.; Middleton, E. M.; Miglietta, F.; Mohammed, G.; Nedbal, L.; Rascher, U.; Schüttemeyer, D.; Verhoef, W. (2017). The FLuorescence EXplorer Mission Concept – ESA´s Earth Explorer 8. *IEEE Transactions on Geoscience and Remote Sensing*, 55, 1273–1284.

Gamon J., Penuelas J. & Field C. (1992). A narrow-waveband spectral index that tracks diurnal changes in photosynthetic efficiency. *Remote Sensing of Environment*, 41, 35–44.

Gengenbach BG, Gorz HJ, Haskins F (1970) Genetic Studies of Induced Mutants in Melilotus alba. II. Inheritance and Complementation of Chlorophyll-deficient Mutants. *Crop Science*, 10, 154–156.

Gitelson AA, Buschmann C, Lichtenthaler HK. (1998). Leaf chlorophyll fluorescence corrected for re-absorption by means of absorption and reflectance measurements. *Journal of Plant Physiology*, 152, 283-296.

Gitelson, A., and M. Merzlyak. (1994). Spectral Reflectance Changes Associated with Autumn Senescence of Aesculus Hippocastanum L. and Acer Platanoides L. Leaves. *Journal of Plant Physiology*, 143, 286–292.

Guanter L, Frankenberg C, Dudhia A, Lewis PE, Gomez-Dans J, Kuze A, Suto H, Grainger RG. (2012). Retrieval and global assessment of terrestrial chlorophyll fluorescence from GOSAT space measurements. *Remote Sensing of Environment,* 121, 236–251.

Guanter, L., C. Frankenberg, A. Dudhia, P. E. Lewis, J. Gomez-Dans, A. Kuze, H. Suto, and R. G. Grainger (2012). Retrieval and global assessment of terrestrial chlorophyll fluorescence from GOSAT space measurements. *Remote Sensing of Environment*, 121, 236–251.

Guanter, L.; Rossini, M.; Colombo, R.; Meroni, M.; Frankenberg, C.; Lee, J. E.; Joiner, J. (2013). Using field spectroscopy to assess the potential of statistical approaches for the retrieval of sun-induced chlorophyll fluorescence from ground and space. *Remote Sensing of Environment*, 133, 52–61.

Haboudane D., Miller J.R., Tremblay N., Zarco-Tejada P.J. & Dextraze L. (2002). Integrated narrow-band vegetation indices for prediction of crop chlorophyll content for application to precision agriculture. *Remote Sensing of Environment*, 81, 416–426.

Hoffman M., Jurisch N., Albiac Borazz E., Hagemann U., Droesler M., Sommer M., Augustin J. (2015). Automated modeling of CO_2 fluxes based on periodic closed chamber measurements: A standardized conceptual and practical approach. *Agriculture and Forest Meteorology*, 200, 30–45.

Huete A.R., Didan K., Miura T., Rodriguez E.P., Gao X. & Ferreira L.G. (2002). Overview of the radiometric and biophysical performance of the MODIS vegetation indices. Remote Sensing of Environment, 83, 195–213.

Juszczak R, Humphreys E, Acosta M, Michalak-Galczewska M, Kayzer D, Olejnik J (2013). Ecosystem respiration in a heterogeneous temperate peatland and its sensitivity to peat temperature and water table depth. Plant and Soil, 366(1-2), 505–520.

Juszczak R., Acosta M., Olejnik J. (2012). Comparison of daytime and nighttime Ecosystem Respiration measured by the closed chamber technique on a temperate mire in Poland. *Polish Journal of Environmental Studies*, Vol. 21, 643–658.

Li Y, Ren B, Gao L et al. (2013). Less Chlorophyll Does not Necessarily Restrain Light Capture Ability and Photosynthesis in a Chlorophyll-Deficient Rice Mutant. *Journal of Agronomy and Crop Science*, 199, 49–56.

LI-COR Application Note 129. The importance of water vapor measurements and corrections. LI-COR inc. 4421 Superior Street, Lincoln, Nebrasca, USA.

Long SP, Zhu X-G, Naidu SL, Ort DR (2006). Can improvement in photosynthesis increase crop yields? Plant, *Cell and Environment*, 29, 315–330.

Meroni M, Rossini M, Guanter L, Alonso L, Rascher U, Colombo R, Moreno J. (2009). Remote sensing of solar-induced chlorophyll fluorescence: Review of methods and applications. *Remote Sensing of Environment*, 113, 2037–2051.

Ort DR, Melis A (2011). Optimizing antenna size to maximize photosynthetic efficiency. *Plant physiology*, 155, 79–85.

Peñuelas J., Filella I., Biel C., Serrano L. & Savé R. (1993). The reflectance at the 950-970 nm region as an indicator of plant water status. *International Journal of Remote Sensing,* 14, 1887–1905

Pérez-Priego O., López-Ballesteros A., Sánchez-Cañete E.P., Serrano-Ortiz P., Kutzbach L., Domingo F., Eugster W., Kowalski A. (2015). Analysing uncertainties in the calculation of fluxes using whole-plant chambers: random and systematic errors. *Plant and Soil*, 393(1), 229–244.

Porcar-Castell A, Tyystjarvi E, Atherton J, van der Tol C, Flexas J, Pfundel EE, Moreno J, Frankenberg C, Berry JA. (2014). Linking chlorophyll a fluorescence to photosynthesis for remote sensing applications: mechanisms and challenges. *Journal of Experimental Botany,* 65, 4065–4095.

Rossini M, Meroni M, Celesti M, Cogliati S, Julitta T, Panigada C, Rascher U, van der Tol C, Colombo R. (2016). Analysis of Red and Far-Red Sun-Induced Chlorophyll Fluorescence and Their Ratio in Different Canopies Based on Observed and Modeled Data. *Remote Sensing*, 8, 412ff.

Rossini M, Nedbal, L., Guanter, L., Ac, A., Alonso, L., Burkart, A., Cogliati, S., Colombo, R., Damm, A., Drusch, M., Hanus, J., Janoutova, R., Julitta, T., Kokkalis, P., Moreno, J., Novotny, J., Panigada, C., Pinto, F., Schickling, A., Schuttemeyer, D., Zemek, F., Rascher, U. (2015). Red and far red Sun-induced chlorophyll fluorescence as a measure of plant photosynthesis. *Geophysical Research Letters*, 42, 1632–1639.

Rouse J.W.J., Haas R.H., Schell J.A. & Deering D.W. (1973). Monitoring vegetation systems in the Great Plains with ERTS. *Third ERTS Symposium*, NASA SP-351, 309–317

Sakowska et al. (2017). Leaf and canopy photosynthesis of a chlorophyll deficient soybean mutant. *Plant Celle & Environment* (submitted),

Sakuratani T (1981). A Heat Balance Method for Measuring Water Flux in the Stem of Intact Plants. *Journal of Agricultural Meteorology*, 37, 9–17.

Sims, D., and J. Gamon. (2002). Relationships Between Leaf Pigment Content and Spectral Reflectance Across a Wide Range of Species, Leaf Structures and Developmental Stages. *Remote Sensing of Environment*, 81, 337–354.

Slattery RA, VanLoocke A, Bernacchi CJ, Zhu X-G, Ort DR (2017). Photosynthesis, Light Use Efficiency, and Yield of Reduced-Chlorophyll Soybean Mutants in Field Conditions. *Frontiers in Plant Science*, 8, 549.

Specht J, Haskins F, Gorz H (1975). Contents of chlorophylls a and b in chlorophyll-deficient mutants of sweetclover. *Crop Science*, 15, 851–853.

Thayer, S.S. and Bjorkman, O. (1990). Leaf xanthophyll content and composition in sun and shade determined by HPLC. *Photosynthesis Research*, 23, 331–343.

Tucker C.J. (1979). Red and Photographic Infrared Linear Combinations for Monitoring Vegetation. *Remote Sensing of Environment*, 8, 127–150.

van der Tol, C.; Verhoef, W.; Timmermans, J.; Verhoef, A.; Su, Z. (2009). An integrated model of soil–canopy spectral radiances, photosynthesis, fluorescence, temperature and energy balance. *Biogeosciences*, 6, 3109–3129.

Van Wittenberghe S, Alonso L, Verrelst J, Hermans I, Delegido J, Veroustraete F, Valcke R, Moreno J, Samson R. (2013). Upward and downward solar-induced chlorophyll fluorescence yield indices of four tree species as indicators of traffic pollution in Valencia. *Environmental Pollution*, 173, 29–37.

Vilfan, N., van der Tol, C., Muller, O., Rascher, U. and Verhoef, W. (2016). Fluspect-B: A model for leaf fluorescence, reflectance and transmittance spectra. *Remote sensing of environment*, 186, 596–615.

Vogelmann TC, Bornman JF, Yates DJ (1996). Focusing of light by leaf epidermal cells. *Physiologia Plantarum*, 98, 43–56.

Vogelmann TC, Evans JR (2002) Profiles of light absorption and chlorophyll within spinach leaves from chlorophyll fluorescence. Plant, *Cell and Environment*, 25, 1313–1323.

Wu, C., Huang, W., Yang, Q., & Xie, Q. (2015). Improved estimation of light use efficiency by removal of canopy structural effect from the photochemical reflectance index (PRI). *Agriculture Ecosystems and Environment*, 199, 333-338.

Zamft BM, Conrado RJ (2015). Engineering plants to reflect light: strategies for engineering water-efficient plants to adapt to a changing climate. *Plant Biotechnology Journal*, 13, 867–74.